Polymers Based on Cyclopropenium Cations, Squaric Acid Amides and Squaric Acid Quinoxalines as New Electrode Materials for Energy Storage: Synthesis and Characterization

Zur Erlangung des akademischen Grades einer

DOKTORIN DER NATURWISSENSCHAFTEN

(Dr. rer. nat.)

von der KIT-Fakultät für Chemie und Biowissenschaften

des Karlsruher Instituts für Technologie (KIT)

genehmigte

DISSERTATION

von

M.Sc. Victoria Le

1. Referent:	Prof. Dr. Patrick Théato
2. Referent:	Prof. Dr. Helmut Ehrenberg
Tag der mündlichen Prüfung:	17.07.2023

Kurzfassung

Um den weltweit wachsenden Energiebedarf zu decken, müssen die Anstrengungen zur Entwicklung hocheffizienter Batteriesysteme verstärkt werden. Die modernste Technologie, die Lithium-Ionen-Batterie (LIB), gilt als unumstritten und ist daher in fast allen mobilen Geräten zu finden. Trotz ihres unbestreitbaren Wertes für die Menschheit sind die Ressourcen an Lithium, Nickel, Kobalt und anderen wesentlichen Elementen begrenzt. Aus diesem Grund stellen metallfreie, organische Batterien eine wünschenswerte Alternative dar. Metallorganische Radikalbatterien, die auf nitroxylhaltigen Polymeren wie Poly(2,2,6,6-tetramethylpiperidinyloxymethacrylat) (PTMA) basieren, wurden erstmals 2002 veröffentlicht, und kurz darauf wurde die erste rein organische Radikalbatterie (ORB) vorgestellt. Ein großer Nachteil der organischen Materialien ist allerdings ihre vergleichsweise geringe spezifische Kapazität, da ein großer Anteil ihrer Masse nicht an den elektrochemischen Prozessen beteiligt ist, sondern z.B. der strukturellen Stabilität von Nitroxid-Radikalen dient. Um dieses Problem zu überwinden, wurden neue Klassen von nicht-radikalischen redoxaktiven Polymeren auf der Basis von Cyclopropeniumkationen und Quadratsäureamiden untersucht. Die funktionellen Gruppen bestanden aus den kleinsten molekularen Zyklen (d.h. drei- und viergliedrigen Zyklen), welche aufgrund ihrer aromatischen Natur hohe Redoxpotentiale und Zyklenstabilität aufwiesen. Obwohl beide funktionellen Gruppen seit Jahrzehnten bekannt sind, wurde erst in den letzten Jahren die Anwendung von Cyclopropenium-Kationen als hochpotente Katholyten in Redox-Flow-Batterien (RFBs) untersucht. Soweit wir wissen, sind Quadratsäureamide seit Hünigs grundlegenden elektrochemischen Studien im Jahr 1977 nicht mehr mit dem Fokus auf Batterieanwendungen untersucht worden. Aus diesem Grund wurden neue Polymere synthetisiert, die mit Aminocyclopropeniumkationen (ACPs) und Quadratsäureamidderivaten (SAA), insbesondere Quadratsäurechinoxalinen (SQXs), dekoriert waren. Ihre physikalischen und elektrochemischen Eigenschaften wurden im Hinblick auf ihre Verwendung als organisches Kathodenmaterial für Batterien untersucht. Während die

synthetisierten ACP-Polymerverbindungen sehr hygroskopisch waren und irreversible Oxidationen in Lösung unterlaufen sind, stellten sich die SAA-Polymere als vielversprechender heraus. Es konnte demonstriert werden, dass vor allem die SQX-Polymere vorteilhafte Charakteristiken wie eine hohe thermische Stabilität und reversible Redoxeigenschaften in Lösung aufweisen. In nachfolgenden galvanostatischen Zyklisierungen wurde die Leistung von ausgewählten Polymeren in Lithium Halbzellen untersucht. Ein SQX Polymer ist dabei besonders herausgestochen durch seine sehr hohe Zyklisierbarkeit über einhundert Zyklen. Obwohl die erste Entladekapazität (43.7 $\mathrm{mA\,h\,g^{-1}}$) deutlich niedriger als die theoretische Kapazität war (66.8 $\mathrm{mA\,h\,g^{-1}}$), blieben nach 100 Zyklen 91 % der ersten Entladekapazität (39.8 $\mathrm{mA\,h\,g^{-1}}$) erhalten.
Es wird erwartet, dass durch weitere Untersuchungen an kritischen Faktoren für die elektrochemischen Eigenschaften diese neuen redoxaktiven SQX Polymere einen signifikanten Beitrag zu der Entwicklung von organischen Batterien leisten werden.

Abstract

Addressing the globally increasing demand for energy and energy storage devices requires a constant effort in order to develop highly efficient battery systems. The state-of-the-art energy storage technology, the lithium ion-battery (LIB), is mostly considered uncontested for a variety of applications and is therefore employed in nearly all mobile powered devices. Despite their indisputable value for humankind, the global supply of lithium, nickel, cobalt and other substantial elements is limited. On this account, metal-free organic batteriesrepresent a desirable alternative. Metal-organic radical batteries based on nitroxyl-containing polymers, such as poly(2,2,6,6-tetramethylpiperidinyloxy methacrylate) (PTMA), were first reported in 2002 by Nakahara and al. and shortly after the first all-organic radical battery (ORB) was introduced. Nevertheless, a major downside of organic energy storage materials is their comparatively low specific capacity. This is mostly attributed to the high amount of their relative mass not contributing to the electrochemical processes but e.g., to the radical stability of nitroxide radicals. To overcome this issue, new classes of non-radical redox-active polymers based on cyclopropenium cations and squaric acid amides were investigated. The functional groups consisted of the smallest molecular cycles (i.e., three- and four-membered cycles) and showed high redox potentials along with cycling stability by virtue of their aromatic nature. Although both functional groups were known for decades, only in recent years the application of cyclopropenium cations as high-potential catholytes in redox-flow batteries (RFBs) has been further investigated. In comparison and to the best of our knowledge, squaric acid amides have not been explored for battery applications since Hünigs basic electrochemical studies in 1977. Consequently, we synthesized new polymers decorated with amino cyclopropenium (ACP) cations and squaric acid amide (SAA) derivatives, in particular squaric acid quinoxalines (SQXs). Their physical and electrochemical properties were studied in regard to their application as organic cathode materials for batteries. While the synthesized ACP polymer networks were very hygroskopic and

exhibited irreversible oxidation in solution, the SAA polymers turned out to be more promising. It could be demonstrated that especially the new SQX polymers exhibited desirable traits like high thermal stability and reversible redox properties in solution. In subsequent galvanostatic cycling tests, the performance of selected polymers in Li half-cells was examined and one SQX polymer particulary stood out by showing very high cyclability over 100 cycles. Even though the initial capacity (43.7 $\mathrm{mA\,h\,g^{-1}}$) was much lower than the theoretical capacity (66.8 $\mathrm{mA\,h\,g^{-1}}$), after 100 cycles 91 % (39.8 $\mathrm{mA\,h\,g^{-1}}$) of the initial capacity was retained.
It is expected that with further examination of critical factors affecting the electrochemical properties, these new redox-active SQX polymers will significantly contribute to the advancement of organic batteries as new polymeric electrode materials.

Contents

List of Abbreviations

ACP	amino cyclopropenium cation
AIBN	2,2-azobis(2-methylpropionitril)
APCI	atmospheric pressure chemical ionization
ATR	attenuated total reflection
Boc	*tert*-butyloxycarbonyl
CE	coulombic efficiency
CP	cyclopropenium
CTA	chain transfer agent
CV	cyclic voltammetry
DBTTC	S,S-dibenzyl trithiocarbonate
DDD	2,5-diphenyl-2,5-diazabicyclo[4.2.0]oct-1(6)-ene-7,8-dione
DHb	deoxyhemoglobin
DIPEA	*N,N*-diisopropylethylamine
DMC	dimethyl carbonate
DSC	differential scanning calorimetry
EA	electron affinity
EC	ethylene carbonate
EPR	electron paramagnetic resonance
FTIR	Fourier transform infrared
IR	infrared
IUPAC	International Union of Pure and Applied Chemistry
KIT	Karlsruhe Institute of Technology
LCAO	linear combination of atomic orbitals
LIB	lithium-ion battery
LMO	lithium manganese oxide

MHb	methemoglobin
MS	mass spectrometry
NAD	nicotinamide adenine dinucleotide
NADP	nicotinamide adenine dinucleotide phosphate
NASA	National Aeronautics and Space Administration
NMC	Ni-Mn-Co oxide
NMR	nuclear magnetic resonance
OEM	organic electrode material
ORB	organic radical battery
Ox	oxidant
PC	propylene carbonate
PCCP	pentachlorocyclopropane
PPM	post-polymerization modification
PQ	plastoquinone
PTMA	poly(2,2,6,6-tetramethylpiperidinyloxy methacrylate)
RAFT	reversible addition-fragmentation chain-transfer
RE	reference electrode
Red	reductant
RFB	redox-flow battery
ROM	redox-active organic material
SA	squaric acid
SAA	squaric acid amide
SAE	squaric acid ethyl ester
SEC	size-exclusion chromatography
SQX	squaric acid quinoxaline
TBAP	tetrabutylammonium perchlorate
TEA	triethylamine
TEMPO	2,2,6,6-tetramethylpiperidinyloxy
TFA	trifluoroacetic acid
TGA	thermogravimetric analysis
V-70	2,2'-azobis(4-methoxy-2,4-dimethylvaleronitrile)
WE	working electrode
XRD	X-ray diffraction

1 Introduction and Motivation

The rapid growing demand for sustainable energy storage solutions in recent years is a global economic and scientific challenge. With e.g., the European union banning new petrol and diesel cars as of 2035, the manufacturing of electric vehicles with high power batteries is becoming a crucial aspect to achieve that goal. The currently leading battery technologies like lithium-ion battery (LIB) or nickel/metal hydride (Ni/MH), are based on metal containing electrodes which are usually difficult to recycle, expensive and unsafe.[1,2] One main concern, especially for LIBs, is the unstable supply of their key resources, namely cobalt and lithium, due to their natural geographical concentration.[3] As a result, a solution for low-cost, sustainable and high-performance batteries can be metal-free batteries based on redox-active organic materials (ROMs).[4–6] Since ROMs consist of inexpensive, light and abundant elements, like carbon, nitrogen, hydrogen, oxygen and sulfur, ROM-based batteries are more lightweight and cost-effective in contrast to LIBs.[7–9] To develop batteries with high specific capacity and energy density, known ROMs are being thoroughly investigated for their application in energy storage technologies. After the introduction of the first full-organic battery in 2009, a lot of effort was put into research on ROMs that could be used as anode and cathode materials and they were thoroughly investigated.[10] Due to these efforts, a range of organic materials was established for organic batteries and recent research was focused on optimizing their properties and composition, combining them or optimizing the cell setups and electrolytes.[4,11–17] Since the current pool of ROMs is limited to these established compounds, the possibilities to manufacture a viable and promising full-organic battery is also limited, respectively.[8,9,18–20] Therefore, an introduction of new materials to expand the pool of the currently accessible ROMs, is a crucial part to make organic batteries possible. Some important points are required for the materials to make reasonable contributions:

- ability to undergo stable and reversible redox reaction(s)
- reasonable and cost-efficient synthetic effort to achieve the molecular structure
- electrochemical stability and relative inertness towards other compounds inside the battery
- modifiable structure for possible fine-tuning of the chemical stability or redox potential.

In this work, new ROMs for the application in organic batteries are introduced with structures based on the smallest known aromatic cyclic molecules, namely cyclopropenium cations and cyclobutene-diones. These compounds exhibit remarkably stable redox reactions due to their aromatic nature. After the first oxidation, they form radical (di-)cations that can be stabilized by introduction of heteroatoms like nitrogen. Since unpaired electrons can be stabilized by localisation on N, the compounds investigated in the work at hand are amino cyclopropenium cations (ACPs) (Scheme 1.1) and squaric acid (SA) (Scheme 1.2) based amides.[21]

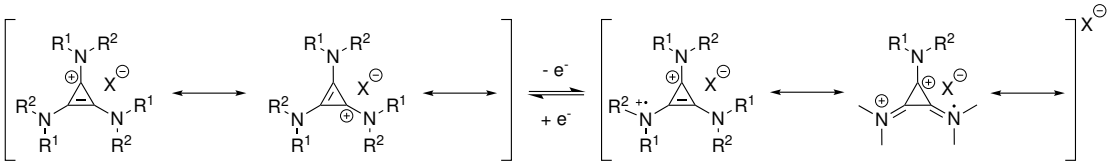

Scheme 1.1 Resonance-stabilized structures of an ACP and its radical dication during an one-electron redox reaction.

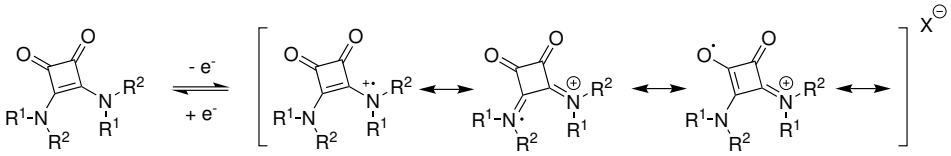

Scheme 1.2 Resonance-stabilized radical cation of a SA amide after an one-electron oxidation.

Even though these compounds were known for decades, their application for energy storage purposes have been widely overlooked.[22–24] While ACPs have recently been investigated as catholytes in non-aqueous redox-flow batteries (RFBs), an expanded use as ROM in non-stationary batteries has not been discussed yet.[25–27] The situation for

SA based amides is more tenuous, since there was no significant study on their electrochemical properties since Hünigs ground work in 1977.[28] On the other hand, the structurally related squaraines dyes have found widespread application in biomedical and optoelectronical applications due to their wide absorption range, very low band gaps and high intrinsic conductivity without doping.[29–32] Two cristalline squaraines were employed as cathodes in LIBs and showed exceptional longterm cycling stability due to their strong dipole effects.[33] Since the underlying SA structure is contributing to the exceptional properties of these dyes, it is safe to assume that this structural motif will also benefit the redox activity of the SA based amides.

A completely overlooked class of redox-active amides is the class of cyclobuta[b]quinoxaline-1,2-diones or squaric acid quinoxalines (SQXs). They had first been synthesized in 1968 through condensation of squaric acid and *o*-phenylenediamines and the electrochemical behavior of some SQX molecules were examined by Hünig and coworkers in 1977.[28,34] In that studies, the distinctly high thermal stability of the SQX moieties were already acknowledged but not further investigated. The motivation for reinventing the SQX functional groups arise from multiple aspects. Firstly, the reversible redox reactions could be interesting for new organic molecules since most organic redox systems were derived from biological systems and already well-studied. Chemical modifications on the redox center are usually limited, therefore the redox potentials of these systems can not be much enhanced while at the same time making sure that the reversibility is retained (e. g., quinones or pyrazines).[35,36] For this reason, a completely new redox-active moiety like the SQX unit could enable the investigation of novel functional structures with tunable redox properties.

2 Fundamental Concepts of Redox Polymers

2.1 Electrochemistry Basics

If a chemical reaction is simultaneously linked with a change in electrical charge (e.g., due to electron transfer), it is called an electrochemical reaction. Electrochemical oxidation/reduction- or redox reactions are associated with a change in the oxidation states of the participating atoms.[37] A general redox reaction can be depicted as follows:

$$\text{Red} \rightleftharpoons \text{Ox}^{n+} + n\,\text{e}^- \qquad \{1\}$$

Simplified equation for a redox reaction, where Red is the reductant, Ox the oxidant and *n* is the number of electrons (e^-).

Each redox reaction consists of a so called redox couple, a reductant (Red) and an oxidant (Ox). During the redox half-reaction, Red is acting as the reducing agent and is capable of transfering an electron (e^-) to Ox. The redox potential of the Red or Ox is linearly related to their electron affinity (EA), a measure to quantify a molecules capability to bind an electron in gas phase. In solution, this ability is strongly affected by the interaction of the formed anion with the solvent and only partly by its EA in gas phase. The variable that is best suited to quantify the in-solution property is the standard electrode potential E^0. A simple equation is given for the relationship between EA and E^0 as

$$E^0 = -\Delta G_a^0(B) - (\Delta G_{sol}^0(B^-) - \Delta G_{sol}^0(B)) + C, \qquad (2.1)$$

where B referes to the molecule, B^- its anionic counterpart, ΔG_a^0 the electron attachement free energy in gas phase, ΔG_{sol}^0 the free energy of the molecule transfer from gas phase to

solution and C a reference electrode dependent constant, respectively.[38] The difference in the solution free energies between B and B^- can be expressed by $\Delta\Delta G^0_{sol}$ as

$$\Delta\Delta G^0_{sol} = \Delta G^0_{sol}(B^-) - \Delta G^0_{sol}(B). \tag{2.2}$$

It has to be noted that the solvation free energy $\Delta\Delta G^0_{sol}$ is depending on the solvent molecules and strongly correlating with EA. For high EA values, $\Delta\Delta G^0_{sol}$ is decreasing, which can be interpreted as weaker bonding between the molecules of the solvent and B^- due to it being a well stabilized anion with high delocalization of its negative charge. This also results in a linear correlation of EA and E^0 when the values of $\Delta\Delta G^0_{sol}$ and C are assumed to be constant in a defined solvent and with a solvent-independent reference. The equation 2.1 is then simplified to

$$E^0 = -\Delta G^0_a(B) + D, \tag{2.3}$$

where, for a defined solvent and reference, D is a constant summarizing $\Delta\Delta G^0_{sol}$ and C. According to this equation, E^0 and $\Delta G^0_a(B)$ are linearly correlated. Therefore, a low EA is associated with a low E^0 as more energy is needed to transfer an electron to a species that has low affinity to electrons. Due to this correlation it is possible to estimate the redox potential of molecules by their EAs and corresponding dissociation constant K^0_d, respectively, without taking the redox environment into consideration.[39]

2.1.1 Principles of Redox Reactions

Each redox reaction is associated with an electron transfer process between Red and Ox (as discussed in section 2.1). The Nernst equation relates the redox potential E of the reaction with the ratio of the participating species in respect to a reference electrode

$$E = E^0 + \frac{RT}{nF}\ln\frac{a_{Ox}}{a_{Red}}, \tag{2.4}$$

where E^0 is the standard redox potential, a_{Ox} and a_{Red} are the activities of Ox and Red, R is the universal gas constant ($8.314\ \mathrm{J\,mol^{-1}\,K^{-1}}$), T is the temperature in K and F the

faraday constant (F = 96 485.3 $\mathrm{C\,mol^{-1}}$).[40] The redox potential E will be equal to E^0 if $a_{Ox} = a_{Red}$. It is worth noting, that the electrode potential can be altered by changing the ratio of the activities of Ox and Red but is independent of their magnitudes at a constant ratio. The activity a is a measure to express the deviation of a real system from an ideal one and is expressed as a product of the activity coefficient γ_i and molar fraction x_i.

$$a = \gamma_i \, x_i. \tag{2.5}$$

In solution, an ion i will aggregate oppositely charged ions around itself. Therefore, the central ion can only interact after stripping from this ion-cloud. The energy required to do this is then lost for the system and the central ions reactivity. In an ideal solution, there would be no ionic interactions (γ_i = 1) and the activity would only be dependent on the molar fraction x_i. For this case, the chemical potential of the ion i without the surrounding cloud can be expressed as μ_i^{ideal}. To describe the chemical potential μ_i^{real} of the ion in a real solution, it can be written as follows:

$$\mu_i^{\text{real}} = \mu_i^{\text{ideal}} + R\,T \ln \gamma_i, \tag{2.6}$$

or

$$\mu_i^{\text{real}} = \mu_i^{\text{ideal}} + L\,U, \tag{2.7}$$

where U is the mediate potential energy of the ion cloud multiplied with the Avogadro Number L (6,022 $\times$ $10^{23}\mathrm{mol^{-1}}$).[41] For very dilute solutions (approx. $10^{-3}\mathrm{mol\,kg^{-1}}$), following points can be assumed:

- the radius of the ion cloud is much larger than the radius of the central ion
- there are no ion pairs in the solution
- the space around each central ion is spherically symmetric
- all interactions are exclusively electrostatic.

These assumptions lead to the expression for the standard Debye-Hückel limiting law

$$\ln \gamma_{\pm} = -A \mid z^+ \, z^- \mid \sqrt{\mathbf{I}}, \tag{2.8}$$

where $\gamma_{\pm}$ is the mean activity coefficient, A a solution specific constant, z^+ and z^- are the charge numbers of cations and anions in solution and

$$\mathbf{I} = \frac{1}{2} \sum_i \; z_i^2 \; x_i, \tag{2.9}$$

is the ionic strength. This standard form of the Debye-Hückel limiting law predicts the same $\gamma_{\pm}$ values for different electrolytes with the same charge, which is working well for singularly charged electrolytes, but fails for multi-charged ones. Nevertheless, it is important to point out that the activity coefficent is only dependent on the ionic strength, according to equation 2.8. Therefore, in the presence of more than one electrolyte, $\gamma_{\pm}$ will remain constant as long as the concentration of the strongest electrolyte stays constant.

In highly concentrated solutions (> 0.5 M), the equation 2.8 is not suitable anymore. There are different strategies to describe $\gamma_{\pm}$ in contentrated electrolyte solutions by either extending the Debye-Hückel-theory by a linear factor, like in the Davies equation, or by using the Pitzer equations which are suited to describe short-range ion-ion-interactions in solution.[42] For the understanding of the contents described in the following chapters, it is not necessary to discuss these equations in detail. However, it should be kept in mind that the composition of the electrolyte solutions (concentrations, nature of ions, solvent, temperature etc.) has a significant impact on the redox behavior of the molecules and polymers discussed in the thesis at hand.

2.2 Redoxactivity in Molecules

The fundamental importance of redox reactions is obvious by looking into natural processes. One of the most significant ones is photosynthesis which uses light ($h\nu$) to consequently produce energy from carbon dioxide CO_2 in plants.[43] The overall reaction is summarized as follows:

$$H_2O + h\nu \; + CO_2 \longrightarrow CH_2O + O_2, \tag{2}$$

where CH_2O is given as a general formula to describe carbohydrates. During the photosynthesis, a range of redox reactions take place e.g., water is being oxidized to

oxygen and the electrons from this reaction are transferred to the next reaction center *via* plastoquinone (PQ), an electron acceptor molecule. PQ is undergoing two redox reactions in a sequence to PQH_2 to transport the e^- (the redox reactions are depicted in Fig. 2.1, 1). Other redox-active key molecules in biological processes are the nicotinamide adenine dinucleotide (NAD) and nicotinamide adenine dinucleotide phosphate (NADP) (refer to Fig. 2.1, 2). The NAD^+/NADH and $NADP^+$/NADPH redox couples are crucial as they act as natural sources for protons and e^- in metabolic processes like the Krebs cycle and many anabolic pathways.[44] In addition to organic redox molecules, inorganic small molecules

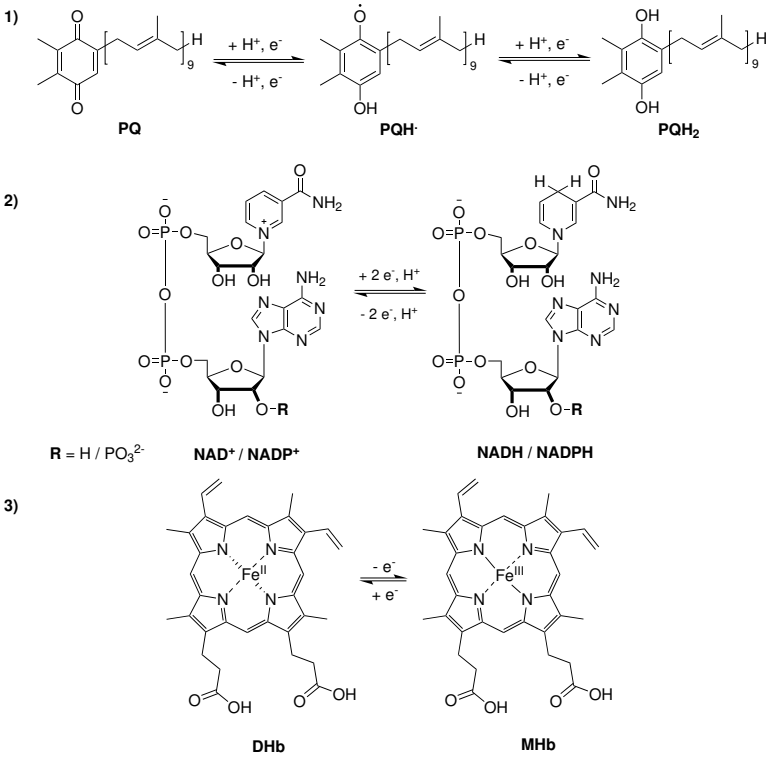

Fig. 2.1 Natural redox reactions in biological processes. 1) Two consecutive one-electron redox reactions from PQ to PQH_2 *via* the semiquinone PQH·. 2) NAD^+/NADH and $NADP^+$/NADPH redox couples. 3) Inorganic redox reaction of hemoglobin from DHb (Fe^{II}) to MHb (Fe^{III}).

and redox centers are also employed for central biological functions. Besides their function as coenzymes for enzymatic reactions, the iron-containing protein hemoglobin is crucial for the transport of oxygen *via* red blood cells in the blood circulatory system.[45] Before the binding of oxygen, the porphyrin structure of deoxyhemoglobin (DHb) is curved / domed and the Fe center is not in plane with the porphyrin Ns (see Fig. 2.1, 3).

After oxygen is bound, the porphyrin flattens and Fe is moving into plane. When the Fe^{II} of DHb is oxidized to Fe^{III}, oxygen is released and methemoglobin (MHb) is formed.

2.2.1 Multistage Organic Redox Systems

In 1978, general structural principles for multistage organic redox systems were described by Deuchert and Hünig.[46] According to their report, compounds undergoing two reversible redox reactions are equipped with two end groups, X and Y (refer to Scheme 2.1). The nature of these end groups dictate the presented redox system: X-groups usually possess free electron pairs, are easily oxidizable and capable of stabilizing a positive charge (e.g., N). Y-groups on the other hand are easily reduced and possess the ability to stabilize a negative charge (e.g., O). If the compound is equipped with two X-groups, the redox system is called *p-type* (see Scheme 2.1, first row), in case two Y-groups are in place, the system is called *n-type* (Scheme 2.1, second row). For a redox compound that is equipped with both groups, respectively, the system is called *bipolar-type* (Scheme 2.1, last row). The basic three structures, that these redox compounds undergo, can be categorized as **RED** (fully reduced state), **SEM** (intermediate radical state) and **OX** (fully oxidized state). While the charges are localized in the **RED** and **OX** stages, in the **SEM** stage the radical is usually strongly delocalized, which makes the radical less reactive and therefore well stabilized. From this structural principle, a range of multistage organic redox systems can be deduced, since the variety of possible end groups X and Y (heteroatoms like N, O, S, P or π-systems) and linking vinylene units is very large. Deuchert and Hünig described two types of redox systems:

1. Open-chain vinylogous redox systems,
2. Redox systems with cyclic π-systems between X and Y.

The systems with cyclic π-systems were further classified into Wurster type (end groups outside of the π-system with aromatic character in the **RED** state), inverse Wurster type (cyclic π-system is aromatic in **OX** state), Weitz type (end groups are part of the cyclic π-system that is aromatic in the **OX** state), inverse Weitz type (end groups are part of the π-system that is aromatic in the **RED** state) and lastly, semi-Weitz type (only one of the end groups is part of the aromatic cyclic π-system in the **OX** state).

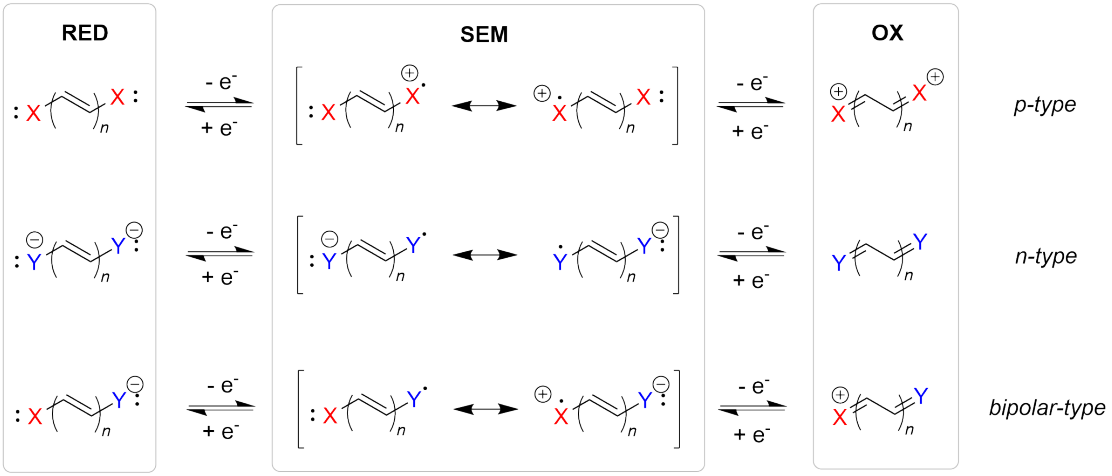

Scheme 2.1 Schematic representation of the general structural principles for organic multistage redox systems[46]. In the case of reversible two-stage redox systems, three structural stages (from left to right: **RED**, **SEM** and **OX**) exist. They are stabilized by the end groups X (red) and Y (blue), who simultaneously dictate the type of redox system at hand (*p-type*, *n-type* and *bipolar-type*).

2.3 Redox-Active Polymers

Shirakawa *et al.* reported in 1977 the first electronically conductive polyacetylenes.[47] The discovery of these polymers laid the foundation for the field of conductive and further, electrochemically active polymers. Since then, great progress was made in this area which significantly impacted the technological advancements in fields like medicine or electronics.[48–51] Generally, electrochemically active polymers can be categorized into two main classes:

i) Electrically conducting polymers

ii) Redox polymers.

Electrically conducting polymers are defined by the International Union of Pure and Applied Chemistry (IUPAC) as polymeric material that exhibits bulk electric conductivity.[52] This definition does not distinguish between ion-conducting and electron conducting polymers and is interchangeably used for both even though the processes behind the two conductivities are very different. For ionic conductivity, the polymer segment mobility is the determining parameter, whereas in case of electron conductivity the mobility of the delocalized electrons moving through conjugated systems is the contributing

factor.[53–56] Nevertheless, the advancement made in both fields of conductive polymers established new applications for polymeric materials including in energy storage systems.

Redox polymers are also a class of electrochemically active polymers. By definition of IUPAC, redox polymers contain groups that can be reversibly reduced or oxidized.[57] These groups, also called redox sites, can have inorganic (e.g., ferrocene) or organic active centers and additionally, can be located either in the polymer backbone or in the side chains.[4,58,59] An overview of selected redox-polymers is depicted in Fig. 2.2. The illustrated redox polymers are divided into n-, p- and bipolar-types. N-type polymers will undergo reversible reduction to form a negatively charged structure that is compensated by a counter cation (depending on the environment, e.g., Li^+ or any other metal cation). In contrast to them, p-type polymers undergo reversible oxidation by losing an e^- and forming a positively charged structure that is combined with available anions to compensate the charge. Lastly, as the name suggests, bipolar redox polymers can undergo both n-type and p-type redox reactions. The best known bipolar redoxpolymer is poly(2,2,6,6-tetramethylpiperidinyloxy methacrylate) (PTMA). PTMA was first introduced in 2002 as a potential environmentally friendly cathode material in rechargeable batteries.[60] Due to its bipolar redox behaviour, PTMA cathodes could on paper deliver their theoretical capacity of 111 mAh g^{-1} twice.[61] A main problem is PTMAs poor conductivity. It has to be mixed with conductive additives to fabricate electrodes, which subsequently lowers the specific capacity of the battery. The redox mechanism of PTMA is depicted in Scheme 2.2.

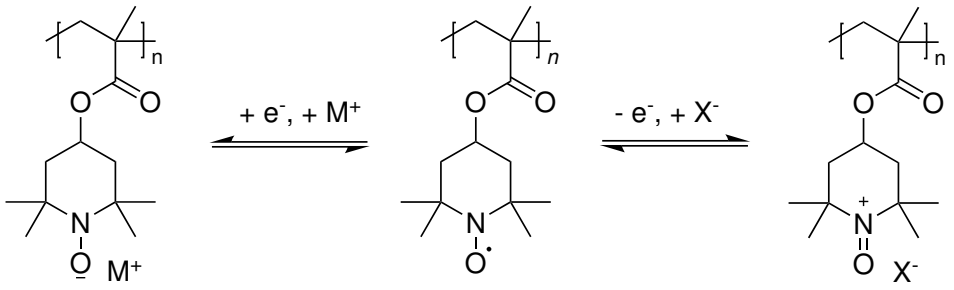

Scheme 2.2 The bipolar redox reactions PTMA can undergo to form aminoxyl anions (left) or oxoammonium cations (right). M^+ and X^- are the charge compensating cation and anion, respectively.

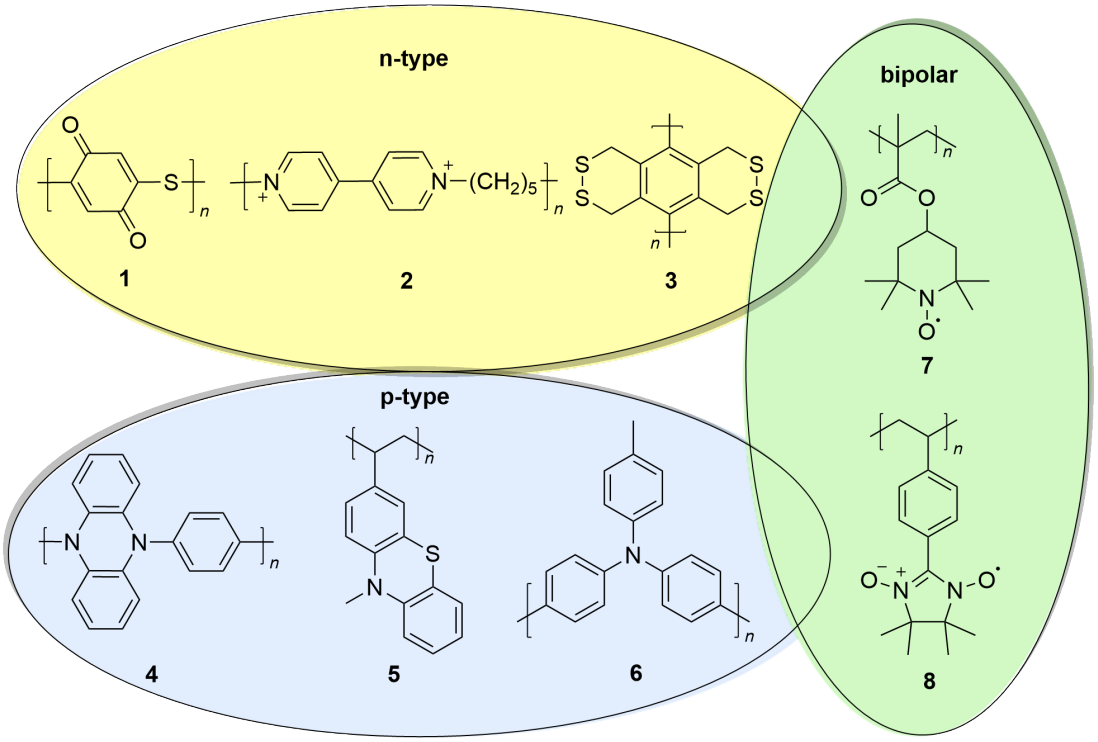

Fig. 2.2 Overview of redox-active polymers. N-type polymers: **1** poly(benzoquinonyl sulfide) (PBQS)[62], **2** poly(1,1'-pentyl-4,4'-bipyridinium dihexafluorophosphate) (PBPy)[63] and **3** poly(5,8-dihydro-1H,4H-2,3,6,7-tetrathiaanthracene) (PDTTA)[64]; p-type polymers: **4** *N,N*'-diphenyl-5,10-dihydrophenazine (DPPZ)[65], **5** poly(3-vinyl-N-methylphenothiazine) (PVMPT)[66] and **6** Polytriphenylamine (PTPAn)[67]; bipolar-type polymers: **7** poly (2,2,6,6-tetramethylpiperidinyloxy methacrylate) (PTMA)[60] and **8**: Poly[4-(nitronylnitroxyl)styrene][68].

2.4 Applications of Redox-Active Materials

As mentioned in the previous chapters, the interesting properties of redox-active materials offer a range of possible application areas. One of the broadest fields of application is energy storage, especially renewable, environmentally friendly and sustainable energy storage technologies like capacitors and batteries.[5,69] Some important parameters to describe the poperties of batteries have to be noted:

i) energy density

ii) power density

iii) cycle life

iv) cost

v) safety.

These parameters are directly influenced by the materials employed in batteries. For instance, a low conducting electrode material has to be supplemented with conductive additives, which lowers the energy density of the resulting battery system. Furthermore, the composition of the deployed electrodes has an effect on the overall cost, safety and cycle life. On the level of the active material, the most important performance defining parameters are the following:

1) Cell voltage V,

2) capacity C,

3) rate capability,

4) C-rate.

It becomes clear, that the multitude of parameters makes it difficult to have every single aspect balanced to create the "perfect" battery. The alteration of one single point can affect the whole battery system and depending on its application, some parameters will be more important than others. In the following sections, some important battery technologies will be introduced.

2.4.1 Redox-Flow-Batteries (RFBs)

In the industrial scale of electricity energy storage systems, redox-flow batteries (RFBs) are a promising technology since they are safe, cost-effective, scalable, independent of fluctuations (in comparison to e.g., wind energy) and allow for high energy in- and output.[12,70] In general, the setup of a RFB consists of two electrolyte tanks that are connected by an electrochemical cell with an ion-selective separator (see Fig. 2.3). The tanks are filled with dissolved redox-active species with different reduction potentials. The species with the lower reduction potential is referred to as the anolyte (in relation to the anode in galvanic cells), while the other electrolyte is called catholyte. The separator inside the electrochemical cell is only permeable for the conductive salt but

not for the redox-active electrolytes, in this way the charge balance is retained and, if needed, the capacity and power of the battery can be scaled separately. The electrolyte solutions are pumped between the cell and the storage tanks. During charging (external supply of electrical energy), the anolyte is reduced and the catholyte is oxidized in their respective half-cells. The electron transfer reactions take place on porous electrodes and the electrical enery is converted into chemical energy. When the battery is discharging (electrical energy is released), chemical energy is converted into electrical energy whilst the anolyte is oxidized and the catholyte is reduced. To store the electrolytes, they are pumped into their respective storage tanks and can be pumped back into the cell for the next charging process.

RFBs can be categorized by their solvent, aqueous or non-aqueous, or their redox

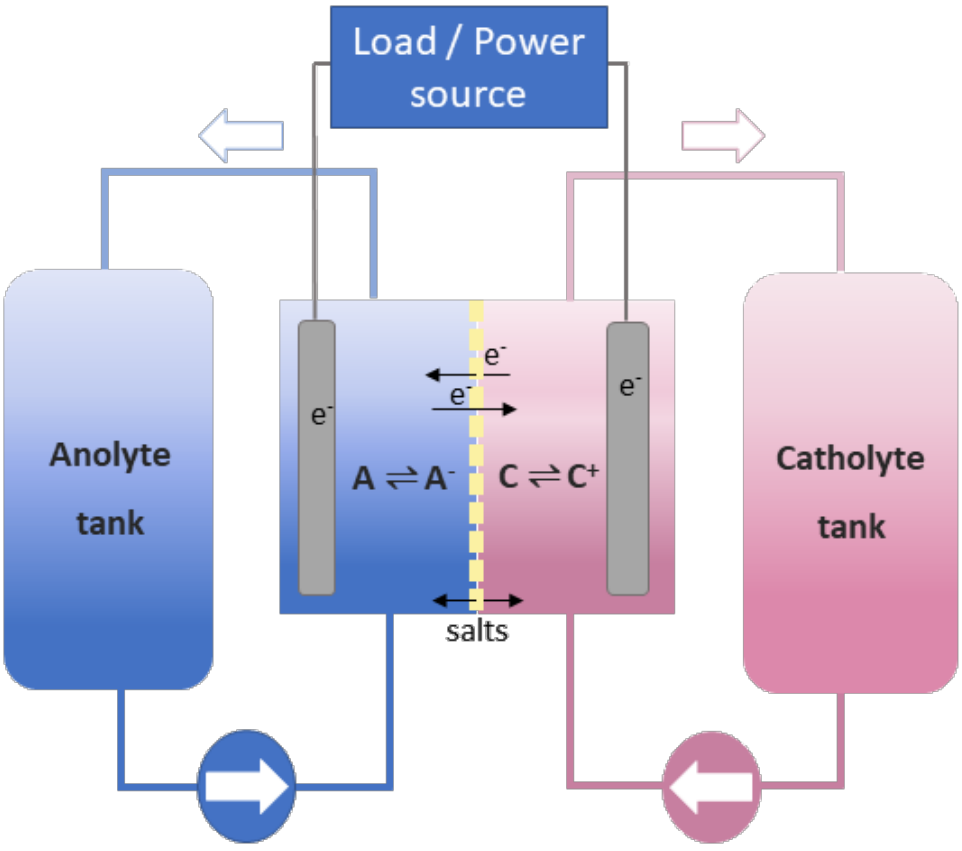

Fig. 2.3 Schematic representation of a redox-flow battery (RFB). The redox reactions of the anolyte (A) and catholyte (C) are depicted in their respective half-cells.

couples, respectively. The most studied and advanced RFB is the aqueous V^{II}/V^{III} (anolyte) and V^{IV}/V^{V} (catholyte) all-vanadium RFB. It was developed in 1986 and presented significant improvements to the unsymmetric Cr/Fe RFB that was deployed by the National Aeronautics and Space Administration (NASA).[71,72] This battery suffered from a relatively low open-circuit potential and crossover of the Fe- and Cr-ions into the opposite half-cells. The all-vanadium RFB solves the cross-contamination issue and shows a stable and higher open-circuit potential then the iron/chromium RFB. Over the years, a lot of improvements were developed for this battery, concentrations up to 3 M were achieved and the cycle stability was improved to as many as 20 000 cycles.[73] Despite these advantages, the all-vanadium RFB are relatively high-cost and therefore not feasible for commercial use.

One strategy to compete these costs is to develop inorganic RFBs from more abundant raw materials or the use of hybrid systems. The costs of all-iron RFB is significantly lower compared to their all-vanadium counterparts, but so is the cell voltage.[74] In hybrid systems, one compound of the redox species is plated onto the electrode. These systems are accompanied by other challenges like dendride formation and careful pH-control.

A different strategy to lower the high-costs of RFBs is utilizing organic redox species. They can be synthesized from low-cost starting material, chemically tailored to match desired electrochemical properties.[75] Additionally, the use of non-aqueous solvents can circumvent the limited electrochemical stability window of water and facilitate the deployment of ROMs as redox species.[76] These developments made the application of carefully tailored catholytes like ACPs possible.[27,77,78] The most important aspects of the redox-activity of ACPs will be shortly discussed in chapter 3.

2.4.2 Li-Ion-Batteries (LIBs)

The commercially most successful and abundant portable battery technology is the lithium-ion battery (LIB). Its undoubtedly importance was honored with the Nobel Prize in Chemistry in 2019.[79] The first use of $LiCoO_2$ as cathode was presented in 1979 and the basis for Li-intercalated graphite anodes was laid shortly after to replace the pure Li-metal anode.[80,81] Since the electrolyte propylene carbonate (PC) was incompatible with graphene (intercalations into the graphite structure and strong decomposition), further improvements on the anode were done by Yoshino, who implemented filamentous carbon

fibers instead of graphene as anode and combined them with the $LiCoO_2$ cathode to patent the first commercialized LIB in 1987.[82–84]. In the decades after, the compounds in LIBs were further improved and especially the field of cathode materials experienced a big growth.[85] The lithium manganese oxides (LMOs) and $LiNiO_2$ cathodes were developed as cheaper options to $LiCoO_2$ but were limited in their practical capacity and especially $LiNiO_2$ suffered from irreversible cation mixing of Ni^{+2} and Li^+. A partial substitution of Ni with other metals was improving the cycling rate and irreversible migration of Ni^{+2} into Li^+ sites. To the current day, Ni-Mn-Co oxides (NMCs) are one of the leading cathode materials in LIBs with a market share of 64.5 % of electric vehicle batteries in 2020 (all NMCs were summarized without distinction of their actual composition).[86] The composition of a LIB consists of three main parts:

1) electrodes (cathode and anode)

2) electrolyte

3) separator.

As the name suggests, the separator is keeping the electrodes physically separated and prevents short-circuits while at the same time enabling ions to flow through. The electrolyte is the medium alowing the ions to move from one electrode to the other, where following reactions take place (on the example of a graphene/$LiCoO_2$ cell):

$$\textbf{Anode}:\ 6\ C + x\,Li^+ + x\,e^- \underset{\text{discharge}}{\overset{\text{charge}}{\rightleftharpoons}} Li_xC_6 \qquad \{3\}$$

$$\textbf{Cathode}:\ LiCoO_2 \underset{\text{discharge}}{\overset{\text{charge}}{\rightleftharpoons}} Li_{1-x}CoO_2 + x\,Li^+ + x\,e^- \qquad \{4\}$$

$$\textbf{Overall}:\ LiCoO_2 + 6\ C \underset{\text{discharge}}{\overset{\text{charge}}{\rightleftharpoons}} Li_{1-x}CoO_2 + Li_xC_6 \qquad \{5\}$$

As described by the redox reactions, during charging Li^+ ions are removed from the $LiCoO_2$ cathode and intercalated into graphene (simplified as C) on the anode, while during discharging the opposite reaction takes place. The shuttling of Li^+ is associated with heat formation that needs to be sufficiently dissipated to prevent an overheating of the cell. Overheating can lead to a series of other unwanted reactions resulting in a thermal runaway.[87] This is a severe safety risk when it comes to LIBs and requires a range of internal and external safety improvements to ensure a secure battery.[1] The safety

concerns are just one of the disadvantages of the LIB, another issues is the dependency on critical resources. While the ultimate aim is to become fossil-fuel independent, the innovations in this regard are introducing new problems by generating an elevated need in critical elements.[86] This demand is accompanied by enhanced mining production, causing other environmental hazards, large quantities of waste and a reliance on insecure supply chains due to geopolitical constraints.[86,88] There are multiple projection studies to estimate the impact of this increased demand and they consistently call for a higher recycling rate of LIBs as a sustainable solution to these issues.[2,3,89,90] The main recycling processes for LIB recycling are pyrometallurgy and hydrometallurgy.[91] For the recovery of metals by pyrometallurgical processes, high temperatures are needed to reduce the LIB metal oxides into an alloy (> 1000 °C). Since the process is done at very high temperatures in a contained environment, it is relatively safe and the LIBs can be used as whole cells. Major drawbacks of this recycling method is the evolution of toxic gaseous products, recovery only of metallic components and very high energy cost. For hydrometallurgical metal reclamation, the electrodes have to be treated with an aqueous solution to extract the desired metals. The most commonly used solution is H_2SO_4/H_2O_2, which is working especially well for Co and Li recovery.[92] Before the extraction can be done, the LIBs have to be opened and physically separated first, which makes the recycling very complex. Additionally, hydrometallurgic metal recovery can cause cross contamination if the extractions and precipitations are not done carefully, and it requires very high solution volumes, which have to be neutralized afterwards.[91] Another long-term solution to the issues discussed above can be the substitution of metal oxides with organic electrode materials (OEMs). Since organics mainly consist of naturally abundant elements like C, H, O, N and S, they could provide access to low cost and sustainable electrodes.[8] The abandonment of Li metal oxides as cathodes for LIBs should already reduce the costs of the battery considerably. Beside the economical benefit, organic materials can be very well chemically altered to design new materials with specific properties. Therefore, a range of redox-active species (molecules and polymers) can be modified to match the required properties the OEM needs. For example, RFBs have very different requirements than LIBs. A well soluble catholyte in a RFB system will be unsuitable for LIBs and show poor capacity retentions due to a high dissolution tendency. For OEMs, the easiest way to combat dissolution issues is polymerization.

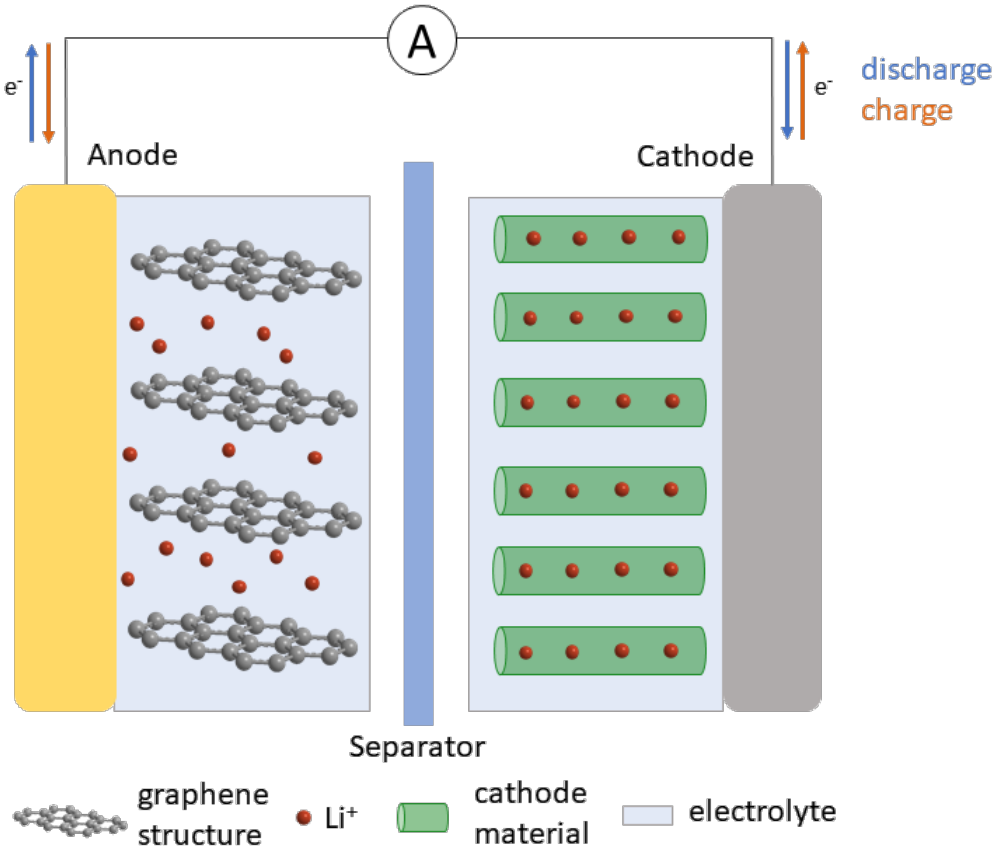

Fig. 2.4 Schematic representation of a lithium ion battery (LIB) based on a graphene/Li-metal oxide cell. During discharging, the Li^+ ions (red) in the graphene are intercalated into the cathode. While charging, the opposite reaction takes place and the Li^+ ions move from the metal oxide through to the anode site.

Polymer OEMs are significantly more stable than small molecule OEMs and can contain different types of redox centers (n-, p- and bipolar-types, see chapter 2.2.1).

2.4.3 Fully Organic Batteries

In the previous section (2.4.2) the main disadvantages of Li-, and more generally, metal-containing batteries were discussed. The important advantages, that can be offered by transitioning to fully organic battery systems are

1. inexpensive and (prospectively) renewable raw materials
2. light-weight and flexible components

3. chemically modifiable active materials
4. good processability
5. safe (no metal burning)
6. high rate performance.

The first fully-organic battery was developed in 2009.[10] This achievement was preceded by the report of the first organic radical cathode in 2002 and subsequent studies to improve and develop more radical polymers as promising materials.[60,93–96] Even though the aquired voltage was relatively low (0.6 V vs. Ag/Ag^+), it could be demonstrated that the manufacturing of fully organic, light-weight and flexible batteries without metal-containing electrodes was possible. The follow-up full organic radical battery only two years later was improved in many aspects from the first one, e.g., the cell voltage was improved from 0.6 V to 1.3 V (vs. Ag/Ag^+) and the bipolar redox behaviour of poly(nitronylnitroxylstyrene) allowed for a symmetric configuration, which was greatly simplifying the battery composition.[68]

Even though radical polymers show fast electron transfer kinetics and good cycling stability, their specific capacity is generally low compared to e.g., carbonyl polymers like quinone or imide-based polymers. Especially benzoquinone derivatives have been shown to perform remarkably well as cathode materials with initial capacities of 358 $\mathrm{mA\,h\,g^{-1}}$.[97] The development of all-organic batteries gained momentum in the last years and the design of symmetric batteries using one polymer for both electrodes (like polyparaphenylene, poly(2,3-dithiino- 1,4-benzoquinone) etc.) showed significant benefit in terms of the battery design.[98,99] Unfortunately, the big drawback of symmetrical polymer batteries is their relatively poor cycling stability despite showing high rate capability and stability in half-cell tests for the separate electrodes. The main issue for this phenomenon is the limited chemical stability of these polymers towards the generated high voltages in the full battery cell. A more stable symmetric polymer battery from a dual redox-active polyimide copolymer was developed based on naphthalene and phenothiazine units.[100] It could be charged to 1.7 V and showed stable long-term cycling with a capacity retention of 94 % after 1000 cycles. This progress showed a promising perspective for future developments in the field of symmetric polymer batteries. While the outlook for future full-polymer batteries is encouraging, there are a lot of

difficulties to overcome. On top of already mentioned limitations, the commonly praised sustainability of organic batteries has its limitations.[101] According to a recent life cycle assessment of all-organic batteries based on redox polymers, the synthesis process was identified as the major contributor to a negative environmental impact. Long and complex synthesis steps for the redox polymers, especially when high amounts of solvents or metal catalysts are required, produce a lot of waste and contribute heavily to the environmental impact. Therefore, redox polymers that enable simple, catalyst-free and low-energy synthesis need to be more emphasized. Beside the decreased environmental impact, these polymers would be more accessible due to the reduced required synthetic effort.

2.5 Introduction to Cyclopropenium (CP) Cations and their Special Status

With the synthesis of the s-triphenylcyclopropenyl cation in 1957, the first non-benzenoid aromatic compound was reported.[102] Before it was successfully synthesized, the existence of small cyclic two-electron aromatics was only predicted *via* the linear combination of atomic orbitals (LCAO) method, developed by Hückel.[103,104] By verification of the LCAO predictions for cyclopropenium (CP) cations, a simple way to assess new aromatic ring systems was confirmed and lead the way for many more to be synthesized. One outstanding property of the CP aromatics is their cationic nature. Since they form salts, their chemical and physical properties are also more similar to salts then to molecules. In comparison to triphenylmethyl bromide, the special stability of triphenyl-CP bromide is shown by the lack of strain that would be expected in such small rings and a very low pK_{a}in ethanol.[105] Further studies on the CP stability by adopting a value called pK_{R^+} (the pH of 50 % ionization of an alcohol R-OH and its carbonium ion R^+) revealed that in comparison to the naked CP cation, the introduction of phenyl-groups (Ph) significantly enhanced their stability.[106]

$$\mathrm{R^+} \underset{\mathrm{H_2O}}{\overset{\mathrm{K}}{\rightleftharpoons}} \mathrm{R{-}OH + H^+} \qquad \{6\}$$

$$\mathrm{p}K_{R^+} = -log\ \mathrm{K}$$

Complementing studies showed that alkyl substituents have an even better stabilizing

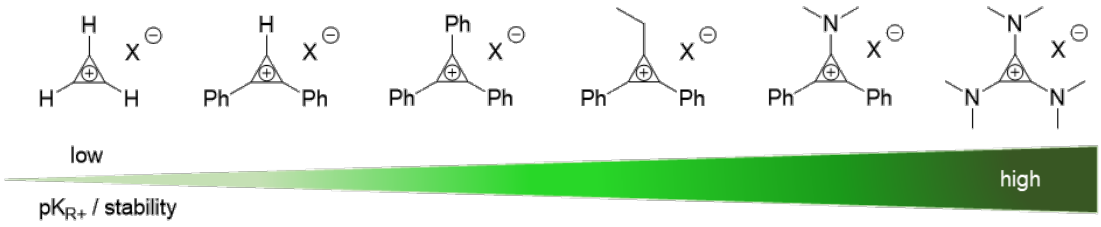

Fig. 2.5 Substituent effects on the stability of the CP cation. The stabilities were determined by the CPs pK_{R^+}-values (increasing stabilizing effect / pK_{R^+}-values of the substituents from left to right).

effect and the substitution of one Ph-group already led to a more stablized CP cation than triphenyl-CP.[107] An especially high degree of stabilization is introduced into CP cations by aminogroups and their strong electron-donating π-conjugative effect.[22,108] The introduction of just one amino-substituent is surpassing the stabilization offered from one alkyl-substituent (see Fig. 2.5). Due to this impact, amino cyclopropenium cations (ACPs) occupy a special position amongst CP cations and are employed in ionic liquids, organocatalysts and transition metal ligands.[109–113] Additionally, ACPs are relatively easy oxidized to their respective ACP radical dications, e.g., the radical dication of dimethyl-ACP (see Scheme 2.3, molecule $\mathbf{1}^{+\cdot}$) was isolated as red crystals and showed a high stability on air for several hours.[114,115] This high stability is remarkable for radicals and the electrochemical oxidation from dimethyl-ACP to form the radical was reversibly achieved at a redox potential of 1.12 V (vs. SCE).[116] In recent years, the reversible oxidation of ACPs was utilized to employ ACPs as new catholytes in nonaqueous RFBs.[25] It was shown that especially diisopropyl-ACP (see Scheme 2.3, molecules **2**) displayed a remarkable cycling stability with only a little loss of storage capacity after 200 cycles in acetonitrile (MeCN). Stability tests of the radical dication (after electrochemical oxidation to obtain a red solution) in dry MeCN showed a very high stability over several days at room temperature, while the radical quickly degraded (observable as bleaching of the red color) in contact with water. Since then, more research was carried out in the area of CP-based catholytes and it is safe to assume, that CP cations are establishing themselves as a very promising new class of organic catholytes.[26,27,78,117] To extend the application of ACPs in ROMs, the incorporation into polymers is a consequential step. In recent years a number of ACP polymers were

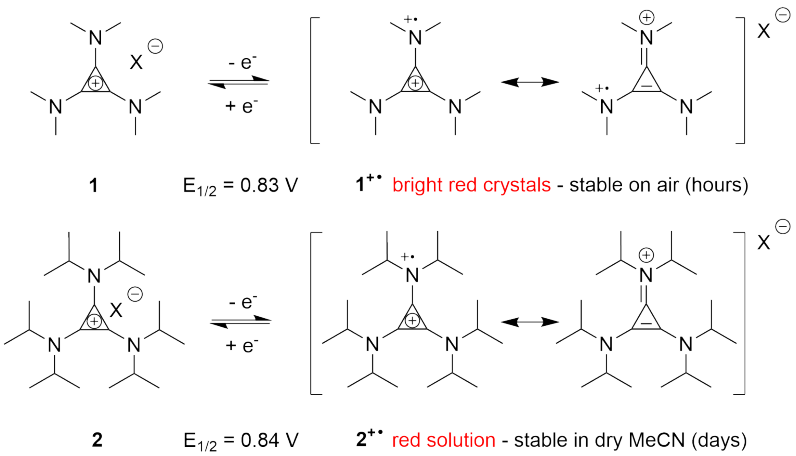

Scheme 2.3 Selected ACPs and their redox potentials $E_{1/2}$ (vs. Fc/Fc^+).[25] Dimethyl-ACP **1** (upper side) and diisopropyl-ACP **2** (bottom). Both radical dications $\mathbf{1}^{+\cdot}$ and $\mathbf{2}^{+\cdot}$ show remarkable stability on air and solution, respectively.

reported and examined as drug delivery vectors, ionic liquids, polyelectrolytes, catholyte polymers for non-aqueous RFBs and many more.[118–123] Even though these polymers all show promising properties in regard to the specified applications, the synthetic effort required to obtain these ACP polymers is high and therefore not suited for an industrial and commercial use. Only recently, ACP polymers with a simple one-step synthesis were reported and tested as polymer electrolytes for all-solid-state Li−S batteries.[124,125] In the section 3.1, ACP polymer networks from diaminoalkanes are presented and their structure discussed on the example of the *N,N'*-dimethyl-1,6-hexanediamine ACP network.

2.6 Introduction of Squaric Acid Amides (SAAs)

The first preparation of 3,4-diaminocyclobutene-1,2-diones or squaric acid amides (SAAs) was reported in 1966 from squaric acid (SA) methoxy esters.[24] As a new class of molecules, their chemical and physical properties were generally investigated but not much attention was given to their electrochemical properties.[23,126,127] The only electrochemical investigations on SAAs were done in 1977 by Hünig and coworkers, showing that the SAA molecules **1**, **2**, **3** and **4** (see Scheme 2.4) exhibit reversible redox reactions at potentials above 1.0 V vs. Ag/Ag^+. Interestingly, the aryl groups significantly elevate

the redox potentials of **1** and **2** in comparison to **3** and **4**. After these basic electrochem-

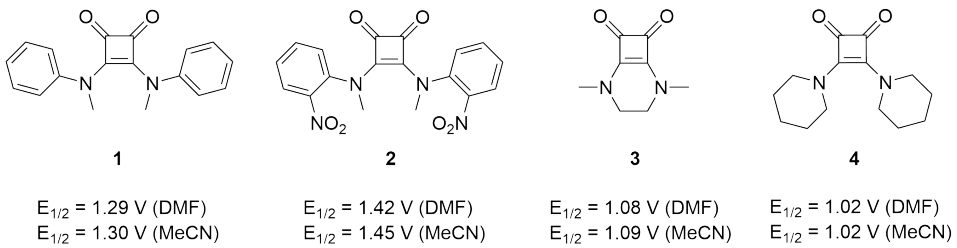

Scheme 2.4 Redox properties of the SAA molecules **1**, **2**, **3** and **4** reported by Hünig.[28] The potentials are given versus Ag/Ag^+.

ical tests, there have not been any further investigations on SAA molecules, to the best of our knowledge, especially after the related squaraine molecules got attention as new, potent cyanine dyes with application in solar cells and biomedical fields.[29,30,32,128,129] In section 4.1, the electrochemical and physical properties of a new cyclic SAA molecule, 2,5-diphenyl-2,5-diazabicyclo[4.2.0]oct-1(6)-ene-7,8-dione (DDD), are investigated and tested towards the application in battery systems. Afterwards, section 4.2 covers the synthesis and properties of SAA containing polymers.

2.7 Historical Contexts of the Squaric Acid Quinoxaline (SQX) Moiety

The first squaric acid quinoxaline (SQX) was first synthesized in 1968 by condensation of squaric acid (SA) and o-phenylenediamine to obtain SQX-H.[34] Shortly after, it was shown that this SQX moiety could also be synthesized from 3,4-diethoxycyclobutene-1,2-dione instead of SA due to the high ring formation tendency and SQX-Hs structure was confirmed by IR and elemental analysis.[130,131] Important properties of this compound were mentioned to be the striking dark red color and the high melting point T_m at 330 °C. The electrochemical behavior of some SQX molecules was examined by Hünig and Pütter in 1977 and they showed that the cyclic voltammetry (CV) of SQX-H displays irreversible anodic and cathodic peaks, however interestingly enough, the overall electrochemical process is reversible.[28] The explanation for this behavior was a quick proton transfer from SQX-H to the solvent medium (see Scheme 2.5, left). At 0.64 V

vs. Ag/Ag^+, SQX-H gets irreversibly deprotonated and oxidized to SQX-ox. At lower potentials, SQX-ox then subsequently gets reduced to the semiquinone SQX-sem which is then followed by a reduction and simultaneous protonation to SQX-H at 0.05 V vs. Ag/Ag^+ (see Scheme 2.5).

Interestingly, the substitution of the secondary amide positions *N* and *N*' with methyl groups solves the proton transfer issues and the electrochemical oxidation becomes reversible (see Scheme 2.5, SQX-Me). The formed radical cation SQX-Me^+ was even stable enough to be isolated as a perchlorate salt.[127]

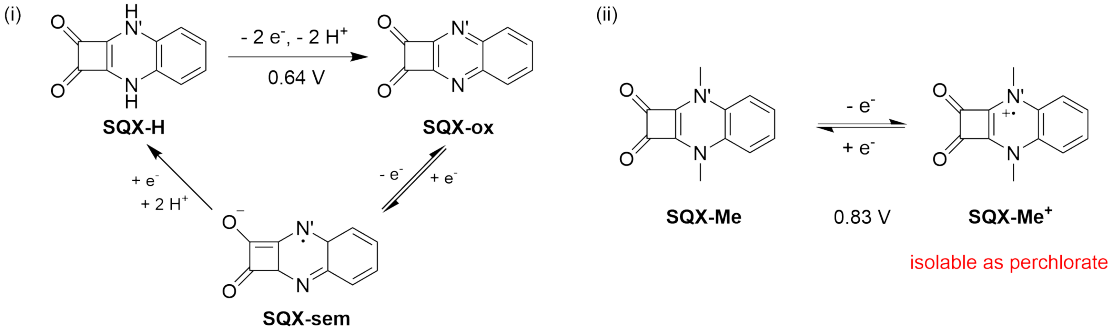

Scheme 2.5 Electrochemical behavior of SQX-H and SQX-Me.[28] Left side (i): SQX-H undergoes a electrochemical (irreversible) oxidation at 0.64 V, coupled with a rapid deprotonation to SQX-ox. SQX-ox can be reversibly reduced to SQX-sem, which gets further reduced (and simultaneously protonated) to SQX-H at 0.05 V. Right side (ii): SQX-Me shows a reversible oxidation without rapid proton transfer at 0.83 V. The radical cation SQX-Me^+ could be isolated as a perchlorate salt.[127] All redox potentials are given versus Ag/Ag^+.

It was generally observed that the SQX moiety seems to be very stable since attempts to further condensate SQX-Me with o-phenylenediamine under harsh conditions (up to 180 °C with addition of strong acids) failed and the molecule remained unchanged.[132] Despite those interesting findings, SQX molecules have remained largely overlooked as potentially promising ROMs for the use in energy storage systems.

In the sections 5.1 and 5.3, new SQX molecules and polymers will be presented and evaluated in regard to their electrochemical properties and potential for future applications.

3 Aminocyclopropenium Cations (ACPs)

3.1 Synthesis and Structural Investigations of Simple ACP-Networks

Inspired by the successful implementation of amino cyclopropenium cation (ACP) molecules in non-aqueous RFBs, herein the goal was to synthesize polymers containing ACP funtional groups for application in energy storage. The benefit of a polymeric system would be a better processability and mechanical stability compared to small molecules. To verify the reversible redox properties reported in literature, two sim-

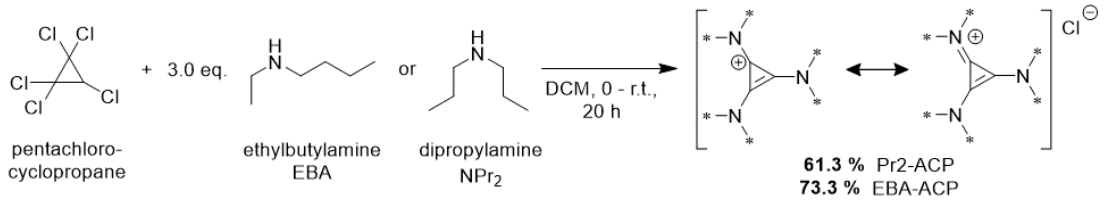

Scheme 3.1 Synthesis of the ACP molecules EBA-ACP and Pr2-ACP from pentachlorocyclopropane (PCCP) in two one-step reactions, respectively. The symmetric ACP salts were obtained in good yields.

ple and symmetrical ACP molecules were synthesized with ethylbutylamine (EBA) and dipropylamine (NPr_2) in two straightforward one step reactions, respectively (refer to Scheme 3.1). The cyclopropene core of the ACPs was provided by pentachloropropane (PCCP) as the starting material. With each amine substitution, chlorides were simultaneously eliminated from the core. At one point, the single proton in PCCP was removed *in situ* and the aromatic cyclopropenium (CP) core was formed. NMR spectroscopy was used to determine the successful synthesis of the ACP molecules (see Fig. 3.1). Since the cyclopropenium core didn't have covalently attached protons, ^{13}C NMR was measured additionally to verify the presence of the intact CP in the products.

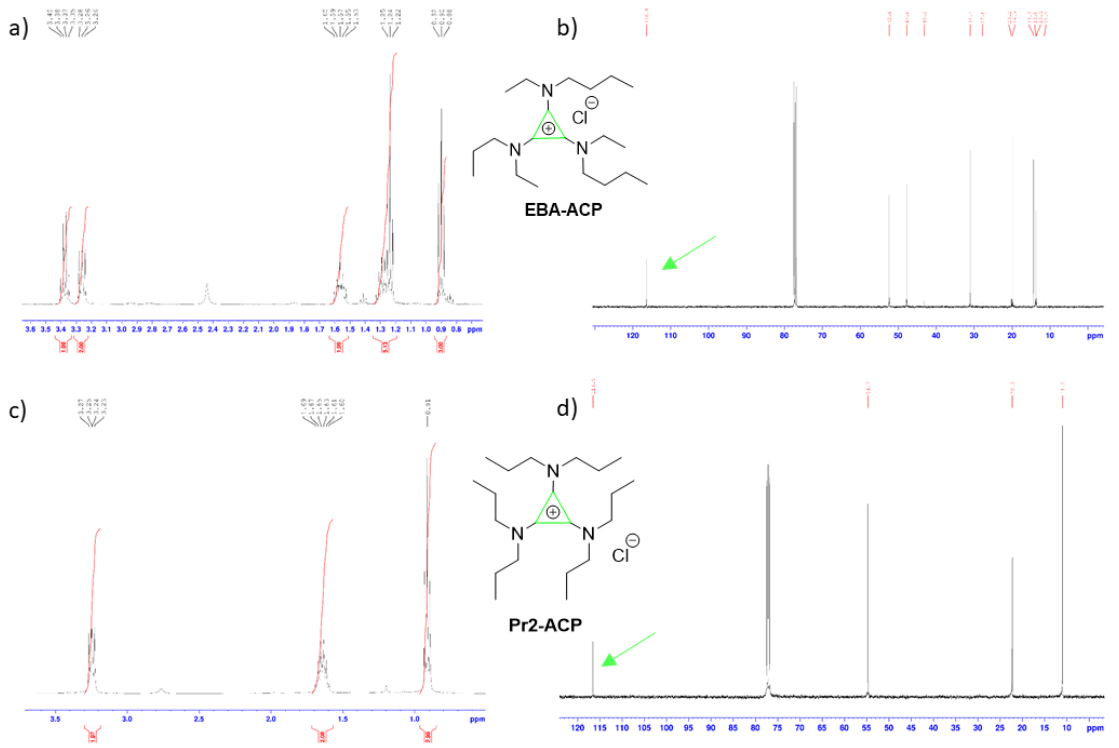

Fig. 3.1 NMR spectra (^{1}H and ^{13}C) of EBA-ACP and Pr2-ACP. a) Proton spectrum of EBA-ACP (400 MHz, $CDCl_3$). The signals of the ethyl- and butyl-groups on the amines were well resolved and could be matched clearly (see experimental). b) Carbon spectrum of EBA-ACP (100 MHz, $CDCl_3$). The signal at 116.4 ppm (marked with a green arrow) clearly indicated the presence of intact CP. c) Proton spectrum of Pr2-ACP (400 MHz, $CDCl_3$). The propyl-groups were well resolved and could be matched clearly (see experimental). d) Carbon spectrum of Pr2-ACP (101 MHz, $CDCl_3$). The signal at 116.5 ppm (marked with a green arrow) clearly indicated the presence of intact CP.

Both ACPs were dissolved in dry electrolyte (0.1 M tetrabutylammonium perchlorate (TBAP) in acetonitrile (MeCN)) and cyclic voltammetry (CV) was measured to assess the redoxactivity of these molecules in solution. From CV it could be shown clearly that both ACP molecules displayed very reversible oxidations in acetonitrile with high redox potentials at 1.31 V (EBA-ACP) and 1.34 V (Pr2-ACP) vs. Ag/Ag^{+}. The high reversibility of the redox reactions was also shown as the responding currents remained stable with each CV cycle. From these results it was anticipated that symmetrical two-dimensional networks with intact ACP moieties would show the same redoxactivity and high reversibility in CV.

Therefore, to synthesize a polymeric network, pentachlorocyclopropane was again used

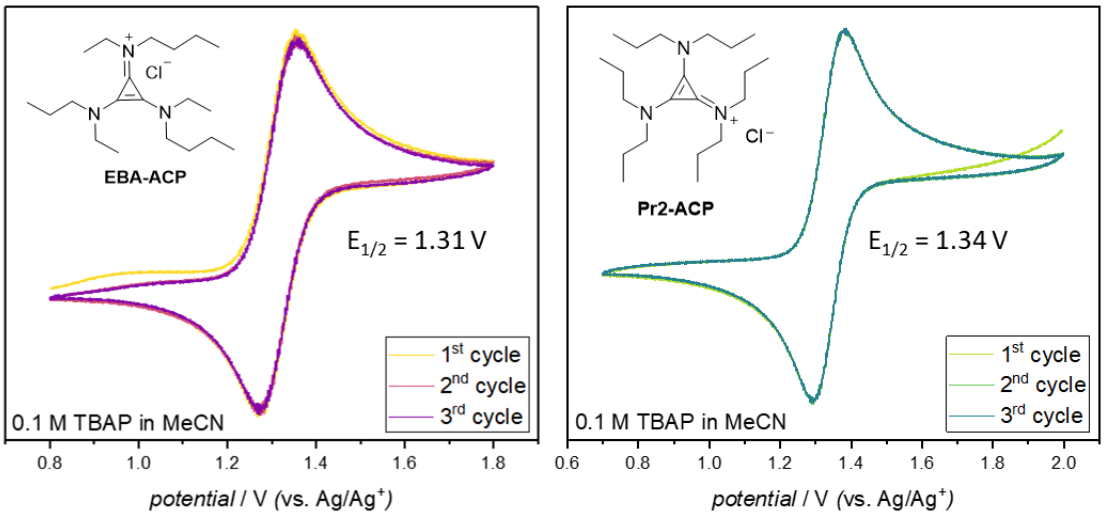

Fig. 3.2 Cyclic voltammograms of the ACP molecules EBA- and Pr2-ACP in acetonitrile. The cyclic voltammetry (CV) spectra were recorded over three cycles with a scan rate of 100 $\mathrm{mV\,s^{-1}}$. The potentials were referenced against Ag/Ag^{+}.

as the starting material (see Scheme 3.3). To build the polymeric structure, diamines with different linker lengths from C2 to C6 were used to build up the ACP network, namely *N,N*'-dimethylethylenediamine, *N,N*'-dimethylpropylenediamine and *N,N*'-dimethyl-1,6-hexanediamine. Primary amines were avoided as linkers to make sure that all amino moieties inside of the networks would be alkylated. The depicted networks AC2, AC3 and AC6 were chosen due to their simple structure and straight-forward synthesis with commercially available chemicals. Firstly, pentachlorocyclopropane (PCCP) was synthesized from trichloroethylene and sodium trichloroacetate according to the method from Tobey and West (Scheme 3.2).[133]

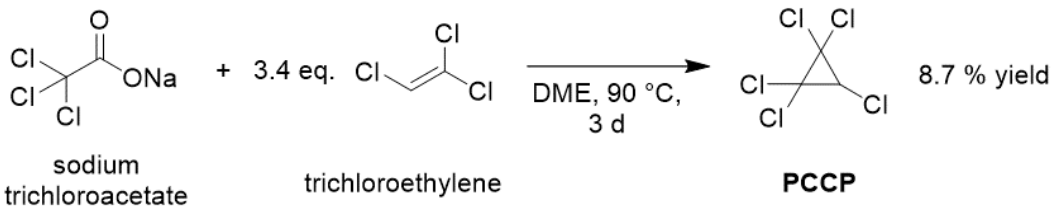

Scheme 3.2 Synthesis of pentachlorocyclopropane (PCCP). The synthesis was adapted from a protocol from 1966 and the low yield could be mainly attributed to the purification step (fractional distillation).[133] The recorded NMR data were in accordance to those reported in literature (see experimental).[134,135]

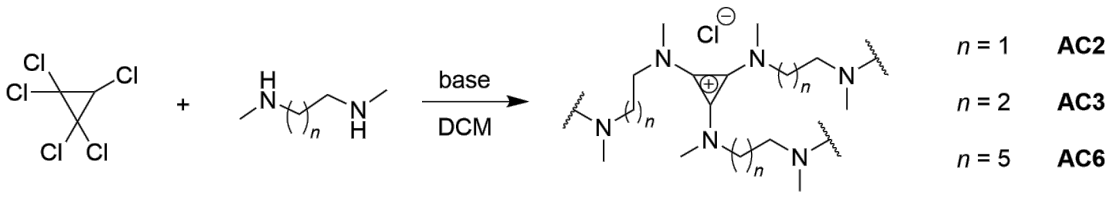

Scheme 3.3 General synthesis of the ACP networks. The diamine linker lengths vary from ethyl (C2) to hexyl (C6).

For the ACP network formations, PCCP and the above mentioned diamines were mixed and reacted together with addition of triethylamine (TEA) to obtain the networks AC2, AC3 and AC6 (Scheme 3.3). The successful synthesis was shown by NMR and FTIR (experimental data 7.1.2.1) and the thermal stability was evaluated by TGA (Fig. 3.3). From optical evaluation, it was noticed that the networks were highly hygroscopic. After leaving the AC-products exposed to ambient atmosphere, the consistency of the dried ACs would change from solid to gel-like, indicating the absorption of moisture from the environment (see Fig. 3.3). This observation was interesting as this behavior had not been mentioned for other ACP polymers in literature.

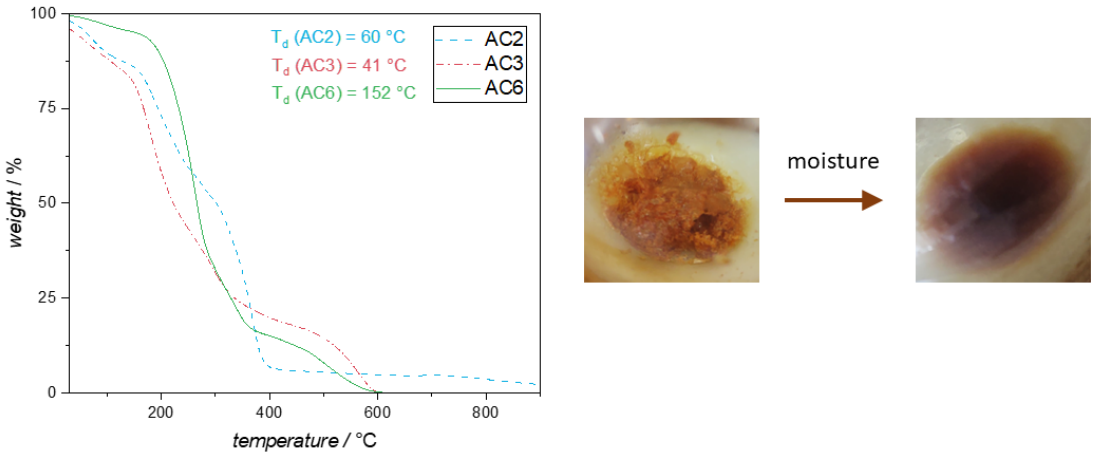

Fig. 3.3 Thermal stability determined by TGA (left) and hygroscopicity (right) of the ACP networks AC2, AC3 and AC6.

The hygroscopicity might be the reason for the low thermal stability of all ACP networks, especially AC2 and AC3 (Fig. 3.3 with decomposition temperatures T_ds (where 5 % of the substance is decomposed) of 60 °C and 41 °C, respectively. The steep decomposition

curve until around 200 °C indicated solvent residues in the ACs. In contrast to this, the decomposition temperature of AC6 is much higher at 152 °C while overall showing the same decomposition behavior like AC3.

To verify that the synthesized network structures contained intact ACP moieties, a cross polarization heteronuclear correlation (CP HETCOR) 2D solid-state NMR experiment was carried out with vacuum-dried AC6 to investigate the ACP network. In this NMR method, two dimensions were coupled to each other, the first dimension was the chemical shift of one nucleus (here proton) and the other dimension was the chemical shift of another nucleus (here carbon-13).[136] The information derived from this spectrum could be used to assign C atoms and their directly attached protons, unfortunately this method is less sensitive compared to methods using indirect nuclei detection like heteronuclear single quantum coherence (HSQC). Nevertheless, from the 2D-NMR spectrum (Fig. 3.4),

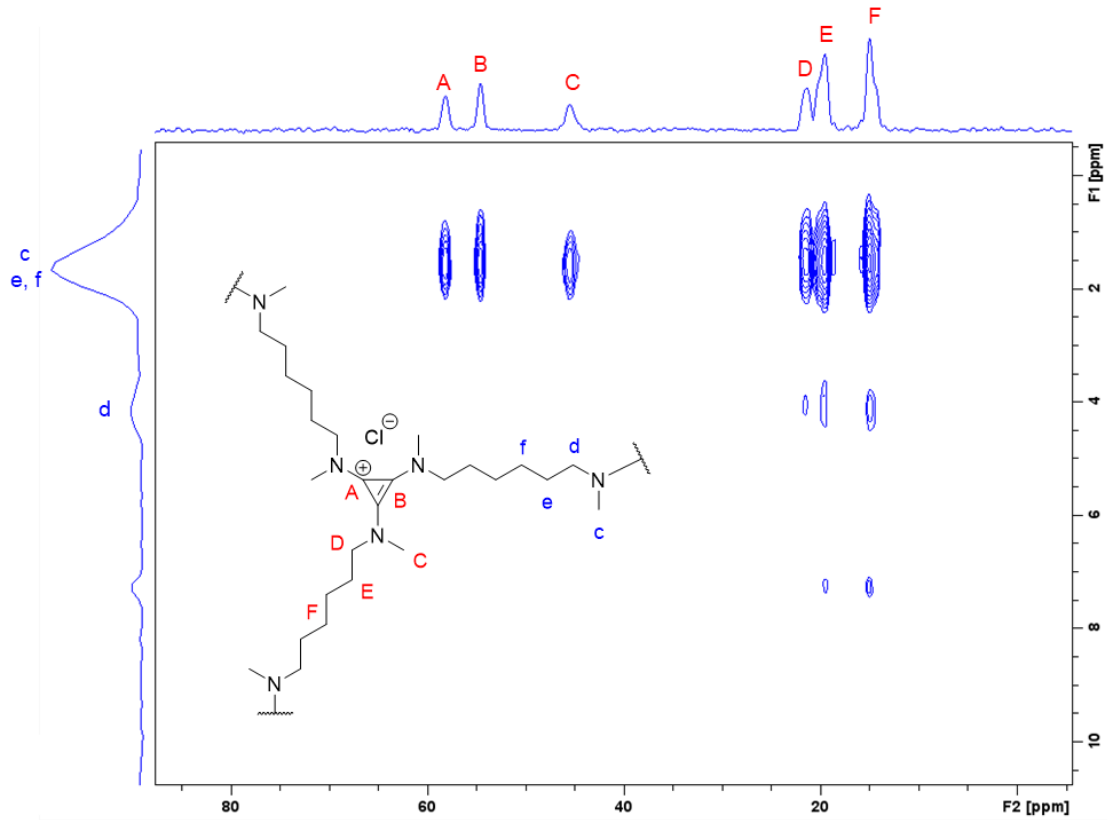

Fig. 3.4 2D-solid-state NMR CP-HETCOR experiment of AC6. The carbon spectrum is displayed on the x-axis (signals marked in red capitals) and the correlating proton spectrum is displayed on the y-axis (signals marked with blue letters).

the intact structure of the ACP ring carbons in AC6 could be shown clearly. The signals A and B were correlated to the cyclopropenium carbons with A corresponding to the carbocation and B to the unsaturated carbon atoms in the CP core. Further, if the ACP structure was not intact, e.g., through ring opening side reactions, this would be apparent through the presence of an additional carbon signal with a similar chemical shift and relative integral as A and B. Therefore, it could be shown nicely that the proposed ACP networks were synthesized successfully without decomposition of the CP rings.
After confirming the intact structure of the ACP ring in the networks, the electrochemical properties of the networks in solution were tested. Unfortunately, the high reversibility

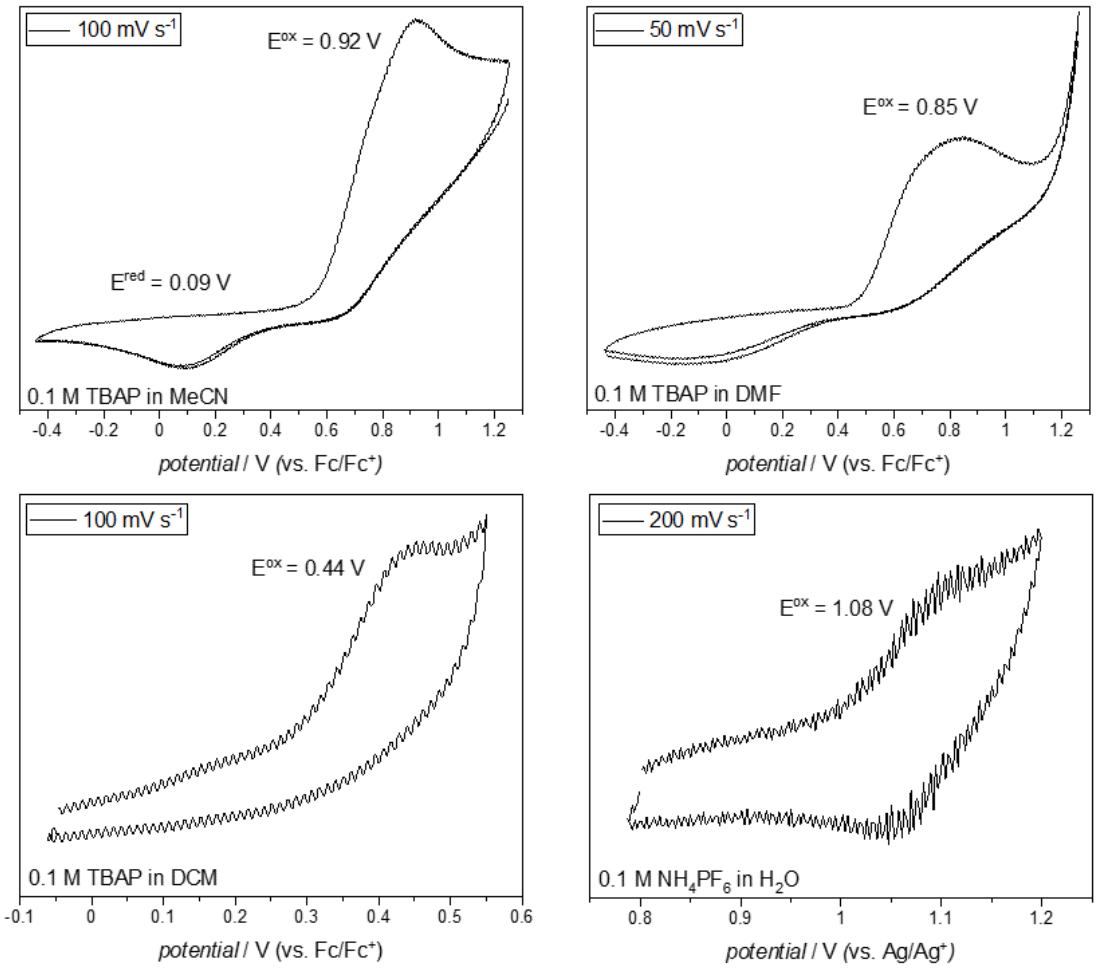

Fig. 3.5 Cyclic voltammograms (CVs) of AC6 in different solutions with 0.1 M concentrated electrolyte solutions recorded at different scan rates. The CV measured in water could not be referenced to ferrocene because of insolubility.

of the redox reaction in single molecule ACPs could not be observed in any of the ACP networks (see Fig. 3.5 and experimental). In DCM, DMF and MeCN the CVs of AC6 showed irreversible oxidations at high potentials of up to 0.9 V vs. Fc/Fc^+. While the high oxidation was expected from the previous results obtained by CV of the molecules EBA- and Pr2-ACP, the irreversible nature of this reaction was surprising. Since the irreversible oxidation was not only observed in one solvent, it can be assumed that the formation of the ACP networks influenced the environment and redox stability of the ACP moieties significantly. One reason for the irreversible oxidation could be that the positive charge remaining after the oxidation would be rapidly distributed throughout the network to stabilize the system. Therefore the reduction would need to occur at much lower potentials to reduce the stabilized network. The observed reduction signal at 0.09 V vs. Fc/Fc^+ (in MeCN) would support this theory as the reduction potential was negatively shifted by more than 0.8 V. Interestingly, in DCM the oxidation potential of AC6 was cut to less than half of the potential in acetonitrile (0.44 V). Additionally, the responding current was also much lower which could be attributed to the poor solubility of AC6 in DCM.

Since the ACP networks were highly hygroscopic, it was attempted to record a CV in water to examine if the redoxactivity was preserved in an aqueous solution. Since ferrocene was not soluble in water, the potential could not be referenced to Fc/Fc^+. The recorded redox reaction of AC6 in water (see Fig. 3.5, bottom right) seemed to be reversible at the first glance but since the responding current was very low it couldn't be determined clearly if the observed signal was an actual redox event instead of an artefact. Due to these results, it could be concluded that these networks are not suitable materials for redox applications.

In summary, from the results of the redox properties of the symmetric ACP small molecules EBA-ACP and Pr2-ACP it was assumed that a polymeric network consisting of symmetric ACP moieties should perform in a similarly reversible manner. To test this hypothesis, three simple ACP networks with different diamine linkers were synthesized and examined *via* cyclic voltammetry. It was noted, that the ACs redox potentials became irreversible in all tested solutions. The reason for this was assumed to be a delocalized stabilization of positive charge in the AC networks after the electrochemical oxidation. To reduce this stabilized system again, a more negative potential would be required since

the reduction sites are not localized anymore. Therefore, the corresponding reduction signal was greatly shifted to lower potentials. To sum up, it can be concluded that the synthesized ACP networks didn't show promising properties as new redox-active materials.

4 Squaric Acid Amides (SAAs)

4.1 Exhaustive Investigations of the Cyclic DDD as an Organic Cathode Material for LIBs

The condensation of SA with N-N'-diphenylethylene-1,2-diamine yielded the cyclic SAA 2,5-diphenyl-2,5-diazabicyclo[4.2.0]oct-1(6)-ene-7,8-dione (DDD) cleanly in an one-step reaction as a white powder (Fig. 4.1). To confirm the successful synthesis of DDD, the product was analyzed *via* nuclear magnetic resonance (NMR) (^{1}H, ^{13}C), Fourier transform infrared (FTIR), atmospheric pressure chemical ionization (APCI) mass spectrometry (MS) and elemental analysis. The most significant spectra are displayed in Fig. 4.1 (proton and carbon NMR) and Fig. 4.2 (APCI-MS).
In the proton spectrum, the signals were assigned to the phenyl and bridging alkyl groups. While the signals a and d (Fig. 4.1, left) could be assigned distinctively, the aromatic signals b and c were overlapping into a broad multiplett. Since the squaric acid moiety didn't have any covalently linked protons, ^{13}C NMR was measured additionally to identify the cyclobutenone group. The carbonyl-Cs A and alkene-Cs B (179.6 ppm and 165.1 ppm, Fig. 4.1) were clearly visible and confirmed the proposed cyclic structure of DDD. Since NMR is a qualitative analysis method and not suitable to distinguish between a single molecule and other possible cyclic oligomers exhibiting the same signals, mass spectrometry was applied to verify DDDs structure. In Fig. 4.2, the APCI-MS spectrum of DDD is displayed. The calculated relative intensity of the m/z signals were in good agreement with the measured values, with 290.4 m/z being the main signal (only 0.1 % deviation from the calculated value of 290.11 m/z). This result further validated the structure of DDD as the proposed cyclic SAA molecule with the chemical formula $C_{18}H_{14}N_2O_2$. Therefore, the structure of DDD could be confirmed qualitatively as well as quantitatively. Additional analysis data are summarized in the experimental part.

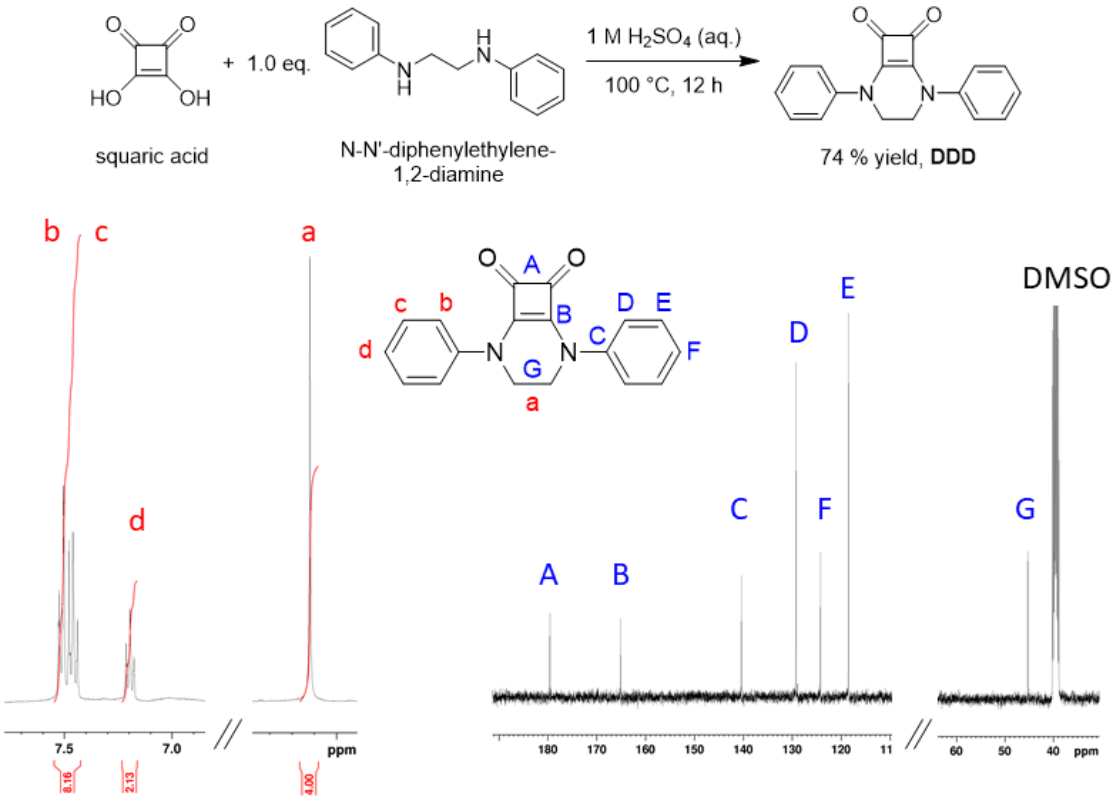

Fig. 4.1 Synthesis and NMR characterization of DDD. The successful synthesis was verified by ^{1}H (left side) and ^{13}C-NMR (right side) in deuterated DMSO. The proton signals (red letters) and carbon signals (blue capitals) could be assigned clearly to the proposed DDD structure.

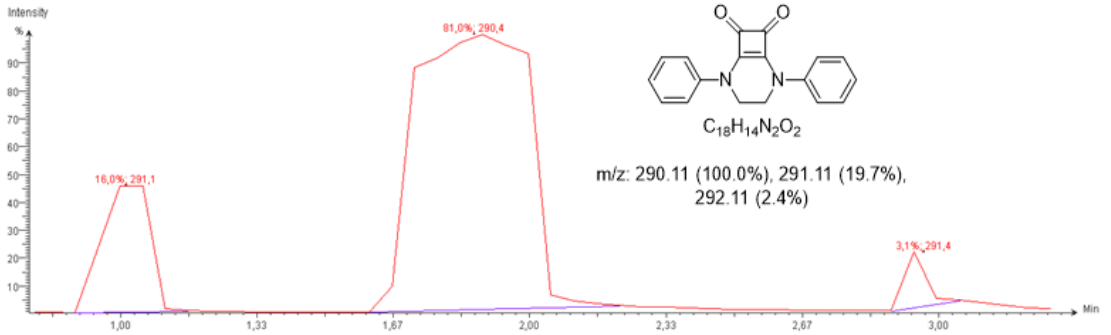

Fig. 4.2 APCI-MS spectrum of DDD. The measured spectrum was in good agreement with the calculated theoretical m/z (mass per charge) distribution. Only 292.11 m/z was not visible in the spectrum.

This new SAA was only badly soluble in a range of organic solvents, including methanol, tetrahydrofurane and DCM. The following section discusses DDDs properties in detail, all radical stability tests *via* EPR and UV-Vis and the single crystal diffraction were carried out by M. Baumert at TU Dortmund, while all half-cell testings (including CVs in electrolytes and scanning electron microscopy (SEM)) were conducted by P. H. Su at Helmholtz Institute Ulm (HIU).

The cyclic structure of DDD was confirmed by qualitative analytics including NMR, FTIR and APCI-MS and the thermal properties of DDD appeared to be very promising. DDDs decomposition temperature exceeded 300 °C and differential scanning calorimetry (DSC) showed that DDD had a very high melting point T_m at 274 °C (see Fig. 4.3) and recrystallized fully at T_c = 258 °C. This high crystallization tendency indicated a strong interaction and order between the molecules and could also be verified by single crystal diffraction (Fig. 4.3, top right) and powder X-ray diffraction (XRD).

In CV, DDD showed a reversible redox reaction with a redox potential at 0.72 V (vs. Fc/Fc^+) as seen in Fig. 4.3 (bottom left). To confirm the structure of the formed radical cation, DDD was chemically oxidized to $DDD^{+\cdot}$ and characterized *via* electron paramagnetic resonance (EPR) spectroscopy. The hyperfine coupling indicated that the radical was located on one of the nitrogen atoms and was in good agreement with the calculated spectrum (see Fig. 4.3, bottom right). Further stability tests of $DDD^{+\cdot}$ in acetonitrile (MeCN) by observation of the radical absorption band at 819 nm *via* UV-Vis showed that the radical cation was slowly degrading over the course of approx. four hours (see Fig. A.7).

These results were interesting as DDD appeared to be a promising organic cathode material. To figure out its behavior under battery conditions, electrodes with DDD as active material were prepared for electrochemical testing in a half-cell setup with Li metal as the anode. Interestingly, it was observed that the radical cation $DDD^{+\cdot}$ was considerably less stable in carbonate-based electrolytes, namely ethylene carbonate (EC) and dimethyl carbonate (DMC). Since the electrolyte composition can have a significant effect on the radical stability, DDD was tested in different alterations (varied ratios of EC and DMC and $LiPF_6$ concentration). One interesting effect that was observed during some CV measurements was a remarkable evolution of the redox peak. E. g., in 1 M $LiPF_6$ EC:DMC (50:50 wt %), also called LP-30, after the first oxidation, the following reduction peak was significantly sharpened and the specific current was much higher than

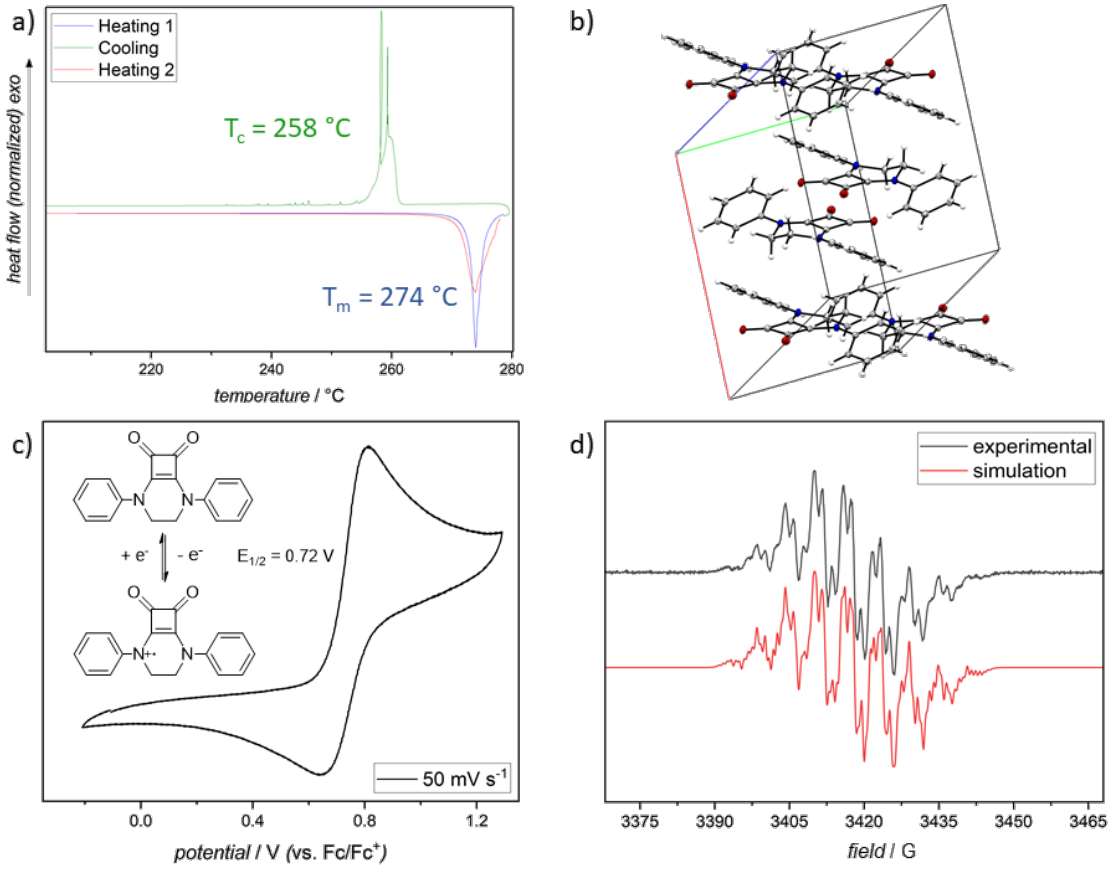

Fig. 4.3 Characterization of DDD. a) DSC heating and cooling curves of DDD showed a melting point T_m at 274 °C (in blue, endothermic) and crystallization point T_c at 258 °C (in green, exothermic). b) Single crystal diffraction of DDD. The single crystal was obtained from a saturated DMF solution. c) CV of DDD in DMF (0.1 M tetrabutyl ammonium perchlorate (TBAP)) recorded at a scan rate of 50 $\mathrm{mV\,s^{-1}}$. The redox potential $E_{1/2}$ = 0.72 V was referenced against Fc/Fc^+. d) EPR spectrum of $DDD^{+\cdot}$ (in black) and its calculated spectrum (in red).

during the oxidation (see Fig. 4.4). This sharpening remained for the redox peaks in the following cycles, therefore the first oxidation could be regarded as an activation step to homogenize the active sites in the cathode. It could be observed that this peak evolution occured in relation to the electrolyte composition. In a higher concentrated solution with 2 M $LiPF_6$ and EC:DMC 50:50 wt %, no peak sharpening could be found. At this salt concentration, the evolution only appeared again for a DMC content as high as 90- and 100 wt %. The correlation between the peak sharpening and electrolyte compositions seemed to be very complex since no clear trends couldn be observed for the occurrence of this evolution. Nevertheless, this effect indicated an underlying rapid redox process

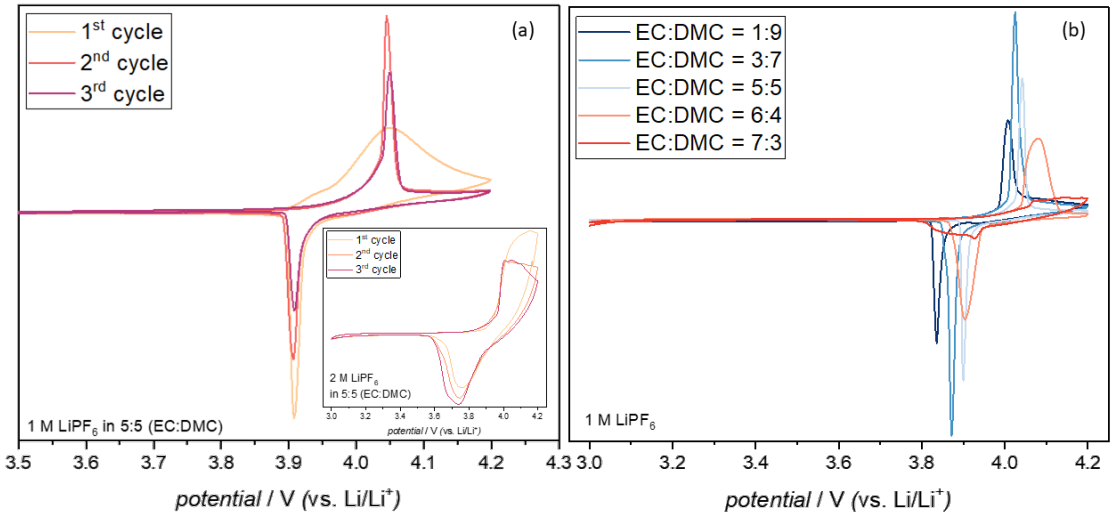

Fig. 4.4 Peak sharpening of DDD in CV after the first oxidation in carbonate electrolytes. (a) CV of DDD in 1 M $LiPF_6$ in 5:5 wt % EC:DMC recorded with a scan rate of 100 $\mathrm{mV\,s^{-1}}$. The unusual peak sharpening after the first cycle was clearly visible. Interestingly this sharpening was not present in the 2 M $LiPF_6$ solution. (b) CV curves of the second cycles of DDD in different 1 M $LiPF_6$ electrolyte solutions. In the electrolytes with the composition EC:DMC = 6:4 and 7:3, respectively, no peak sharpening could be observed.

that needed to be further examined.

In terms of cyclability, a very important factor was the solubility of DDD in the electrolyte since dissolution was one of the main issues leading to rapid capacity fading in organic batteries. Parameters that needed to be monitored over multiple cycles to estimate the cyclability of DDD were coulombic efficiency (CE) and specific capacity C_s. The CE is the fraction of the retained discharge charge and the charge applied in the same cycles charging procedure. Any value deviating from 1 is an indication for e.g., irreversible side reactions, crossover of material or other issues. The theoretical specific capacity C_s^{theo} of DDD was determined to be 96 $\mathrm{mA\,h\,g^{-1}}$ using the following equation:

$$C_s^{theo} = \frac{n \cdot F}{M}, \tag{4.1}$$

where n is the number of charge carriers, F is the Faraday constant and M is the molecular weight of the electroactive material[137]. In practice, only a fraction of the C_s^{theo} was achieved as the existence of inactive components (like binders or conductive materials) and inefficiencies (like resistance) lower the achieved capacity. Since DDD is an organic material, dissolution is a main concern for poor capacity retention[8]. During constant

current cycling at 50 $\mathrm{mA\,h\,g^{-1}}$, high initial capacities followed by rapid degradation could be observed for almost all electrolyte compositions in 1 M $LiPF_6$ (except for LP-30, see Fig. 4.5). In the higher concentrated 2 M $LiPF_6$ electrolytes, the initial specific capacities were improved and remarkably the CE of the cycling of DDD in EC:DMC = 5:5 was greatly enhanced compared to the cycling in the 1 M $LiPF_6$ electrolyte. After an optical examination of the cycled separators it was clear that dissolution of DDD was a main contributor to the poor CE in the 1 M $LiPF_6$ electrolyte.

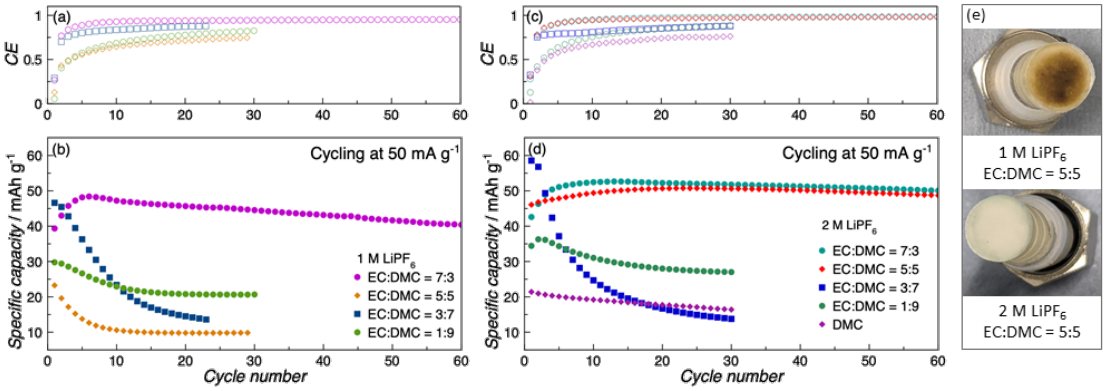

Fig. 4.5 Cycling of DDD in different electrolytes. The specific capacity evolution for up to 60 cycles is depicted in (b) for 1 M $LiPF_6$ electrolyte solutions with the corresponding CEs depicted in (a). For 2 M $LiPF_6$ electrolyte solutions the cycling behaviour is depicted in (c) and (d). The cycled separators of the EC:DMC = 5:5 electrolyte solutions with 1 M and 2 M $LiPF_6$, respectively, are depicted in (e). From optical comparison, the dissolution of DDD in the upper separator is apparent.

A number of other factors considered critical for the cyclability of DDD included the electrode morphology and the viscosity of the electrolytes. It was observed, that the surface of the electrodes in the well cyclable electrolyte compositions (e.g., 1 M $LiPF_6$ EC:DMC = 7:3) showed a mostly even distribution of DDD. This stood out especially when comparing with the surface of an electrode cycled in unsuitable electrolyte composites like 1 M $LiPF_6$ EC:DMC = 5:5 (LP-30, see Fig. 4.6). The surface of the electrode cycled in LP-30 showed a lot of formed clusters that were largely connected and covering the majority of the electrode. A possible implication, that the electrode morphology showed, was that an uniform deposition of DDD ensured a good contact between the active material and the conductive matrix, which was a crucial factor to maintain the discharge capacity. Therefore, a cluster-like deposition reduced the contact area of DDD

with the conductive matrix and caused poor cyclability. Intuitively, another relevant parameter was the electrolytes viscosity since this strongly influences the diffusion behaviour of DDD and $DDD^{+\cdot}$ during the charging and discharging cycles. A low viscosity could enable high diffusion and cause DDD to lose contact with the conductive matrix more easily. At the same time, high viscosity alone could not be the deciding factor, since the 1 M $LiPF_6$ EC:DMC = 7:3 electrolyte had a rather low viscosity but nevertheless showed a considerably good cyclability (compare Fig. 4.5 and Fig. 4.6). Therefore, to ensure a good cyclability, all of the above discussed parameters had to be balanced carefully.

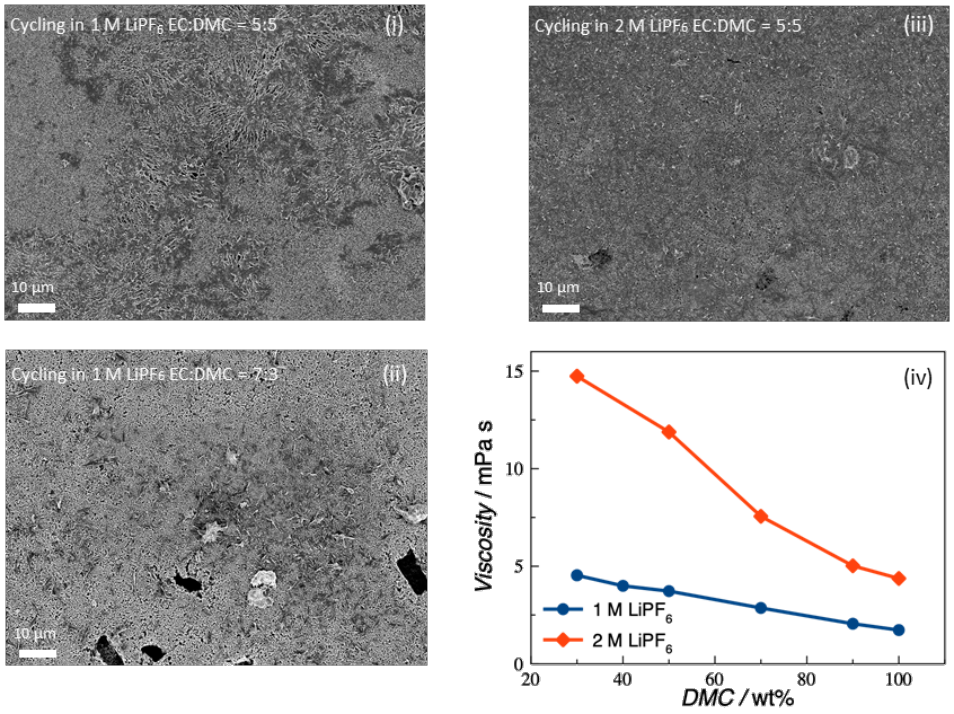

Fig. 4.6 DDD electrode surface morphologies and electrolyte viscosities. The surfaces were monitored after cycling *via* scanning electron microscopy (SEM). In (i) the formation of big, connected clusters could be seen for the electrode in 1 M $LiPF_6$ EC:DMC = 5:5 (LP-30). After cycling in EC:DMC = 7:3 (1 M $LiPF_6$), the electrode surface in (ii) showed patchy formation of clusters while the majority of the surface was even. Lastly, the electrode surface after cycling in 2 M $LiPF_6$ EC:DMC = 5:5 was very homogeneous and showed only isolated cluster formations. (iv) displayed the viscosities of the examined electrolyte compositions.

To examine the effect of the Li salt, $LiPF_6$ was exchanged with lithium bis(trifluoromethanesulfonyl)imide (LiTFSI) to investigate the redox activity. Interestingly, CV in

1 M LiTFSI EC:DMC = 5:5 showed an irreversible oxidation but in combination with 1 M $LiPF_6$, the same peak sharpening effect as in previous CVs could be observed and the oxidation became reversible. Increasing the concentration of LiTFSI to 2 M + LP-30, broadened the redox peaks again but the process stayed reversible. This result indicated, that PF_6^- anion was vital for the reversibility of the oxidation of DDD. In regard to cyclability, the addition of 2 M LiTFSI to LP-30 greatly enhanced the cycling and CE.

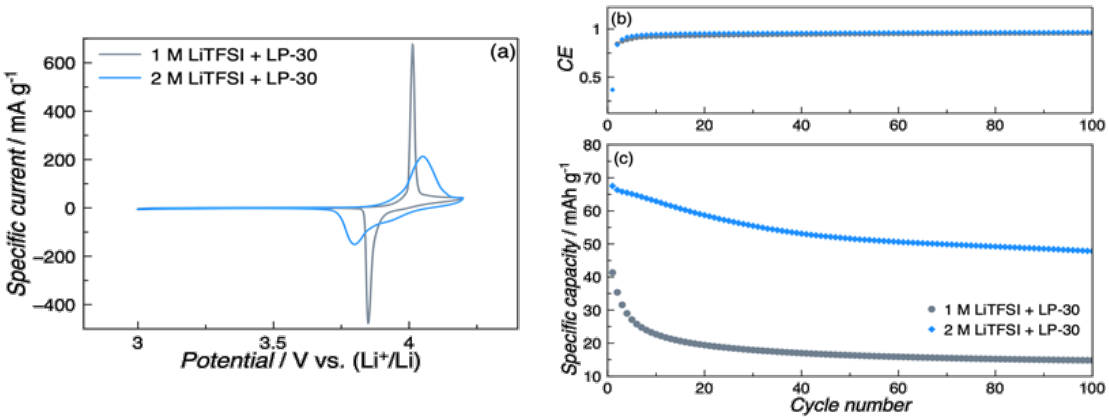

Fig. 4.7 DDD in dual-salt electrolytes. The CVs in (a) showed that the redox reactions are reversible and the cycling behaviour (in (b) and (c)) was greatly enhanced in 2 M LiTFSI + LP-30 with high specific capacities and CE.

4.2 Synthesis and Investigation of SAA Polymers and their Electrochemical Behavior

The most serious issue that was discovered during the investigation of DDD was its high dissolution in carbonate electrolytes. Even though this issue could be approached by tailoring the electrolyte, this is not an ideal solution to achieve a viable alternative to other cathode materials. It has been shown in previous studies that the increase of molecular weight by introduction of oligomers or polymers could circumvent the solubility issue organic electrode materials (OEMs) usually face and enhance the battery cycle life significantly.[97,138] Therefore, new polymers with SAA as functional redox groups were synthesized and examined in respect to their electrochemical performance.

4.2.1 Synthesis of SAA Monomers for Polymerization

To obtain SAA homopolymers, acrylamide based monomers were synthesized from squaric acid ethyl ester (SAE). The reason for selecting this type of monomers was that diamines with different chain lengths are readily available compounds, which should make a variation of the linker lengths in the monomers easily possible. However, the issues associated with this synthesis route were unwanted side reactions like substitution on both ester sides or intra- and intermolecular substitutions from the diamines. To compete with these unwanted reactions, the concentration, temperature and composition of the reaction mixtures had to be carefully adjusted. Additionally, one of the amino moieties on the diamine was substituted with the *tert*-butyloxycarbonyl (Boc) protecting group to avoid a second intramolecular substitution on the ethyl ester but this added two additional steps to the synthesis.

In total, four steps were required for the synthesis of the SAA acrylate monomers (Scheme 4.1). The following diamines were used for the monomer synthesis: 1,2-diaminoethane (C2H), *N,N*'-dimethylethylenediamine (C2M), 1,3-diaminopropane (C3H) and *N,N*'-dimethylpropylenediamine (C3M). Already in the first synthesis step clear differences in the reactivity of the amines were visible. While the methylated diamines were monoprotected in moderate to good yields (49 - 70 %, see Table 4.1), the yields for the primary diamines were much lower (21 - 27 % yield). This difference in reactivity

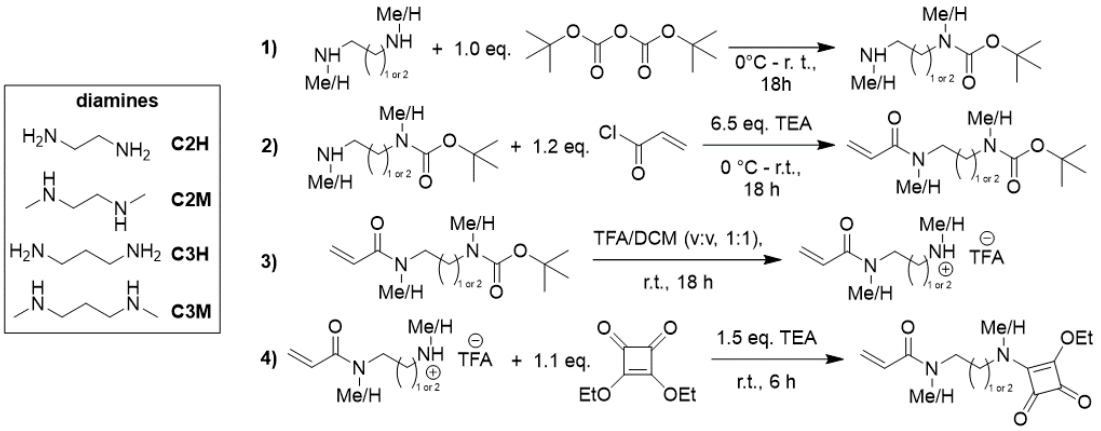

Scheme 4.1 General synthesis scheme of the SAA acrylate monomers in 4 steps starting from selected diamines (1,2-diaminoethane C2H, *N,N'*-dimethylethylenediamine C2M, 1,3-diaminopropane C3H and *N,N'*-dimethylpropylenediamine C3M).

could be explained by the inductive effect of the methyl group, which was enhancing the nucleophilicity of the amines. Since the heightened nucleophilicity could facilitate a double protection of the diamines, the equivalents of diamines were adjusted to three. The successful mono-substitutions were confirmed by ^{1}H-NMR (see appendix and Fig. 4.8).

The second synthesis step is the acroylation of the monoprotected diamines with acryloyl chloride (see Scheme 4.1 step **2)**). This functionalization worked well for all diamines, with yields up to 93 %. Before the squaric ethyl ester could be attached, the protected

Table 4.1 Single and overall yields of the synthesis steps for the SAA monomers. For M-C2M, no monomer could be isolated after the 4th synthesis step so an overall yield could not be calculated.

yield / % / monomer	step 1	step 2	step 3	step 4	overall
M-C2H	27	87	50	quant.	11.7
M-C2M	70	92	quant.	n. a.	-
M-C3H	21	93	quant.	98	19.1
M-C3M	49	72	quant.	quant.	10.6

amine group had to be deprotected in the third synthesis step. Boc protection groups can generally be removed by acidic treatment but since a free amine group could attack

the newly synthesized acrylamide group in an intramolecular aza-Michael reaction, trifluoroacetic acid (TFA) was used to form the stable TFA ammonium salt *in situ*. The deprotection worked well with quantitative yields for C2M, C3H and C3M, for C2H a yield of 50 % was achieved. Again, the conversion was confirmed by NMR (^{1}H and FTIR. Finally, in the last step, SAE was attached to obtain the squaric acid acrylamide

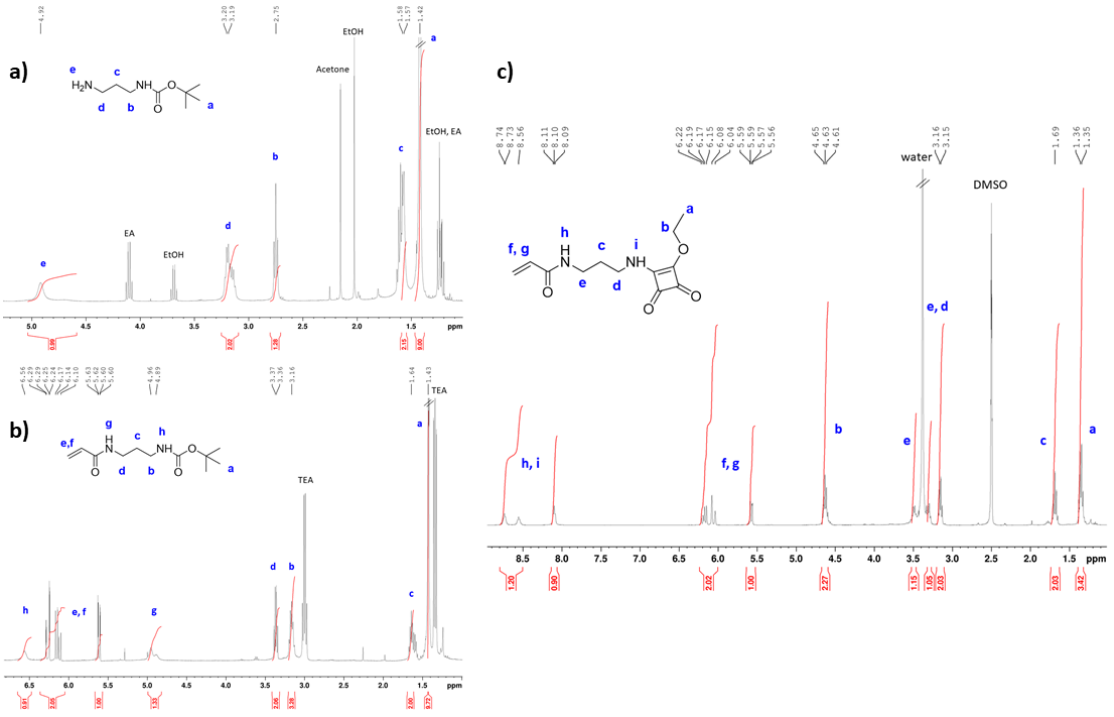

Fig. 4.8 Proton-NMR spectra of the isolated M-C3H intermediates after the reaction steps. a) Mono-Boc-protected C3H in $CDCl_3$. The singulett a at 1.42 ppm showed the successful N-boc protection of the first step clearly. b) Boc-protected C3H-acrylamide in $CDCl_3$. New signals between 5.50 and 6.40 ppm clearly showed the successful introduction of acrylamide of the second synthesis step. The broad signals h (6.56 ppm) and g (4.89 - 5.00 ppm) indicated the free amine protons on C3H. c) M-C3H in DMSO. The successful implementation of the squaric acid amide moiety into the acrylamide monomer could be demonstrated clearly through the new ethoxy signals at 4.63 ppm and 1.36 ppm (signals b and a).

monomers. After the substitution was completed, the crude products were purified by column chromatography over silica in ethylacetate. Unfortunately, during the purification of C2M, precipitation of the crude product on the column was observed. The isolated precipitate was analysed and identified as polymer formed through autopolymerization of the C2M monomer (see Fig. A.18). It was unclear why this monomer polymerized

spontaneously, since none of the other three monomers showed this behavior. The structures of the synthesized intermediate products were verified by proton NMR (compare to Fig. 4.8 and appendix). For clarification, the ^{1}H-NMR spectra of the different intermediates of M-C3H are depicted in Fig. 4.8 and their signals and integrals assigned accordingly. After the last synthesis step, the successful implementation of the SAA ester into the monomers was shown by the appearance of the ethoxy group signals a and b but needed to be further verified with an additional analysis method due to the lack of hydrogen atoms on the cyclobutenone unit. FTIR was selected as a suitable technique to analyze the carbonyl groups in the SAA moiety. As depicted in Fig. 4.9, the three acrylamide monomers M-C2H, M-C3H and M-C3M all displayed two weak carbonyl signals at around 1800 cm^{-1} and 1730 cm^{-1} (marked with black arrows) additionally to the carbonyl signal of the acrylamide moiety around 1675 cm^{-1} (purple arrow).

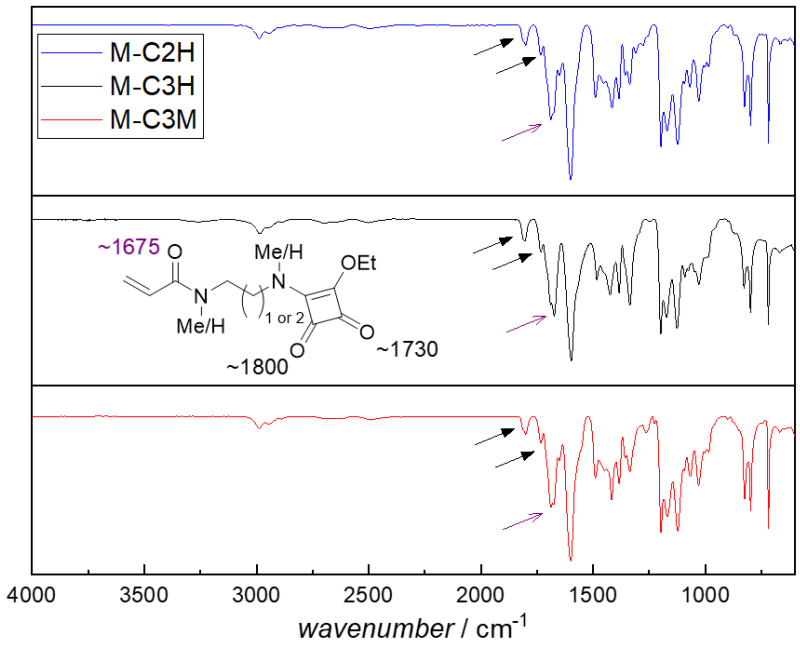

Fig. 4.9 IR spectra of the SAA acrylamide monomers M-C2H (blue), M-C3H (black) and M-C3M (red). The SAA carbonyl signals were marked with black arrows while the acrylamide C=O stretching signal was marked in purple.

After successfully obtaining the monomers M-C2H, M-C3H and M-C3M, it was attempted to polymerize them *via* reversible addition-fragmentation chain-transfer (RAFT) polymerization with 4-cyano-4-((((dodecylthio)carbonothioyl)thio)pentanoic acid as the

RAFT agent and *via* free radical polymerization. Unfortunately, the first RAFT polymerization attempt with M-C2H failed, therefore, the other monomers were subjected to free radical polymerization conditions. Due to the overall low yield of the monomer syntheses, the amount of monomers was very low (up to 200 mg). Because of this, some monomers could only be tested in one polymerization condition and the concentrations of the polymerization solutions were typically between 0.6 and 1.0 $\mathrm{mmol\,mL^{-1}}$. Unfortunately, the polymerizations didn't show any conversion of the monomers even after using different solvents (DMF, DMSO, THF) and different initiators (2,2-azobis(2-methylpropionitril) (AIBN) and 2,2'-azobis(4-methoxy-2,4-dimethylvaleronitrile) (V-70), refer to Table 4.2). This result was very unexpected, especially after M-C2M spontaneously polymerized after purification and it was not clear why the radical polymerizations of the SAA monomers wouldn't proceed in any of the tested conditions.

Table 4.2 Conditions of the polymerization attempts of the SAA acrylamide monomers. The polymerization solutions were set to a concentration between 0.6 to 1 $\mathrm{mmol\,mL^{-1}}$. None of the conditions resulted in polymerization. a) RAFT polymerization with 4-Cyano-4-(dodecylsulfanylthiocarbonyl)-sulfanylpentanoic acid (0.0135 mmol, 0.02 eq.) as chain-transfer agent (CTA).

monomer	solvent	initiator	temperature / °C	time / h
M-C2H [a]	DMF	AIBN	70	37
M-C3H	DMF	V-70	30	4
M-C3M	DMF	AIBN	70	4
M-C3M	DMSO	AIBN	70	4
M-C3M	THF	V-70	30	4

To see if the acrylamide monomers could be copolymerized, the SAA acrylate A was synthesized in two steps (see Fig. 4.10). SAE was first mono-substituted with *N*-methylaminoethanol. Since the resulting amide was not capable of undergoing an intramolecular substitution on the other side of the squaric acid ester, there were no additional protection steps necessary to obtain a stable intermediate product. Therefore, the overall effort to obtain the acrylate A was much lower than for the SAA acrylamide monomers. A was then attempted to copolymerize with M-C3H in a 1:4 monomer ratio (0.02 eq. AIBN as initiator, dry DMF as solvent, 70 $^{\circ}\mathrm{C}$ initiation temperature).
Unfortunately, the SEC results (50 $^{\circ}\mathrm{C}$ in dimethylacetamide (DMAc)) showed that not

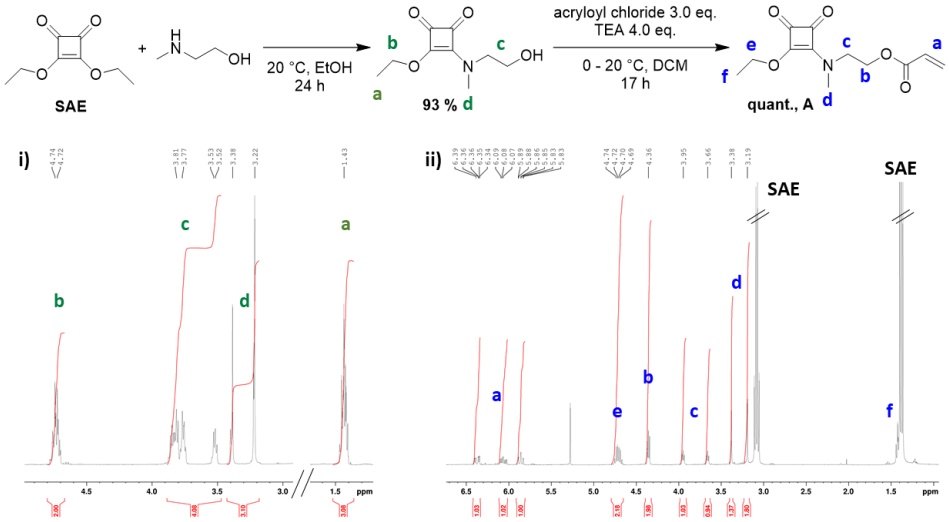

Fig. 4.10 Synthesis of the SAA acrylate monomer A from squaric acid ethyl ester (SAE) and *N*-methylaminoethanol in two steps and NMR characterization of both products. i) ^{1}H-NMR spectrum of the SAE ethanolamide in $CDCl_3$. All signals were assigned to the proposed structure (dark green letters). ii) ^{1}H-NMR spectrum of the SAA acrylate A in $CDCl_3$. All signals were distinctly assigned to the proposed structure (blue letters).

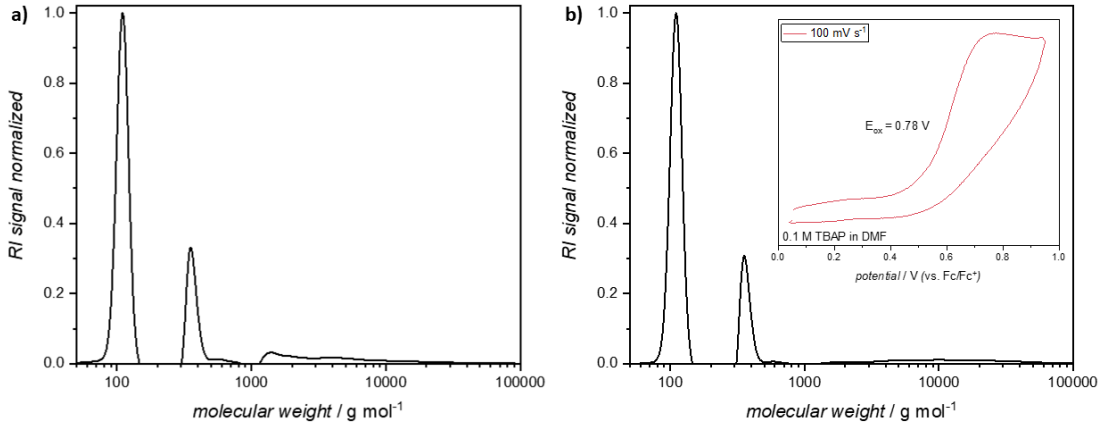

Fig. 4.11 SEC results of the co- and homopolymerization of SAA acrylate A. a) SEC trace of the copolymerization of monomer A with monomer M-C3H (ratio 1:4). The majority of the monomers remained unreacted and partial formation of oligomers and some polymer was obtained. b) SEC trace after homopolymerization of monomer A. The cyclic voltammetry of the product (scan rate 100 $\mathrm{mV\,s^{-1}}$, 0.1 M tetrabutylammonium perchlorate (TBAP) in DMF) showed a irreversible oxidation at 0.78 V vs. Fc/Fc^{+}.

all monomers were converted. Two signals around 100 and 400 indicated unreacted monomers and formed oligomers (see Fig. 4.11, a). A low intensity signal starting from 1100 $\mathrm{g\,mol^{-1}}$ showed the formation of polymer but with a very high dispersity (around Đ = 2.7) and low control. This result was not satisfying since the polymerization was not favored and the produced polymer was not clearly defined. Therefore, it was attempted to homopolymerize A in the same polymerization conditions but the SEC again showed that a lot of monomer was left unreacted and only partly formed oligomers (Fig. 4.11, b). A very small signal indicated some formation of polymer with a broad dispersity Đ = 1.9 but again, the polymerization wasn't favored and no clearly defined polymer was obtained. Nevertheless, it was attempted to measure cyclic voltammetry (CV) of the obtained product to see if the redoxactivity of the SAA functional group was still maintained. As seen in Fig. 4.11 b, an irreversible oxidation at 0.78 V vs. Fc/Fc^{+} was recorded. This result suggested that the SAA moieties in the product likely underwent side reactions after oxidation to form a species that couldn't be electrochemically reduced back to SAA. All of the obtained results discussed in the preceded paragraphs did not show a promising redox-active material. Firstly, the synthesis of the SAA monomers was very time-consuming. Due to the required 4 synthesis steps, the overall yield of the monomers was low (up to 19%). On top of this, the monomer M-C2M couldn't be obtained at all because of spontaneous polymerization during the purification. Despite this high reactivity of M-C2M, the synthesized SAA monomers couldn't be homo- or copolymerized at varied conditions *via* RAFT or free radical polymerization. One feature these monomers all had in common was that the SA moieties were asymmetrically substituted (one side ester and one side amide). To see if the low polymerization tendency of these monomers was connected to the nature of the SAA group, a new acrylate monomer with two amide functionalized SA sides was synthesized by M. E. Baumert at TU Dortmund. Additionally, a styrene based monomer was also provided. The results of the polymerization of these two monomers are summarized in the following section 4.2.2.

4.2.2 SAA Functionalized Polymers

As shown in the previous section 4.2.1, the synthesized asymmetric SAA acrylamide and acrylate monomers couldn't be polymerized with good conversion and control.

Therefore, a symmetric SAA acrylate monomer and a styrene-based monomer were synthesized by M. E. Baumert at TU Dortmund. The structures of both monomers were confirmed by ^{1}H-NMR (Fig. 4.12). These two monomers were then polymerized *via* free radical polymerization and RAFT polymerization, respectively (refer to Fig. 4.12). The SEC (50 °C DMAc) results showed that the polymerization of the acrylate monomer resulted in a polymer with higher molecular weights but at lower conversion in comparison to the RAFT polymerization of the styrene monomer (10 kDa vs. 3 kDa). The obtained

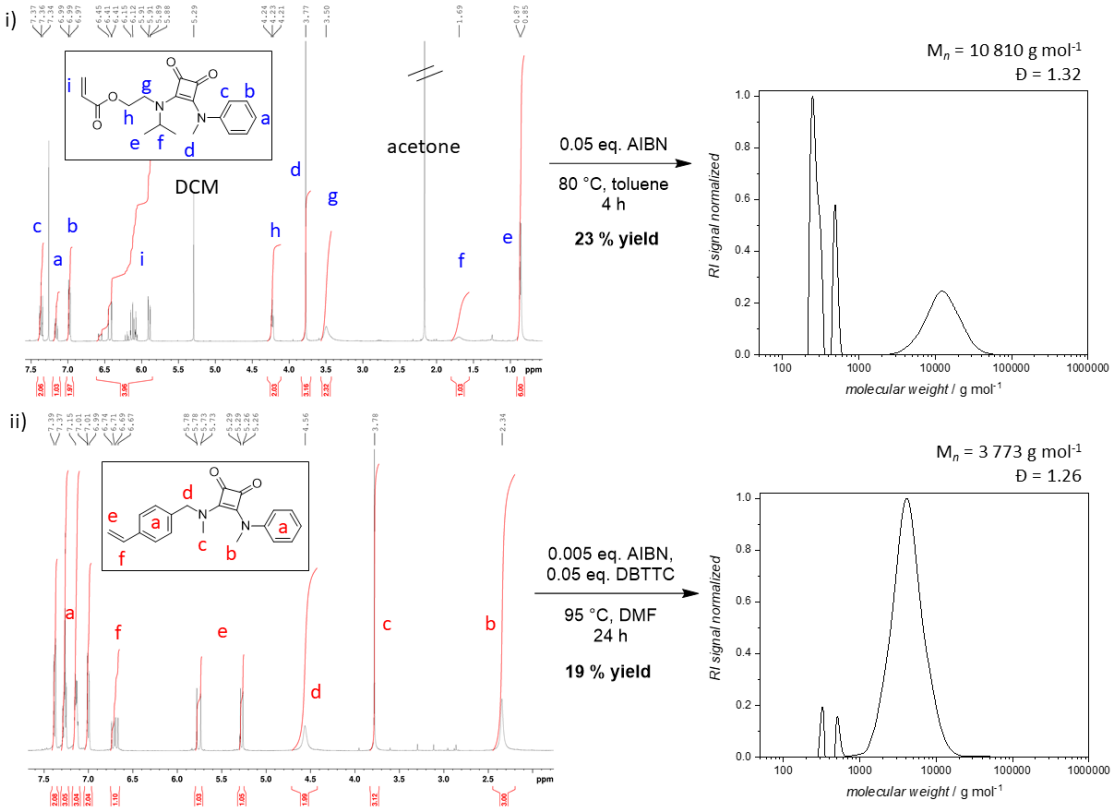

Fig. 4.12 Structure and polymerization of SAA bisamide monomers to obtain SA1 and SA2. The monomers were synthesized by M. E. Baumert at TU Dortmund and their structures verified by ^{1}H-NMR in $CDCl_3$ (left side). After subjecting the monomers to polymerization conditions (middle, i: free radical polymerization, ii: RAFT polymerization with dibenzyltrithiocarbonate (DBTTC) as chain transfer agent), SECs were measured in DMAc at 50 °C (right side).

polymers, SA1 and SA2 were analyzed with ^{1}H-NMR and FTIR (Fig. 4.13).

The polyacrylate SA1 was obtained *via* free radical polymerization as a light yellow solid (0.05 eq. AIBN, dry toluene, 80 °C, 23 % yield). Its high thermal stability was

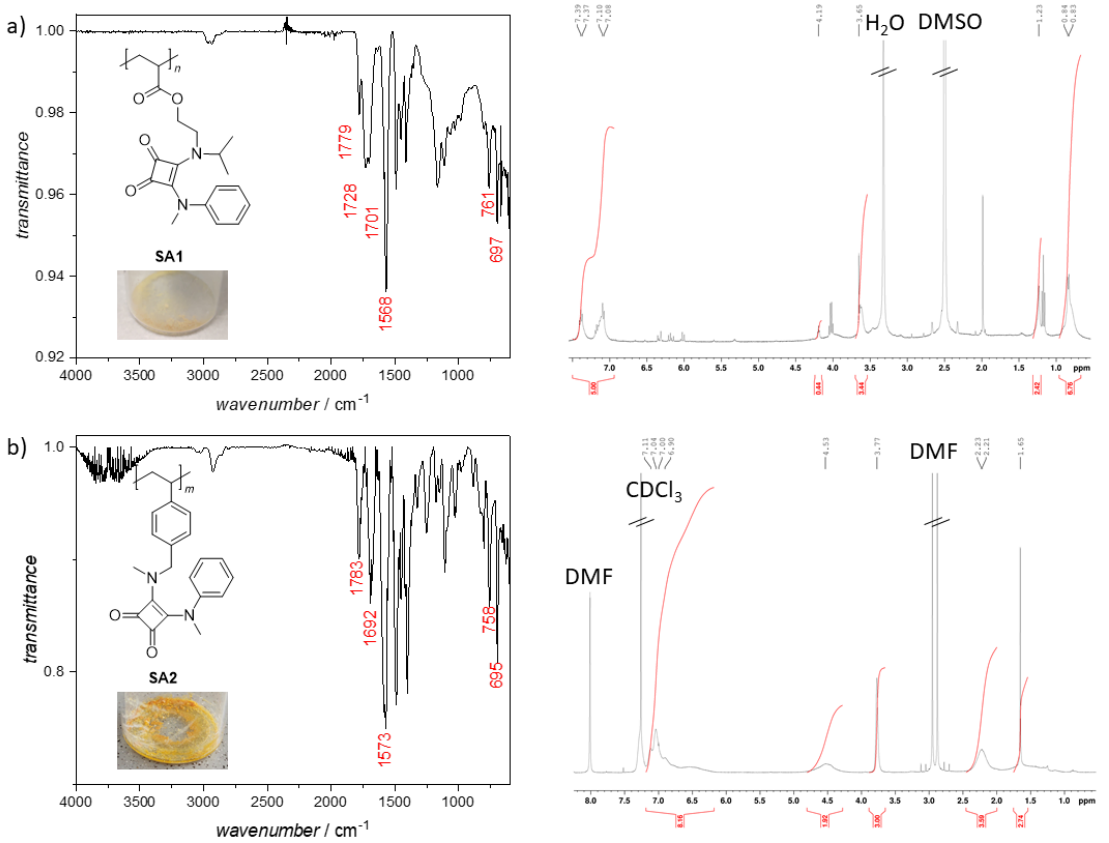

Fig. 4.13 Characterization of the SAA polymers SA1 (a, top) and SA2 (b, bottom). (a) The FTIR spectrum of SA1 showed the carbonyl signals of the cyclobutenone moiety (1779 and 1701 cm^{-1}) next to the acrylat carbonyl (1728 cm^{-1}). In the proton NMR spectrum (in deuterated DMSO), some monomer signals were still visible in the olefinic region (between 6.0 - 6.5 ppm). b) The FTIR spectrum of SA2 also showed the two SAA carbonyl signals clearly (1783 and 1692 cm^{-1}).

revealed by thermogravimetric analysis (TGA). From the TGA curve, the decomposition temperature T_d(5%), where 5 wt % of the material was degraded, was determined to be 180 °C. Interestingly, in differential scanning calorimetry (DSC) SA1 showed a melting point at 82 °C instead of a glass transition. This could be a result of the monomers still left in the product as seen in NMR (signals between 6.0 and 6.5 ppm).

The polystyrene SA2 was obtained *via* reversible addition-fragmentation chain-transfer (RAFT) polymerization with S,S-dibenzyl trithiocarbonate (DBTTC) as the chain transfer agent. As seen in SEC, the yield and molecular weight of the resulting product was lower than SA1, but the conversion was higher and in NMR (Fig. 4.13) no residual monomer signals could be detected. Additionally, the thermal stability of SA2 was also

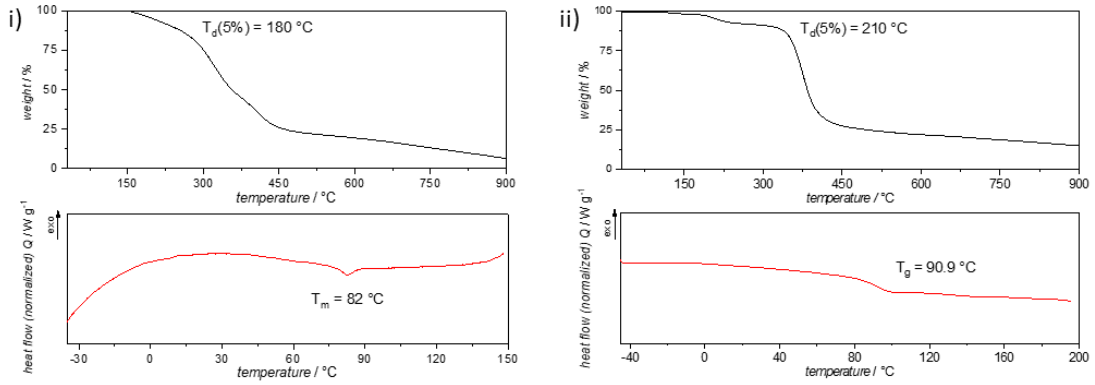

Fig. 4.14 Thermal characterization of the SAA polymers SA1 (i, left) and SA2 (ii, right) *via* TGA and DSC. (i) The TGA curve of SA1 in nitrogen atmosphere showed a decomposition temperature of 180 °C. Until 900 °C there was still residual mass left which means that a part of SA1 was not decomposing at temperatures up to 900 °C in a non-oxidative atmosphere (N_2). The second heating curve of the DSC of SA1 surprisingly showed a weak melting point instead of a glass transition. This could be a result of some monomer left in the product, as seen by signals in the olefinic region of the NMR spectrum. ii) SA2 showed a slightly higher thermal stability with a decomposition temperature at 210 °C according to TGA. Similar to SA1, at the maximum temperature of 900 °C residual mass could still be detected. In DSC, SA2 showed a glass transition around 91 °C as expected for polystyrene-based polymers.[139]

slightly higher than SA1 (T_d = 210 °C) and the glass transition temperature T_g was also in the range expected for polystyrene-based polymers (91 °C refer to Fig. 4.14).[139]
After characterization of SA1 and SA2, both polymers were tested in regard to their electrochemical properties (Fig. 4.15). To examine the redox properties of SA1, cyclic voltammetry (CV) was measured in DMF and DCM (refer to Fig. 4.15, i and ii). It was observed that the polymer showed an oxidation at 0.72 V vs. Fc/Fc^+ in either solvent. However, during the reverse sweep no reduction peak could be observed, indicating that the oxidation was not reversible. On top of this, a formation of solid precipitate in the CV cell could be observed after the first oxidation sweep. This observation was in accordance with a noticable decrease of the current after each recorded cycle. The irreversibility of the oxidation of SA1 seemed to be independent from the solvent, since it was detected in both solvents DCM and DMF. It should be noted, that the shape of the CVs did slightly change, but the oxidation potential remained the same.
In the case of the polystyrene SA2, the CV in DCM showed a redox process at a slightly lower potential of $E_{1/2}$ = 0.62 V vs. Fc/Fc^+ (see **??**, (iii)). The shifting of the peak potentials with higher scan rates indicated a slow electron transfer, concluding that the

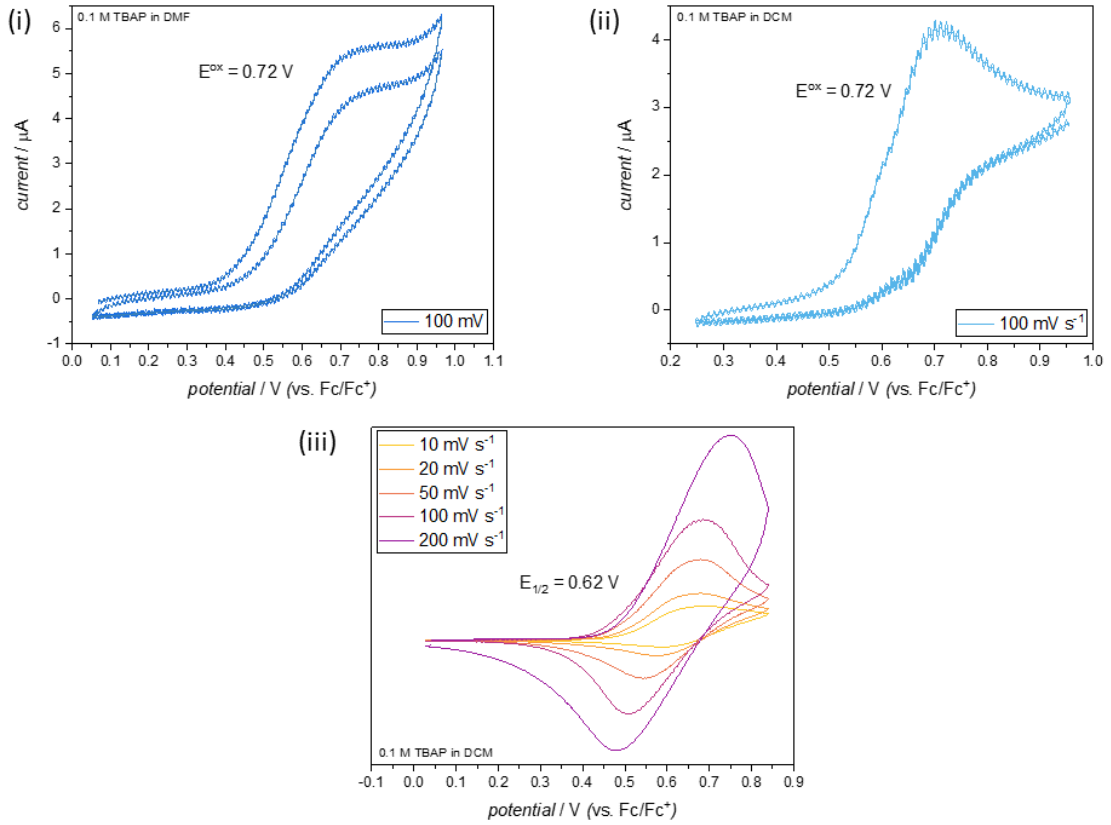

Fig. 4.15 Electrochemical properties of the SAA polymers SA1 and SA2 according to CV. (i) The CVs of SA1 in 0.1 M TBAP in DMF recorded with a scan rate of 100 $\mathrm{mV\,s^{-1}}$. As the form of the CV curve showed, the oxidation at 0.72 V vs. Fc/Fc^+ was not reversible and the already low current decreased further in the second cycle. (ii) CV of SA1 in 0.1 M TBAP in DCM, also displaying an irreversible oxidation at the same potential 0.72 V vs. Fc/Fc^+. (iii) CV of SA2 in 0.1 M TBAP in DCM at different scan rates. A reversible redox reaction at 0.62 V was recorded. Ferrocene was used as an internal reference for all CV measurements.

observed redox reaction was not fully reversible in the given conditions. Since the parameters for testing towards battery application would be different, these CV results nevertheless indicate that SA2 could be a potentially interesting redox-active material. In addition to this, the thermal properties of SA2 indicated a high stability towards thermal treatments (T_d(5%) = 210 °C) which would be beneficial for potential electrode preparation. SA2s high glass transition temperature at around 90 °C was also in accordance with values expected for polystyrene based polymers.

To get an idea for the performance of SA2 as a organic cathode material for battery applications, an electrode was prepared from a mixture from SA2 as active material,

conductive carbon and a binder material, to be tested in a half-cell setup. Li metal was used as the anode and the electrolyte was prepared as 1 M $LiPF_6$ in an ethylene carbonate (EC) and dimethyl carbonate (DMC) mixture of 5:5 weight-% solution. The half-cell setup and measured CV are displayed in Fig. 4.16.

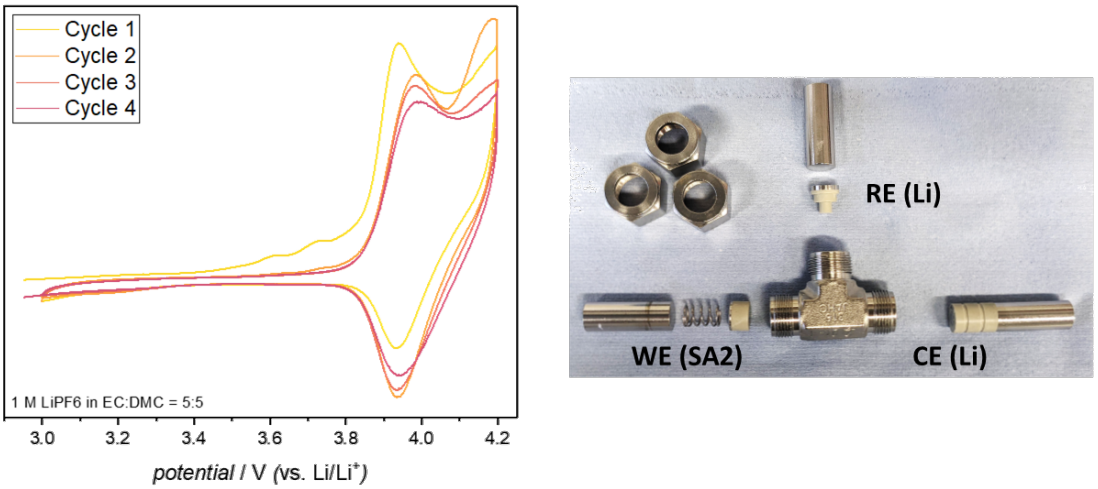

Fig. 4.16 CV of SA2 in a Li half-cell. The reference and counter electrodes (RE and CE, respectively) are lithium metal. As an electrolyte solution, LP-30 (1 M $LiPF_6$ in ethylene carbonate (EC) and dimethyl carbonate (DMC) (5:5 weight percent (wt %))) was prepared. The CV was recorded with a scan rate of 100 $\mathrm{mV\,s^{-1}}$ over 4 cycles. It could be observed that the redox potential was shifting from 3.93 Vin the first cycle to 3.96 Vvs. Li/Li^+ by the fourth cycle. Additionally, the specific current was also slightly decreasing with each cycle. On the right side, the swagelock T-cell used for the half-cell three electrode setup is depicted.

As seen in the CV measurement, SA2 showed a reversible redox peak at 3.93 Vthat was shifting to 3.96 Vvs. Li/Li^+ by the fourth CV cycle. Further, in the first cycle two small oxidation peaks could be observed at around 3.60 Vand 3.72 V. Both oxidation peaks disappeared in the following CV cycles. It can be speculated that, similar to the behaviour of DDD (see Fig. 4.4), the first oxidation of SA2 was an activation step causing a similar homogenation of the electrode. However, this effect didn't seem to be considerable, since the observed shift was rather small and a significant change in the shape of the redox peak could also not be observed. Additionally, a second oxidation was noted at around 4.2 VThis oxidation seemed irreversible and indicated a possible side reaction of SA2 in LP-30. These results, combined with a noticable decrease in the specific currents after

each cycle, indicate a dissolution of SA2 from the electrode into the electrolyte LP-30. A dissolution of electrode material in the electrolyte is an undesirable side reaction that causes poor cyclability and high capacity loss in batteries. Therefore it can be concluded that a different electrolyte composition should be used to test SA2 as a cathode material in batteries.

Overall, the results from SA2 support the assumption that SAA-containing polymers could potentially represent a promising new class of redox-active organic materials (ROMs). It was shown that the two synthesized SAA polymers showed high glass transition temperatures above 80 °C and high thermal stability with decomposition temperatures above 180 °C. In regard to the redoxactivity, SA2 displayed a reversible oxidation at high potentials (0.62 V vs. Fc/Fc^+) in DCM according to CV. The redox property of SA2 seemed to be maintained after electrode preparation and testing in the common electrolyte LP-30. Unfortunately, the CV results indicated dissolution of SA2 in the tested electrolyte, therefore the galvanostatic cycling of SA2 should be tested with a different electrolyte composition. In optimized conditions, the SAA polymers could possibly be used for energy storage or other important redox applications. Especially in the field of organic batteries, the selection of ROMs is limited, therefore every contribution towards the expansion of this area of research is essential to make progress.

4.2.3 Polycondensation to SAA Main Chain Polymers

It was demonstrated in 4.2.2 that the SAA containing homopolymer SA2 showed interesting electrochemical properties that could render it suitable for energy storage applications. Despite the promising material properties, one major drawback was the rather exhaustive synthetic effort required to obtain this polymer. Additionally, SA2 has a rather high amount of molecular weight that is not contributing to the redox activity of the polymer and therefore lowering its theoretical capacity. These two factors could severly limit the applicability of SA2. A way to overcome these issues is the synthesis of main chain polymers by straightforward polycondensation of different diamine linkers with squaric ethyl ester (SAE) to obtain SAA main chain polymers in a single step (see Scheme 4.2). The linkers used for the polycondensations were *N,N*'-dimethylethylenediamine, *N,N*'-dimethylpropylenediamine and homopiperazine. Unfortunately, the polycondensations

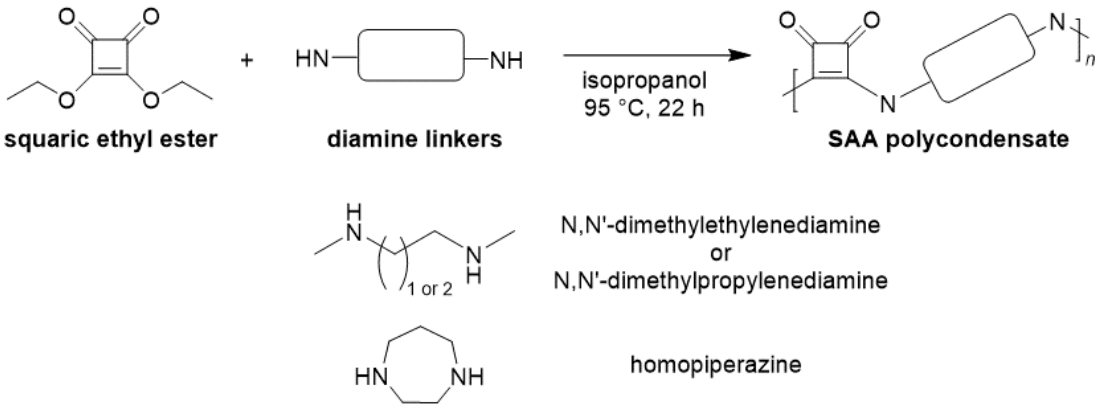

Scheme 4.2 General scheme for the synthesis of SAA polycondensates in one step. The diamines used as linkers were *N,N*'-dimethylethylenediamine, *N,N*'-dimethylpropylenediamine and homopiperazine.

didn't result in high yields or formation polymers. For the condensation with *N,N*'-dimethylethylenediamine, the resulting product was a powder with very low solubility in a range of solvents. Therefore it was not possible to record NMR in deuterated chloroform, DMSO or toluene as well as SEC in DMAc or THF. The recorded FTIR spectrum was not feasable to determine the formation of polymer due to the lack of a suitable distinct signal (Fig. 4.17). All three of the IR spectra looked similar. They consistently showed the two distinct carbonyl signals of the cyclobutenone moiety of SAA (1791 and 1669 cm^{-1} for the condensation product of SAE and ethylenediamine, Fig. 4.17 left, 1791 and 1700 cm^{-1} for the condensation product of SAE and propylenediamine, Fig. 4.17 middle, and lastly, 1780 and 1671 cm^{-1} for the condensation product with homopiperazine Fig. 4.17 right) and the C=C stretching signal of the cyclobutene moiety between 1540 and 1570 cm^{-1} (most intensive signal in all three FTIR spectra). Therefore, from the IR analysis only the existence of SAA moieties in the products could be clearly confirmed but not the actual condensation of the feeding monomers.

For the condensation with *N,N*'-dimethylpropylenediamine, the results were similar but the resulting product was slightly better soluble and NMR in deuterated DMSO and SEC in DMAc could be recorded. Unfortunately, the SEC result showed a prominent monomer signal, some oligomer formation and no actual polymer. This result was dissatisfying as no main chain polymer was formed. Due to the structure of the propylenediamine linker, it is possible that instead of polycondensation the intramolecular ring formation was favored and therefore no polymer was obtained. This theory would be reasonable since

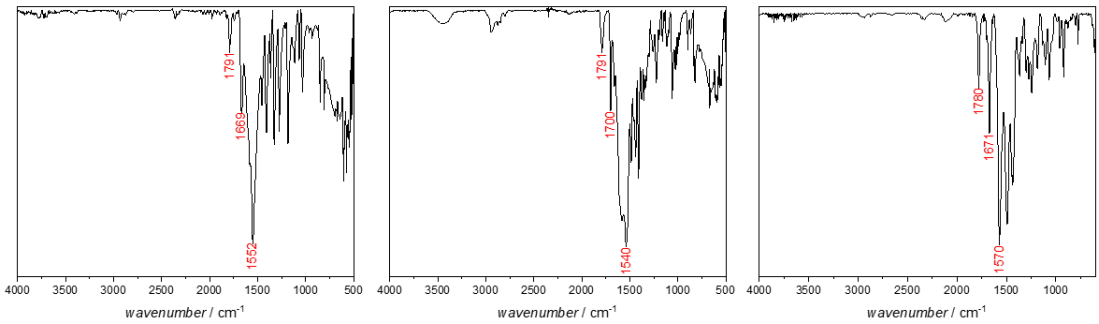

Fig. 4.17 FTIR spectra of the SAA condensation products with *N,N*'-dimethylethylenediamine, *N,N*'-dimethylpropylenediamine and homopiperazine (from left to right). All three spectra looked very similar and showed the identifying carbonyl signals and C=C stretch of the SAA group (marked in red). No signal was suitable to identify if polycondensation products were formed.

the synthesis of DDD (4.1) also proceeds *via* intramolecular ring formation. Therefore it could also be concluded that the diamine linker *N,N*'-dimethylethylenediamine most likely resulted in the formation of insoluble cyclic SAA molecules too instead of a SAA main chain polymer.

Since the structure of homopiperazine is bulky, it was hypothesized that this diamine should be a more suitable linker for the synthesis of SAA polycondensates. Unfortunately, the SEC showed the same result as for the condensation with the propylenediamine. This result suggested that the main chain polymer formation is most likely generally disfavored, independent from the nature of the used diamine linker. A possible explanation would be that the first substitution on the squaric ethyl ester is deactivating the second substitution so significantly that no polycondensation can occur. It is questionable if the polycondensation would be possible with other diamines due to this significant reactivity issue.

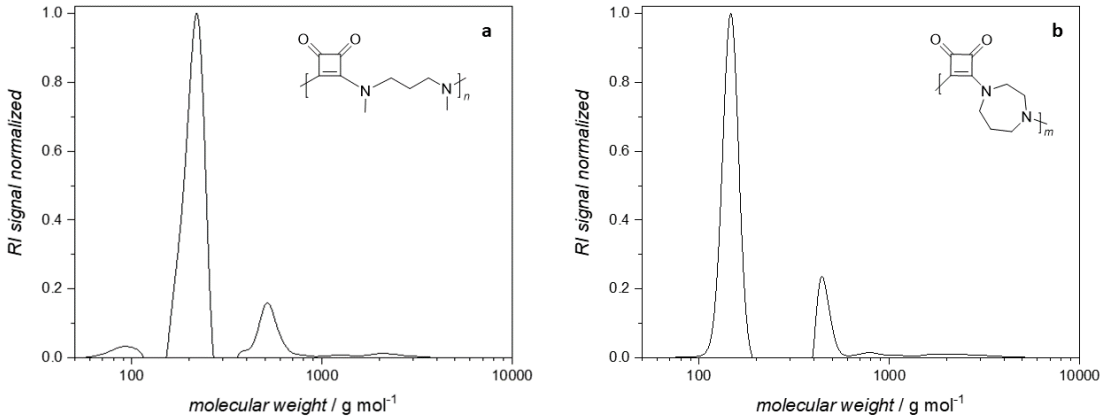

Fig. 4.18 SEC traces of the SAA condensation products. a) The condensation with *N,N'*-dimethylpropylenediamine showed almost no conversion and just a small amount of formed condensation product. b) Homopiperazine as the diamine linker also didn't result in linear polymer chain formation. The SECs were recorded in DMAc at 50 °C and calibrated with polystyrene standards.

5 Squaric Acid Quinoxalines (SQXs)

5.1 SQX Small molecules

The results in the previous chapter (4) suggested that the stability of squaric acid amides (SAAs) could be enhanced by bridging the amides as in 2,5-diphenyl-2,5-diazabicyclo[4.2.0]oct-1(6)-ene-7,8-dione (DDD). A functional group that matches this structural requirement is the group of squaric acid quinoxalines (SQXs).

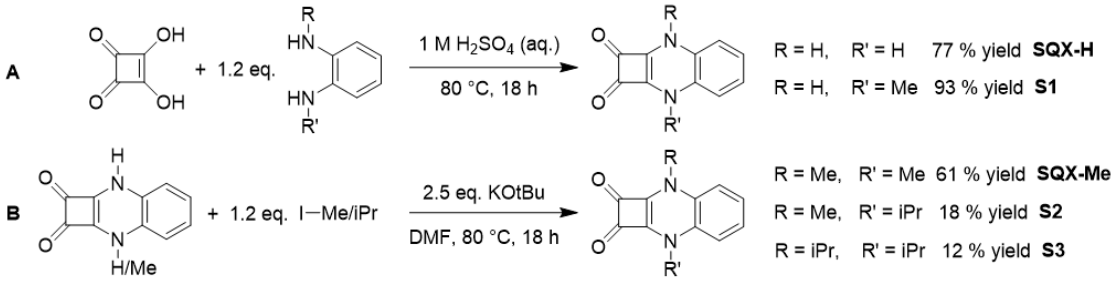

Scheme 5.1 Synthesis schemes for the SQX molecules. A = condensation of squaric acid with *o*-phenylenediamine or *N*-methyl-*o*-phenylenediamine to obtain SQX-H and S1. B = Substitution of SQX-H or S1 with methyl- or isopropyliodide to obtain SQX-Me, S2 and S3.

The general synthesis routes for SQX molecules are depicted in Scheme 5.1. To obtain the main SQX unit, SQX-H, squaric acid was condensed with *o*-phenylenediamine. Exchanging the diamine to *N*-methyl-*o*-phenylenediamine resulted in the synthesis of S1. In general, by alkylating one or both of the amine groups at the phenylenediamine, asymmetric SQX molecules could be obtained. Both molecules, SQX-H and S1 were obtained in good yields. For the synthesis of SQX-Me and S2, the molecule S1 was used as the starting material, activated with KO^{t}Bu and reacted with methyliodide and isopropyliodide, respectively. While SQX-Me was still obtained with good yields (61 %), the yield for S2 was significantly decreased. An explanation for the reduced yields could

be the lowered reactivity of isopropyliodide in comparison to methyliodide, which is known as a potent methylating agent.[140] This reason was further affirmed as the two-fold substitution of SQX-H with isopropyliodide gave S3 in even lower yields (12 %). It was generally observed that the condensation route A resulted in higher yields and therefore should be the preferred synthesis route to obtain SQX molecules.

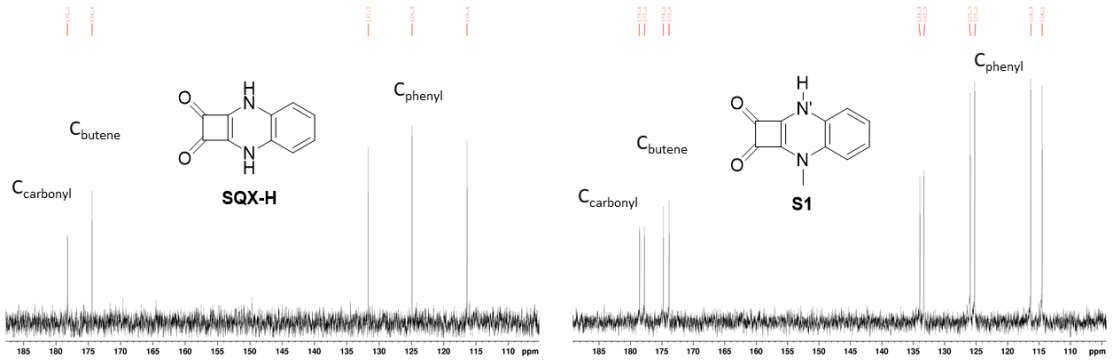

Fig. 5.1 Comparison of the ^{13}C-NMR spectra of SQX-H and S1 (100 MHz in deuterated DMSO). The SQX-unit identifying signals were assigned as follows: carbonyl C = 178 ppm, butene C = 174 ppm, phenyl Cs = 131, 125, 116 ppm. For asymmetrically substituted SQX molecules, the signals are doubled as shown in the spectrum of S1.

The successful synthesis of the SQX molecules was verified *via* NMR spectroscopy. Since the SQX unit only contained covalently linked protons on the phenyl-side, ^{13}C NMR spectra were integral to identify the cyclobutenone part. As shown in Fig. 5.1, the SQX unit displayed five distinctive carbon signals that could be assigned to the carbonyl-, alkenyl- and aromatic carbons. Interestingly, for asymmetrically substituted SQX molecules, the five carbon signals are doubled due to the slightly changed chemical environment as demonstrated on the example of S1 (Fig. 5.1, right).

Elaborating on the findings of Hünig and coworkers in 1977, the molecules SQX-H and SQX-Me were re-synthesized for thorough characterization.[28] Confirming their results, the rapid proton transfers of SQX-H in DMF during CV were also observed in the replicated measurements. To have a reliable, solvent independent point of reference, ferrocene was used as an internal reference for all CV measurements. The first irreversible electrochemical oxidation to SQX-ox (see Scheme 2.5) was detected at 0.12 V vs. Fc/Fc^+ and the reduction from SQX-sem back to SQX-H occurs at -0.38 V vs.

Fc/Fc^+(see Fig. 5.2). It could be verified that the electrochemical reactions were overall reversible by cycling over three CV cycles.

On top of the interesting electrochemical behavior, the high stability of SQX-H was also verified by thermogravimetric analysis (TGA) under nitrogen atmosphere. It was clearly visible that SQX-H withstands more than 300 °C until it cleanly decomposes in two steps (see Fig. 5.2). Additionally, in differential scanning calorimetry (DSC) no visible melting or crystallization could be observed between -50 to 300 °C, further solidifying the thermal stability SQX-H exhibits over this large temperature range (see appendix).

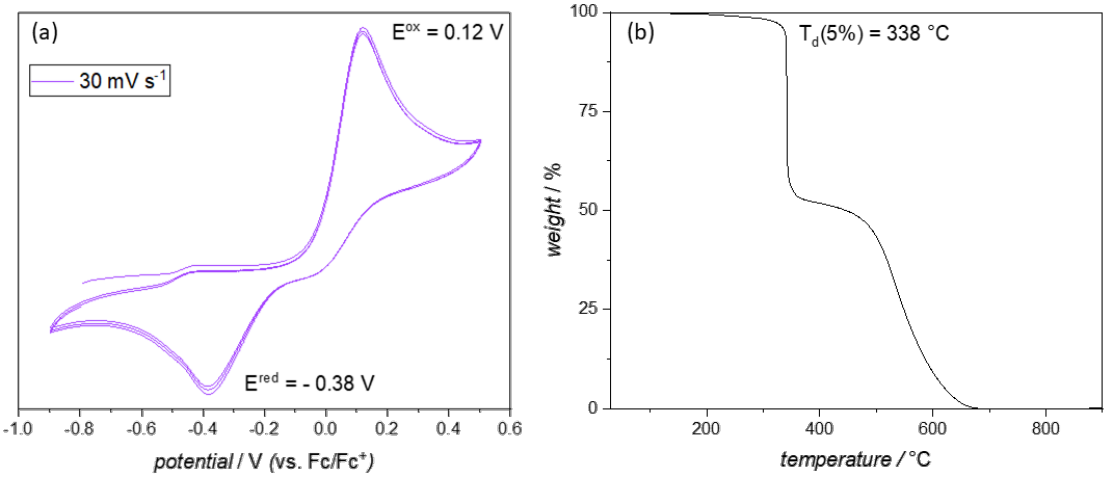

Fig. 5.2 Confirmation of SQX-Hs key characteristics. (a) CV of SQX-H in 0.1 M TBAP dry DMF over three cycles. Ferrocene was used as an internal reference. The shape and observed redox events are in agreement with the findings of Hünig in 1977.[28] (b) TGA shows the high thermal stability of SQX-H under nitrogen atmosphere. The first decomposition starts at ca. 340 °C with a weight loss of around 48 wt-%, followed by a second decomposition at around 400 °C.

Concerning the molecule SQX-Me (Scheme 2.5), the statements from Hünig could also be confirmed. The brightly colored orange solid showed a high thermal stability similar to SQX-H. During CV in DMF, a reversible oxidation with a redox potential of 0.30 V vs. Fc/Fc^+ was observed and SQX-Me didn't indicate any signs of irreversible oxidation processes (see Fig. 5.3). This was in agreement with the results of Hünig and coworkers[28].

In contrast to the proposed synthesis pathway (condensation of SA with *N,N'* -dimethyl-o-phenylenediamine), SQX-Me was synthesized by methylation of the single methylated

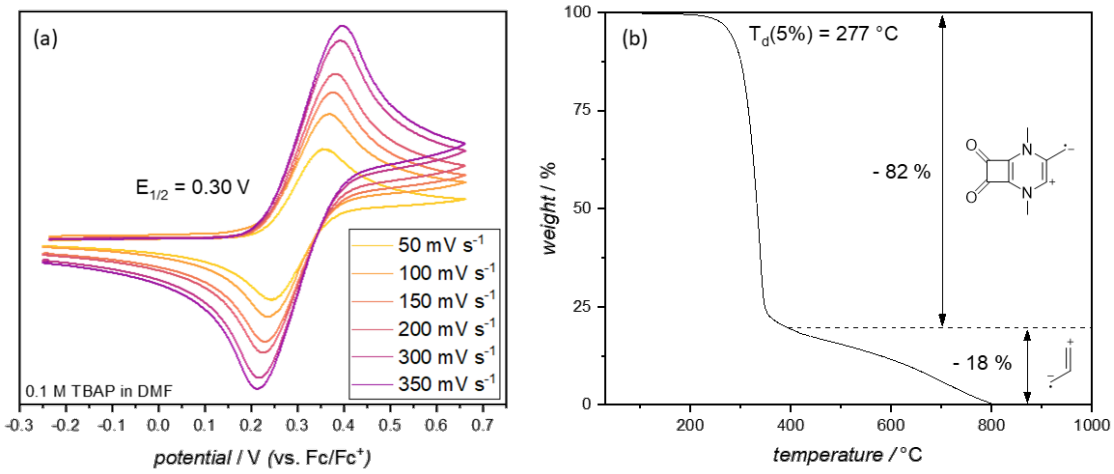

Fig. 5.3 Confirmation of SQX-Me's key characteristics. (a) CV of SQX-Me in dry DMF (0.1 M TBAP) at different scan rates. Ferrocene was used as an internal reference. The greatly improved redox potential and reversibility of the oxidation was in agreement with the results of Hünig[28]. (b) TGA shows the high thermal stability of SQX-Me under nitrogen atmosphere (T_d(5%) = 277 °C). Interestingly, SQX-Me decomposes asymmetrically in two steps, with 82 % weight loss in the first step (corresponding to the main diaza-cyclobutenedione structure) and the remaining 18 % fully decomposing until 800 °C was reached.

SQX molecule S1 under basic conditions (see experimental)[127].

It was safe to assume that the rapid proton transfer after the electrochemical oxidation of SQX-H was prevented by substitution of the amide protons on N and N' with alkyl groups. This hypothesis could be verified by examination of the electrochemical properties of the SQX molecule S1 (see Fig. 5.4).

In DMF, the CV of S1 shows an unusual behavior: depending on the scanned potential range, certain oxidation and reduction peaks would appear or disappear. For instance, the scan from -0.95 to 0.55 Vvs. Fc/Fc$^+$ (Fig. 5.4 potential range ΔE = 1.5 V, dashed line) shows an oxidation peak at 0.12 V before the second oxidation E_2^{ox} at 0.27 V. While E_2^{ox} can be seen in all three potential ranges, E_1^{ox} disappears for the scans that are going to low potentials (Fig. 5.4, (ii) dotdashed and solid lines), instead, a quasi-reversible reduction appears at $E_{1/2}$ = 0.65 V vs. Fc/Fc$^+$. In the potential range of 2.2 V from -1.65 to 0.55 V vs. Fc/Fc$^+$ a very low reduction peak can be determined at -1.43 V. The precise mechanism of these electrochemically induced oxidation and reduction reactions S1 undergoes can not be determined easily. However, it can be deduced from these results that DMF as a solvent was the decisive factor causing this unusual behavior. In parallel to the CV of SQX-H, the basicity of DMF could cause a deprotonation of S1

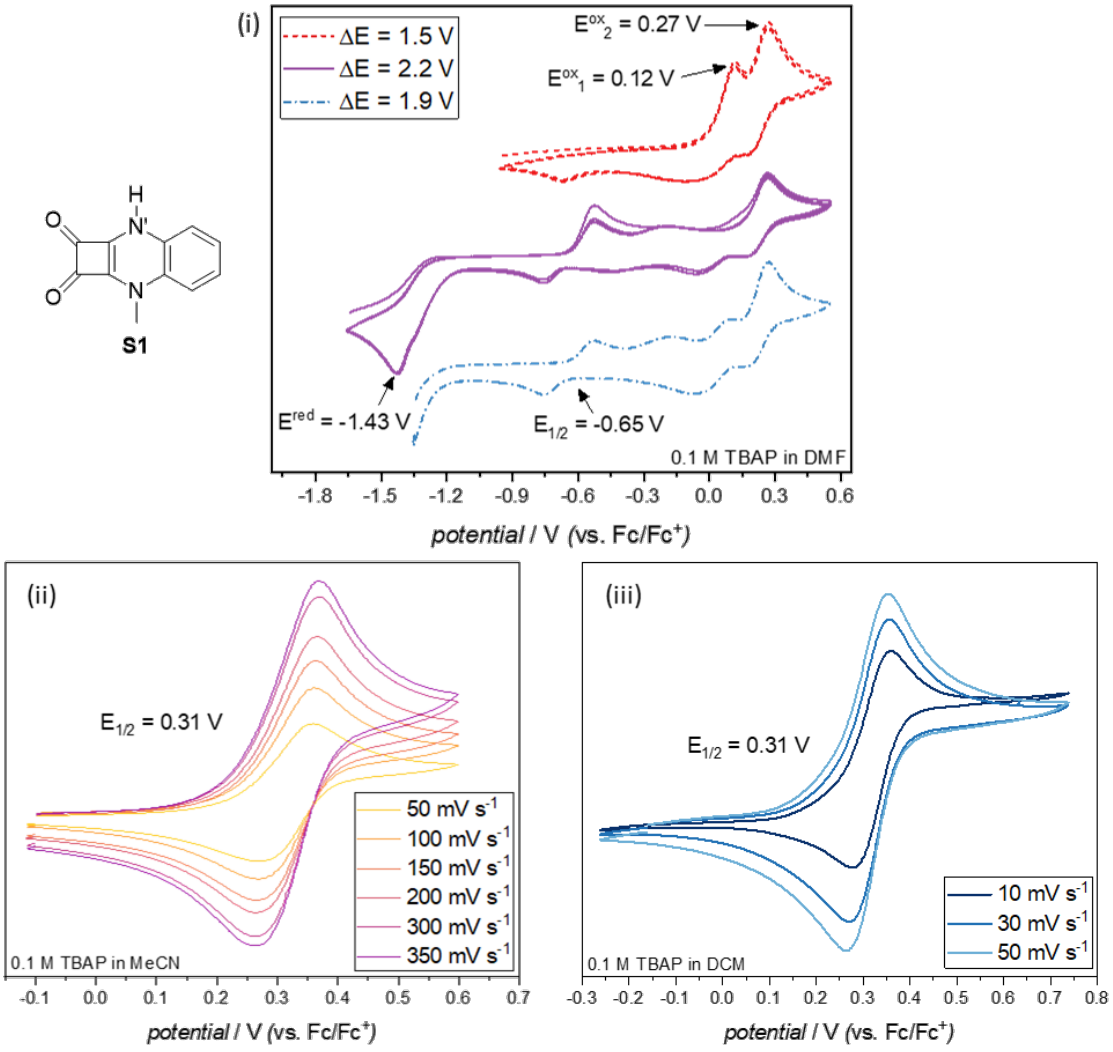

Fig. 5.4 Electrochemical behavior of the SQX molecule S1. (i) CV of S1 in 0.1 M TBAP dry DMF in different potential ranges (ΔE). The scans are depicted with an offset for easier comparison. All relevant redox peaks are marked with arrows. (ii) CV of S1 in 0.1 M TBAP dry acetonitrile (MeCN) at different scan rates. (iii) CV of S1 in 0.1 M TBAP dry dichloromethane (DCM) at different scan rates. Ferrocene was used as an internal reference for all depicted CVs.

after the first oxidation, followed by subsequent side reactions that are driven by the applied voltages. To prove this theory, CV measurements of S1 were carried out in less basic solvents like acetonitrile (MeCN) and dichloromethane (DCM)[141].
In both solvents, DCM and MeCN, S1 shows a reversible oxidation at 0.31 V vs. Fc/Fc^+ (see Fig. 5.4). This value was in line with the magnitude of the redox potential of SQX-Me (0.30 V, compare Fig. 5.3). The drastically different redox behavior of S1 in DMF compared to DCM and MeCN, further indicates that the solvent selection for electrochemical measurements can have a big impact on the performance of the material and confirms the findings of Hünig and coworkers. Therefore, to prevent the rapid proton transfer in DMF, any protons on the nitrogens N and N' of the SQX moiety, should be substituted with alkyl groups.
The examination of S1 with TGA shows a very high thermal stability with a decomposition temperature of 286 °C. In direct comparison with the TGA curve of SQX-H (see Fig. 5.2, (b)) both curves show two very distinctive decomposition steps, which suggests that the SQX molecules have the same decomposition mechanism. Due to the asymmetric structure of S1, the two step decomposition pathway can be estimated as follows: above 270 °C the cyclobutenone side of S1 was decomposing first, leaving the residue aromatic amino moiety to start degrading in a second step above 400 °C (complete degradation at around 650 °C). Analogue to the previously discussed SQX molecules, the DSC curves don't show any noticable peaks and implicate that S1 was stable in the temperature range from -30 to 290 °C (see Fig. 5.5).

To investigate what kind of effect the introduction of isopropyl substituents on the SQX systems have, two new SQX molecules, S2 (isopropyl group on N and methyl group on N') and S3 (isopropyl groups on both Ns) were synthesized and thoroughly characterized. One of the first property changes, that could be observed, was the improved solubility of S2 and S3 in comparison to SQX-H and S1. This improved solubility made it possible to purify both molecules *via* column chromatography and facilitates further chemical modifications. Both molecules were obtained as bright red (S2) and dark orange (S3) solids. The evaluation of their electrochemical properties *via* CV, showed a reversible redox reaction at 0.36 Vvs. Fc/Fc^+ for both molecules (see Fig. 5.6). This was remarkable, since it suggests that the introduction of the first isopropyl group already greatly dictates the redox potential of the SQX molecule, so that the second isopropyl group

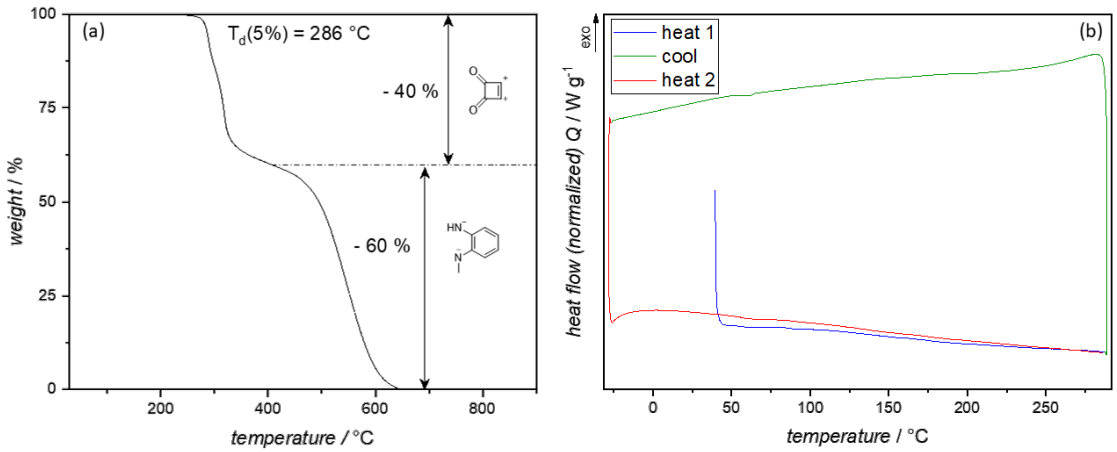

Fig. 5.5 Thermal properties of SQX molecule S1. (a) TGA of S1 in inert nitrogen atmosphere. The cyclobutendione moiety (corresponding to 40 % of S1's weight) was proposed to decompose in the first step before the aromatic amino moiety was degraded above 400 °C. (b) DSC curves of S1 with a heating (and cooling) rate of 10 °C min^{-1}. S1 appears to be stable in the scanned temperature range from -30 to 290 °C without any visible change of state.

does not enhance it further. From this aspect, it can be concluded that in the case of an asymmetrically substituted SQX molecule the redox potential was dictated by the substituent with the stronger inductive effect.

Besides the redox potential, the thermal properties are also heavily influenced by the isopropyl groups. For instance, the decomposition temperatures of S2 and S3 are lowered to 220 °C and 228 °C, respectively, and the DSC analysis shows noticable melting and recrystallization points (see Fig. 5.6). These results propose that the isopropyl group was lowering the crystallinity of the SQX molecules by disrupting their stacking order. This assumption was reasonable as it was known, that isopropyl groups have a strong steric effect and introduce repulsion into a molecule that can be estimated by the ligand repulsion energy E_R.[142] This E_R disrupts the crystallization of the molecules, which was also clearly visible in the DSC curves in Fig. 5.6. While S2 shows recrystallization during cooling (onset temperature = 97.9 °C), there was no indication in the corresponding cooling curve of S3. Instead, the melt of S3 shows a glass transition at 16 °C, followed by a crystallization (onset = 45 °C). This unusal crystallization behavior is called cold crystallization and appears at temperatures between glass transition and melting point. For polymers, cold crystallization was described by Wunderlich as an effect occuring after rapid quenching of a polymer from above its melting temperature to a randomly oriented glass[143]. Upon reheating, after passing T_g the rearrangement of

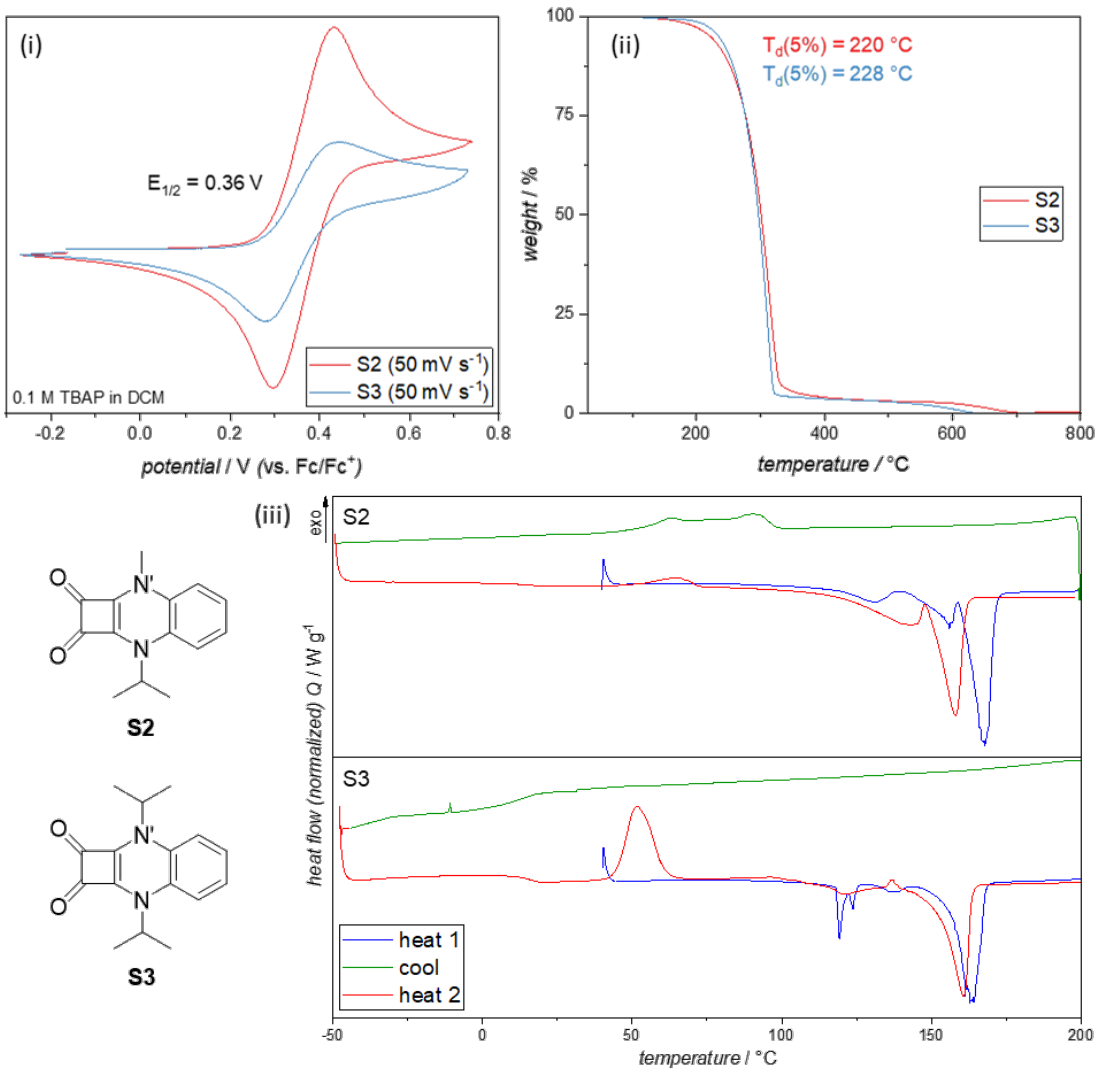

Fig. 5.6 Comparison of the SQX molecules S2 and S3 and the influence of isopropyl groups on their properties. (i) CVs of S2 and S3 in 0.1 M TBAP in DCM. The potential was referenced against ferrocene. (ii) TGA curves of S2 and S3 under nitrogen. The decomposition temperatures are drastically reduced in comparison to S1 and SQX-Me and 95 % of the weight was degraded in one decomposition step. (iii) DSC curves of S2 (top) and S3 (bottom) with heating (and cooling) rates of 10 °C min^{-1}. Remarkably, S3 exhibits cold crystallization at 45 °C, which was unusual for small molecules.

individual amorphous segments was possible again and causes cold crystallization between neighboring groups. This metastable state remains until a temperature is reached where all cold crystals are melted. In case of small molecules, the rapid cooling (also called supercooling) from their liquid state also forms a glass, which upon further heating

recrystallizes and releases heat. This property was exploited for long-term heat storage if the supercooled material was stable enough to not be triggered into spontaneous crystallization.[144] Even though S3 was not further examined in regard to this application, this special property still needs to be noted.
The obtained results on the SQX molecules showed that they exhibit interesting properties, summarizing the analytical data gathered from SQX-H, SQX-Me, S1, S2 and S3, the most reliable methods to identify this molecule class are by

1. optical examination
2. infrared (IR) spectroscopy
3. thermogravimetric analysis (TGA)
4. cyclic voltammetry (CV)
5. solubility in polar protic solvents.

As discussed in the previous passage, all the synthesized SQX molecules exhibited a very high thermal stability with decomposition temperatures above 200 $^{\circ}\mathrm{C}$ and showed nearly no morphological changes over a wide temperature range (with exception of S2 and S3). In non basic solvents, reversibel redox reactions between 0.30 to 0.36 Vvs. Fc/Fc^{+} could be observed. The only exception was SQX-H, due to its limited solubility in a range of common organic solvents. Further, all five SQX molecules shared an insolubility in polar protic solvents like water, methanol and ethanol.
The analysis with Fourier transform infrared (FTIR) spectroscopy revealed distinct bands that appeared in all samples and are suitable to identify the SQX moiety (see Fig. 5.7). With the most protruding structural motives being the carbonyl groups on the cyclobutenedione moiety, the two C=O stretching bands at around 1770 to 1800 cm^{-1} and between 1670 to 1690 cm^{-1} could be observed in all SQX molecules (marked in blue). Another unusual characteristic was a split at around 1500 cm^{-1} that was consistent in all spectra (marked in green). Although this split doesn't correspond to a certain structural motif, it was very noticable. Lastly, the aromatic C-H bend patterns of the phenyl group are also continuously observed in the fingerprint region of the spectra (marked in gray). The main bands (around 750 and 640 cm^{-1}) can be easily covered

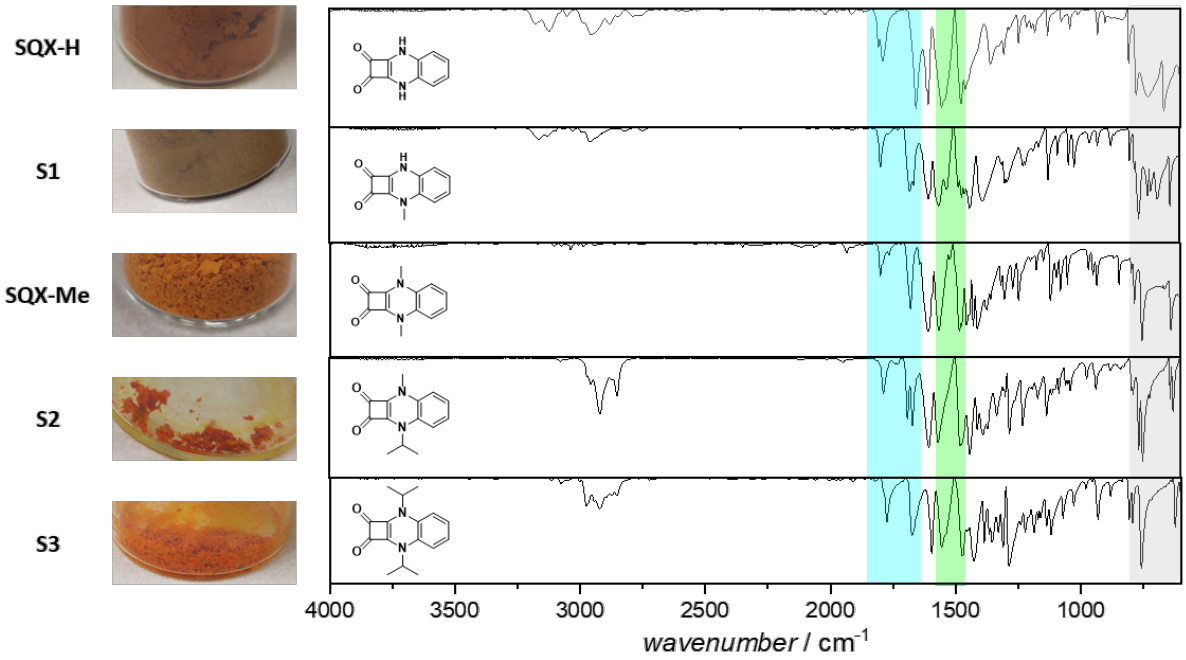

Fig. 5.7 Summary of the investigated SQX molecules in chapter 5.1 and comparison of their characteristic IR bands. All SQX molecules are brightly colored and solid at room temperature. The most distinct bands in IR spectroscopy are marked, in blue: two carbonyl stretches of the cyclobutenedione moiety, the stretch at higher wavenumbers (around 1770 - 1800 cm^{-1}) generally displays a lower intensity than the second carbonyl band (around 100 cm^{-1} lower). In green, a very distinct split at around 1500 cm^{-1} can be observed in all SQX molecules. And lastly, the sp^2 C-H bend pattern of the condensed phenyl ring is marked in gray. The two defining bands are one more intensive band at around 750 cm^{-1}, followed by a lower band at around 640 cm^{-1}.

by other bands due to their low intensities, therefore they are the least distinct bands to identify the SQX moiety.

5.2 Synthesis of SQX monomers and main-chain polymers *via* condensation

After establishing the fundamental characteristics of the SQX moieties, the next step was to prepare monomers to synthesize new SQX containing polymers. The synthesis of these SQX monomers was mainly done by Marcel Baumert from TU Dortmund.
One main challenge in preparing the monomers was to achieve asymmetric substitution of the SQX moiety with an alkyl group on N and the polymerizable unit (PU) on

N'. The central SQX unit could be synthesized *via* two condensation approaches (see Scheme 5.2), starting from a N-alkylated phenylenediamine and squaric acid (SA) (right side) or its ethyl ester (left side), respectively.

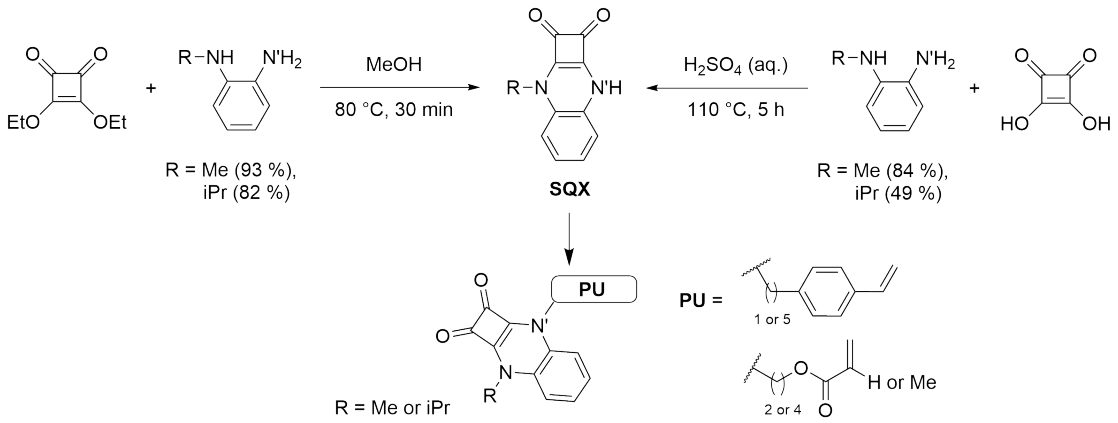

Scheme 5.2 Synthesis of asymmetric SQX monomers. The central structural unit SQX can be obtained by condensation of squaric acid (right) or its ethyl ester (left) with an N-alkylated phenylenediamine in good yields. From there, the polymerizable unit (PU) was attached to the free N' atom. The PUs implemented for the SQX monomers are styrene- and (meth)acrylate-based moieties with different alkyl linker lengths.

It was also attempted to synthesize this unit by alkylation of SQX-H, but either the unreacted starting material or the disubstituted molecules S3 or SQX-Me were isolated. On the free N' atom, a selected polymerizable unit (PU) could be attached *via* nucleophilic substitution, in this case the units were based on styrene and (meth)acrylate moieties. Alkyl linkers of different lengths (from C1 to C5) were added between the SQX and the active polymerizable groups to monitor its influence on the polymer. While the synthesis of the C1 styrene monomer was done by straightforward substitution on vinylbenzenechloride (VBC), in case of the C5 styrene, VBC had to be reacted with dibromobutane in a Grignard reaction first, before the SQX unit was attached.

For the synthesis of the acrylate monomers, SQX-alcohols (ethanol and butanol) had to be synthesized first. To realize this, halogenated alcohols were protected with silyl groups like tert-butyldimethylsilyl (TBDMS) before substitution with SQX to minimize side reactions. This extra protective measure added at least two more steps to the synthesis sequence and increased the overall synthetic effort and simultaneously decreased the yield of the obtained acrylate monomers. The synthesis steps are illustrated with

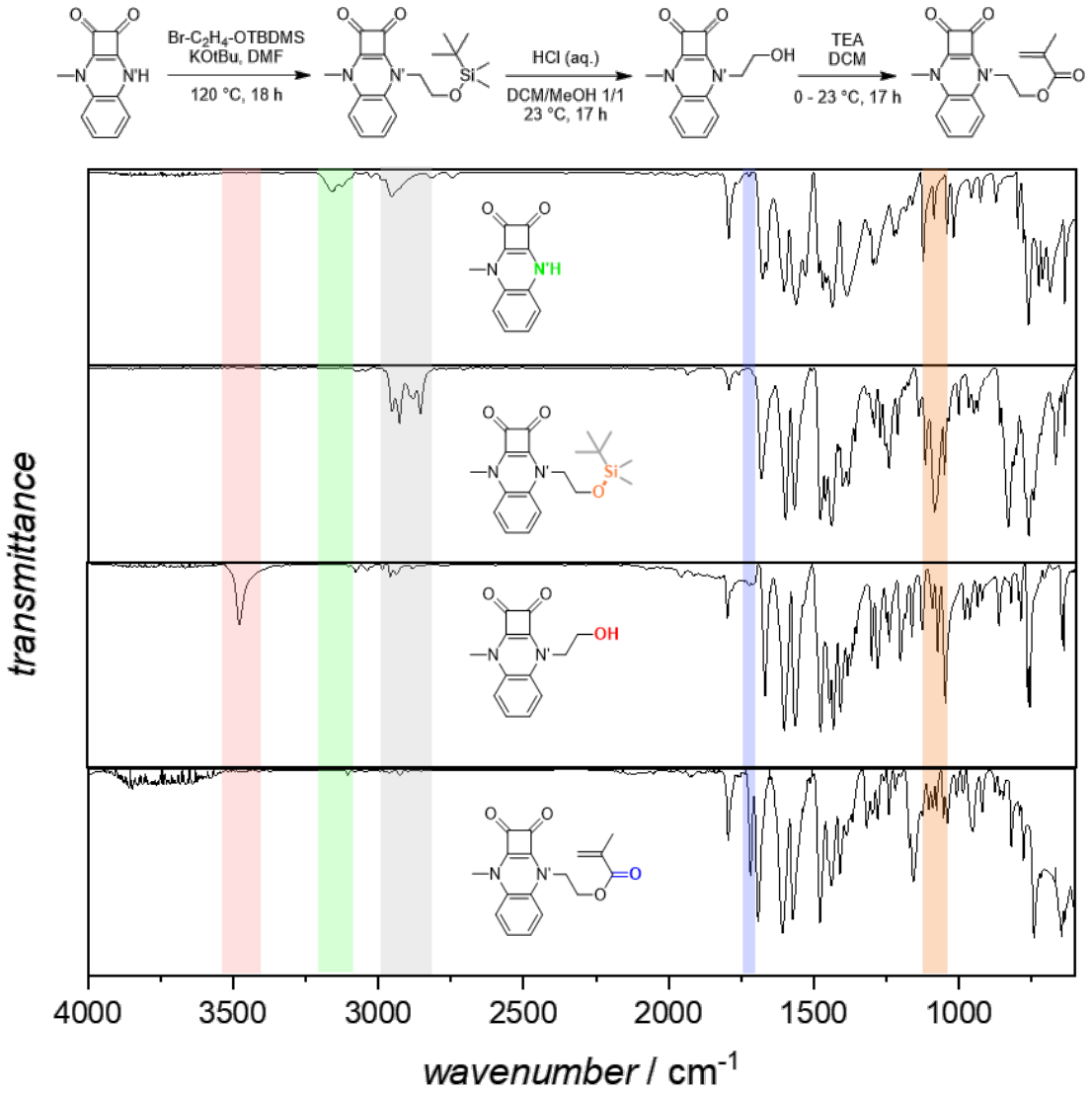

Fig. 5.8 SQX acrylate monomer synthesis on the example of the C2 methacrylate and monitoring with FTIR. The important signals and their corresponding structural motifs are color coded (N-H stretch at ca. 3160 cm^{-1} in green, alkyl sp^3 C-H stretches of TBDMS between 2800 - 3000 cm^{-1} in grey, Si-O-alkyl stretch between 1020 - 1100 cm^{-1} in orange, alcohol O-H stretch at ca. 3480 cm^{-1} in red and acrylic C=O stretch at 1717 cm^{-1} in blue) to track the reaction progress.

the C2 methacrylate serving as an example (see Fig. 5.8). By monitoring the IR spectra of every reaction step, each transformation can be seen clearly while the characteristic bands of the SQX moiety (as discussed in Fig. 5.7) also stayed consistent. This implies that the central structural motif remained undisturbed during the structural modifications

on N'. In total, eight different SQX containing monomers (M1 to M8) were synthesized. Their FTIR spectra are displayed in Fig. 5.9 and their significant IR bands identified in Fig. 5.7 were marked to verify the SQX units inside of all monomers. In the monomers M5 to M8, additional carbonyl signals (marked with black arrows) could be observed, corresponding to the acrylate and methacrylate groups. The styrene-based monomers didn't show further distinctive signals but differences in the alkyl-linker lengths could be tracked in the region around 2900 cm^{-1} when compared carefully. Carbon NMR spectra further verified the depicted monomer structures and the polymerizations of the SQX monomers were discussed in section 5.3.

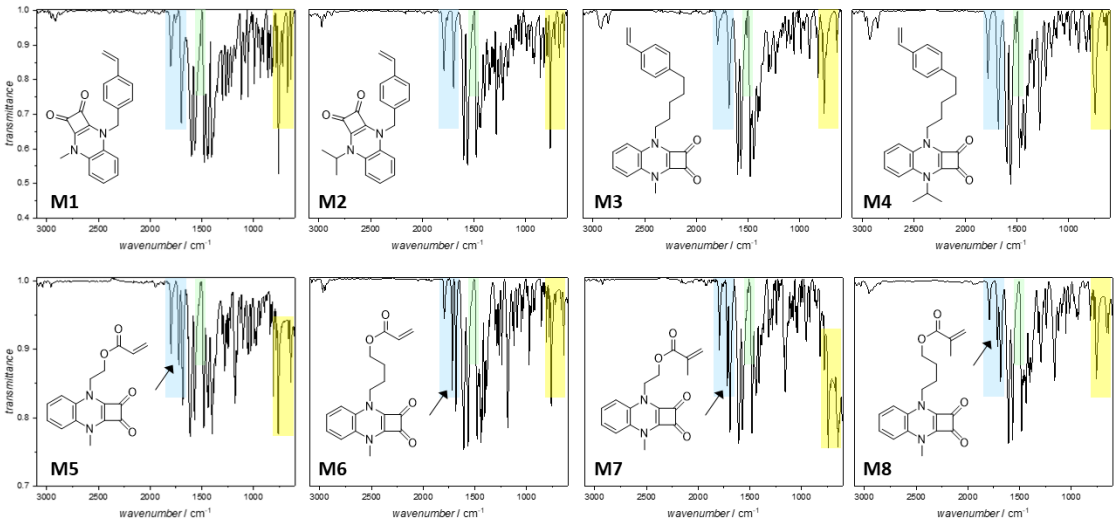

Fig. 5.9 FTIR spectra of the SQX monomers M1 to M8. The SQX-specifying signals were color marked in blue (carbonyl stretches), green (distinct split around 1500 cm^{-1}) and yellow (aromatic C-H bending). All (meth)acrylate monomers (M5 to M8) showed additional carbonyl signals, marked with arrows.

5.2.1 Synthesis of SQX Main Chain Oligomers *via* polycondensation

The symmetric structure of SQX-H with N and N' as substitution sites, renders it a suitable unit for a condensation polymer. One major difficulty was the high stability of SQX-H and its low solubility in most organic solvents. After multiple attempts to activate SQX-H with different bases, potassium tert-butoxide (KOtBu) was selected as

the main base. It could be observed that the addition of KOtBu to SQX-H in DMF caused a visible color change from dark red / brown to a bright red, indicating the successful deprotonation of SQX-H. The deprotonated SQX-H was then reacted with suitable dibromo-electrophiles to attempt polycondensation (see Scheme 5.3).

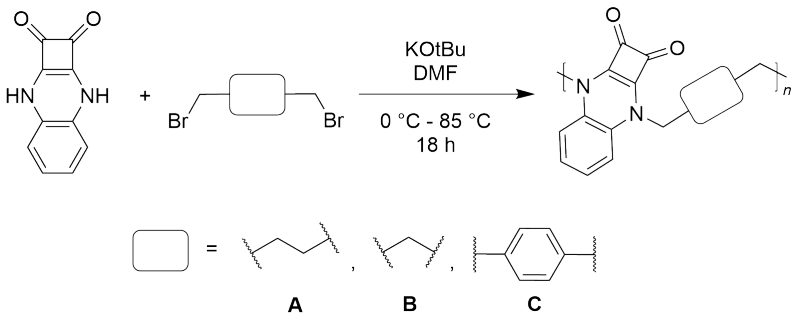

Scheme 5.3 Synthesis of SQX main chain polymers *via* polycondensation of SQX-H with dibromo electrophiles (A = dibromobutane, B = dibromopropane and C = dibromo-p-xylene). Potassium tert-butoxide (KOtBu) was used as the base to activate SQX-H by deprotonation. The successful activation could be observed as a color change from dark red / brown to a bright red, after the addition of the electrophiles the reaction mixtures slowly turned brown again.

Following the naming of the electrophiles in Scheme 5.3, the condensation products are labeled as PA, PB and PC, respectively. The precipitated crude products were washed with water and extracted with DCM to remove any traces of potassium tert-butoxide. For PA, the crude product was dissolved in toluene and precipitated in diethylether repeatedly to remove DMF. The NMR analysis in deuterated DMSO showed that the precipitate was a mixture of starting material and condensation products (see appendix). This was also confirmed by SEC since the SEC trace clearly shows three signals: monomer units, di- or trimers and higher oligomers (from left to right). The same problem was encountered with PB, the NMR analysis showed a lot of signals that are difficult to assign (see appendix) and the SEC trace also had a similar appearance like the trace from PA and shows more than one signal. In contrast to these, the SEC trace of PC showed a broad multimodal signal shifted to higher molecular weights and with a significantly smaller first monomer signal. Even though this SEC trace still indicated the formation of a lot of oligomers, the change from dibromoalkanes to dibromo-p-xylene as the condensation partner for SQX lead to higher conversion and seemed to represent a more suitable co-reagent for polycondensation. To make better use of these condensation polymers, the

reaction conditions and starting materials would have to be further optimized to ensure full conversion to high molecular weight polymers with a unimodal SEC distribution.

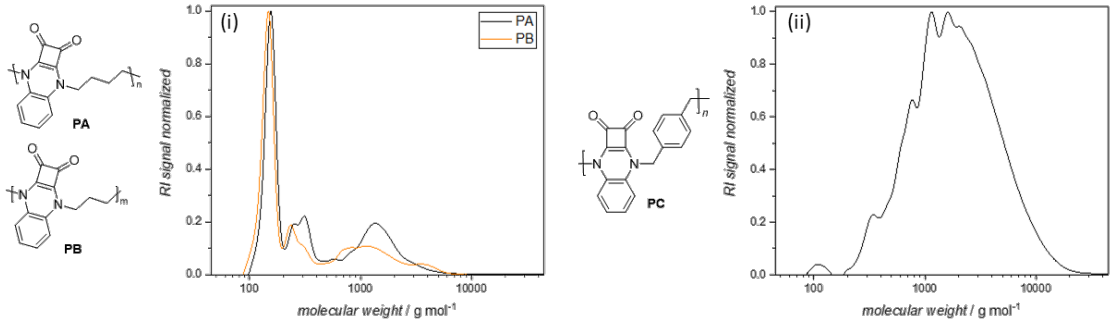

Fig. 5.10 Condensation products of SQX-H with dibromobutane (PA), dibromopropane (PB) and dibromo-p-xylene (PC). The displayed SEC traces were recorded in dimethylacetamide (DMAc) at 50 °C and calibrated with polystyrene standards. (i) SEC elugrams of PA (in black) and PB (in yellow). Both elugrams show three signals, corresponding to unreacted starting material, small oligomers and heavier oligomers (from lower to higher molecular weight). Since the first band displays the highest RI signal, it can be assumed that the conversion of the starting molecules was very low. (ii) SEC elugram of PC with one main multimodal signal. The shape of this signal corresponds to the underlying polycondensation, so that each peak represents an oligomer with one condensation unit more than the previous peak. The small band at low molecular weights indicates a high conversion of the starting materials.

PC was further examined in regard to its thermal properties *via* thermogravimetric analysis (TGA) and differential scanning calorimetry (DSC) (Fig. 5.11). From evaluation of the TGA curve, the decomposition of PC under nitrogen atmosphere appeared to undergo in one main step. The observed weight loss corresponded to the decomposition of the cyclobutenone moieties on the SQX units and xylene linkers, therefore the residual weight at 900 °C corresponded to the phenylenediamine moieties of the SQX groups. This decomposition behavior was unexpected as the SQX molecules examined in section 5.1 all completely decomposed under nitrogen atmosphere in one or two steps. A cause for this change could be that the polymerized SQX units influence the overall thermal stability as the decomposition temperature of PC was also lowered to 213 °C. The formation of polymer was likewise shown *via* DSC by the recorded glass transition at 95 °C. Following the analysis of the thermal properties, PCs electrochemical properties were examined with cyclic voltammetry. The CV in acetonitrile showed a reversible oxidation at 0.45 V vs. Fc/Fc^+, which was significantly higher than the redox potentials recorded for the SQX small molecules in section 5.1. This redox reaction also seemed

to be very reversible over three CV cycles (at a scan rate of 100 $\mathrm{mV\,s^{-1}}$). Therefore it could be concluded that PC might be a promising new redox-active polymer containing the SQX moieties as functional groups. To test PCs applicability as an organic electrode material, the redoxactivity in a half-cell would need to be tested (similar to SA2 in section 4.2). From the solution CV it was shown that PC had a low solubility in acetonitrile. A low solubility in organic solvents would be beneficial since dissolution was always a main concern for organic electrode materials. Therefore, PC displays a promising new SQX containing redox material for potential application in organic batteries. The straightforward one-step synthesis also renders this polymer interesting for larger scale application.

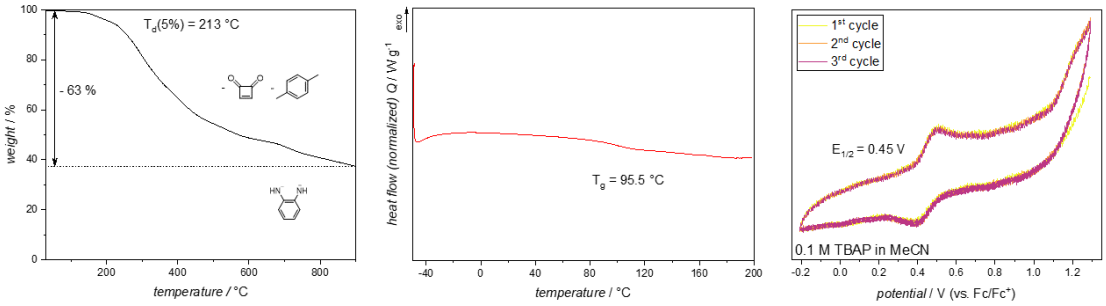

Fig. 5.11 Properties of the SQX main chain polymer PC. Left: TGA in nitrogen atmosphere with a heating rate of 10 $\mathrm{K\,min^{-1}}$. The recorded decomposition temperature was determined as 213 °C and the TGA curve showed an incomplete decomposition of PC at 900 °C with more than a third of the initial material weight left. Middle: Second heating curve of the DSC measurement. The glass transition was determined at 95 °C. Right: CV of PC in 0.1 M TBAP in acetonitrile at a scan rate of 100 $\mathrm{mV\,s^{-1}}$ with ferrocene as an internal reference. The redox reaction at 0.45 Vseemed reversible over three cycles but the responding current was very low due to the low solubility of PC.

5.3 Synthesis of new SQX containing Homopolymers

After it was successfully shown in section 5.1 that the SQX small molecules were stable (chemically and thermally) and exhibited reversible oxidations in dry solutions, the next step was to integrate them into polymers and expand their potential application as ROMs. It has to be addressed beforehand that the number average molecular weights (M_ns) of the polymers were estimated by size-exclusion chromatography (SEC) in *N,N*-dimethylacetamide (DMAc) using calibration curves based on polystyrene and polymethylmethacrylate (PMMA) standards. Since the effective interaction of the SQX polymers with the SEC columns is unknown, all denoted M_n values have to be taken with caution.

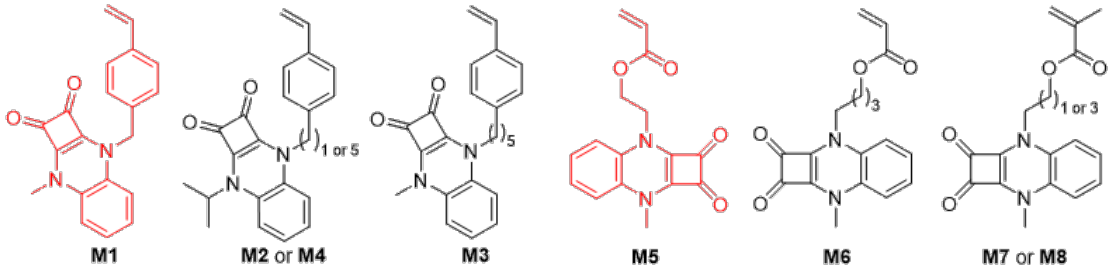

Fig. 5.12 SQX monomers for homopolymerization. The monomers M1 and M5 (in red) didn't show any conversion after exposition to radical polymerization conditions.

The synthesis of the SQX monomers (see Fig. 5.12) was mainly carried out by M. Baumert from the Hansmann group at TU Dortmund and is briefly described in section 5.2. SQX monomers with three different main polymerizable units were synthesized, namely styrene, acrylate and methacrylate. These polymerizable units were separated from the functional SQX moiety by different alkyl linkers with varying lengths from one to five CH_2 units. These lengths were selected to investigate the influence of the chain mobility on the polymerization conditions and resulting polymer properties.

It was generally observed, that the conversion of monomers in the polymerization was not very high (up to 49 %, see Table 5.1) which could be attributed to their limited solubility in the tested polymerization solvents like DMF, 1,4-dioxane, NMP or toluene, despite the effort of RAFT polymerization to maintain lower molecular masses. The amount of solvent was selected to match a concentration of 1 $\mathrm{mmol\,mL^{-1}}$ prior to

Table 5.1 Polymerization conditions of the SQX polymers P2 to P8.

monomer	time / h	temp. / °C	polymer	M_n / g mol^{-1}	Đ	yield / %
M1 [a,c,d]	5	80	**-**	-	-	-
M2 [a]	25	90	**P2**	10 500	1.29	49
M3 [a]	25	90	**P3**	3 500	1.47	27
M4 [c]	7	80	**P4**	10 300	1.29	21
M5 [b,c,d]	5	80	**-**	-	-	-
M6 [c]	3	90	**P6**	3 080	1.34	24
M7 [c]	2	90	**P7**	4 400	1.13	9
M8 [c]	3	90	**P8**	7 200	1.74	35

The following conditions were applied for all polymerizations: The monomer concentration was set to 1 mmol mL^{-1}, AIBN was used as an initiator and dry DMF was used as the solvent. a) RAFT polymerization, dibenzyl trithiocarbonate (DBTTC) was used as chain transfer agent (CTA); b) RAFT polymerization, 4-Cyano-4-[(dodecylsulfanylthiocarbonyl)sulfanyl]pentanoic acid was used as CTA; c) free radical polymerization (FRP); d) no polymer formation

polymerization. However, the quantity of the solvent was generally not enough to fully dissolve all the monomers and obtain a clear solution prior to polymerization. When the volume of the solvent was adjusted to fully dissolve all monomers, polymerization didn't occur, most likely because the solution was too dilute (around 0.1 mmol mL^{-1}). For this reason, the polymerizations were carried out in melt without being fully dissolved. The incomplete conversion therefore is most likely a result from undissolved monomers not participating in the polymerization.

All obtained polymers, P2 to P8, were analysed and characterized by their thermal properties (decomposition temperature T_d(5%), where 5 % of the material weight is lost, and glass transition temperature T_g) and their electrochemical redox properties in solution. The relevant properties of the SQX monomers and their respective polymers are summarized in Table 5.2.

The first obtained SQX-homopolymer was synthesized from the styrene based monomer M2 by reversible addition-fragmentation chain-transfer (RAFT) polymerization with S,S-dibenzyl trithiocarbonate (DBTTC) as the chain transfer agent (CTA). Despite a lot of effort, the monomer M1 could not be polymerized in radical polymerization conditions even after variation of the concentration, solvent and initiator. Interestingly, the only structural difference between M1 and M2 was the replacement of the alkyl-group

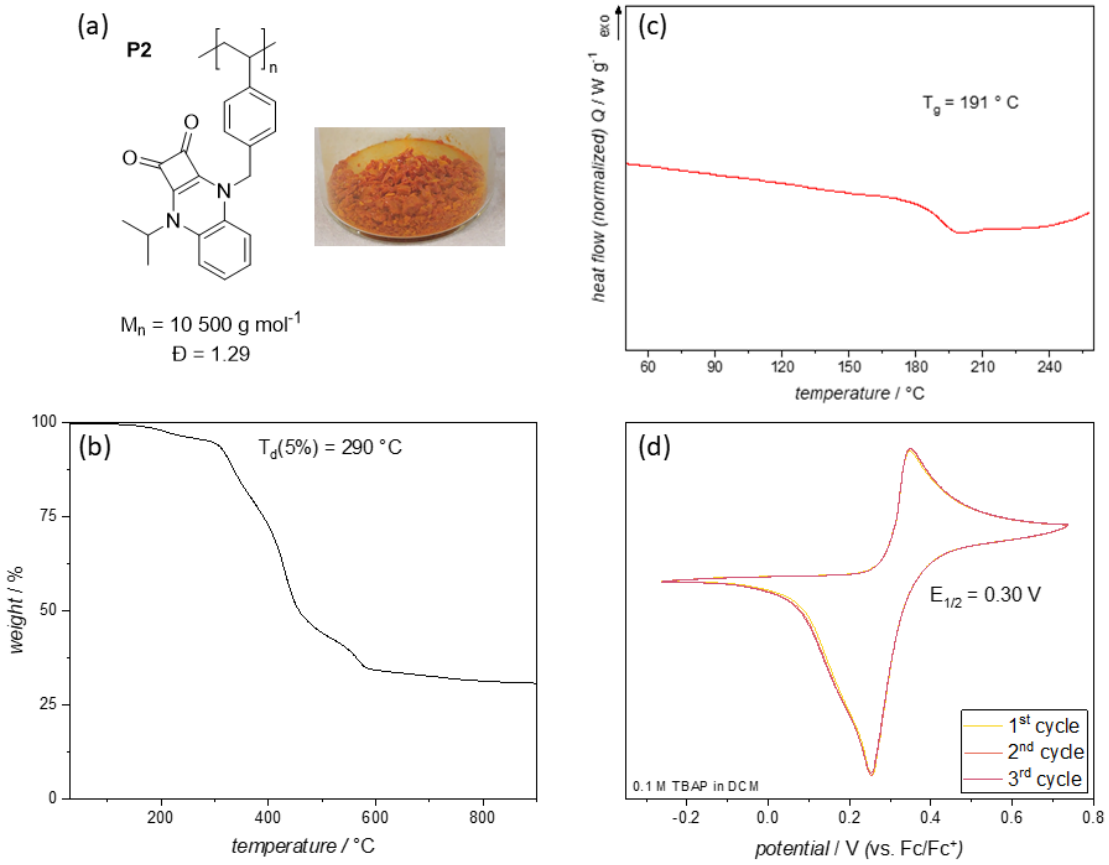

Fig. 5.13 Basic characterization of SQX homopolymer P2. (a) Structure, appearance, molecular weight distribution (M_n) and dispersity Đ of P2. (b) Thermal decomposition of P2 under nitrogen, determined by TGA. The decomposition temperature T_d(5%) was remarkably high at 290 °C. (c) DSC curve of P2 shows a glass transition point T_g at 191 °C. (d) CV in 0.1 tetrabutylammonium perchlorate (TBAP) in dry DCM. Ferrocene was used as an internal reference and the redox potential $E_{1/2}$ was determined as 0.32 V (vs. Fc/Fc^+).

at N from methyl to isopropyl. This subtle change enabled M2 to be polymerized and the resulting polymer P2 was obtained as a bright orange solid. To verify the polymer formation and implementation of SQX functional groups, the polymer was analyzed with NMR (^{1}H and ^{13}C), Fourier transform infrared (FTIR) and size-exclusion chromatography (SEC). P2 showed exceptional thermal stability (T_d(5%) = 290 °C) and a very high glass transition at 191 °C (see Fig. 5.13 c). The elongation of the alkyl linker between the SQX and the styrene moiety from one to five CH_2 units made the polymerization of the monomer M3 possible, even with a methyl group at the other N atom, to obtain the polymer P3 as an orange solid (see Fig. 5.14). P3 showed a redox

potential in the same order as P2 ($E_{1/2}$(P3) = 0.34 V vs. Fc/Fc^+ compared with $E_{1/2}$(P2) = 0.32 V). This polymer also showed a very high thermal stability above 300 °Cbut a lowered glass transition point at 75.9 °C according to DSC analysis. The lowered T_g was anticipated since the longer C5 alkyl linker was expected to enhance the mobility of the polymer chain.

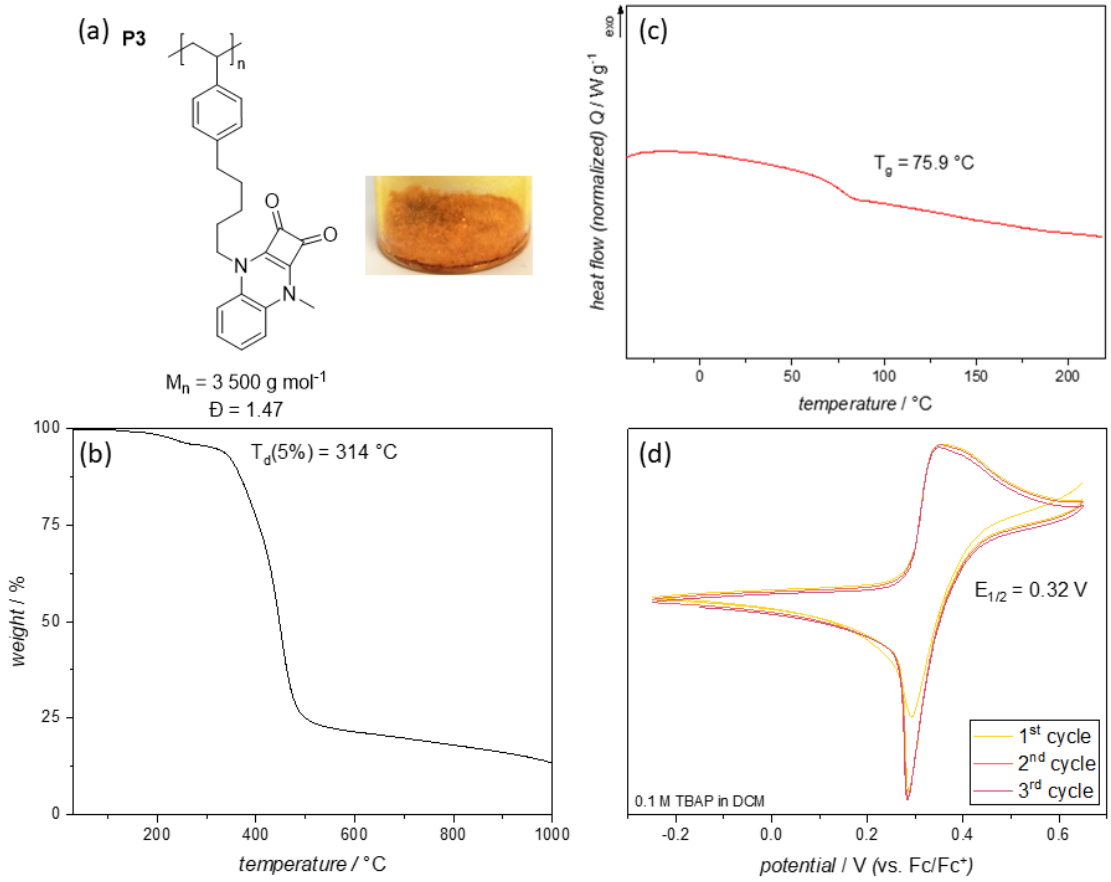

Fig. 5.14 Basic characterization of SQX homopolymer P3. (a) Structure, appearance, M_n and Đ of P3. (b) Thermal decomposition under nitrogen, T_d(5%) was determined to be 314 °C. (c) DSC curve of P3 shows a glass transition point T_g at 75.9 °C. (d) CV in 0.1 tetrabutylammonium perchlorate (TBAP) in dry DCM. Ferrocene was used as an internal reference and the redox potential $E_{1/2}$ was determined as 0.34 V (vs. Fc/Fc^+).

The third SQX homopolymer P4 was also a polystyrene-based polymer obtained from the monomer M4, this time with an isopropyl group on the second N atom of the SQX moiety (see Fig. 5.15). This polymer was obtained as a fine yellow powder and also showed a high thermal stability and a reversible redox reaction at 0.3 V vs. Fc/Fc^+

according to CV. To synthesize polyacrylate based SQX homopolymers, the monomers

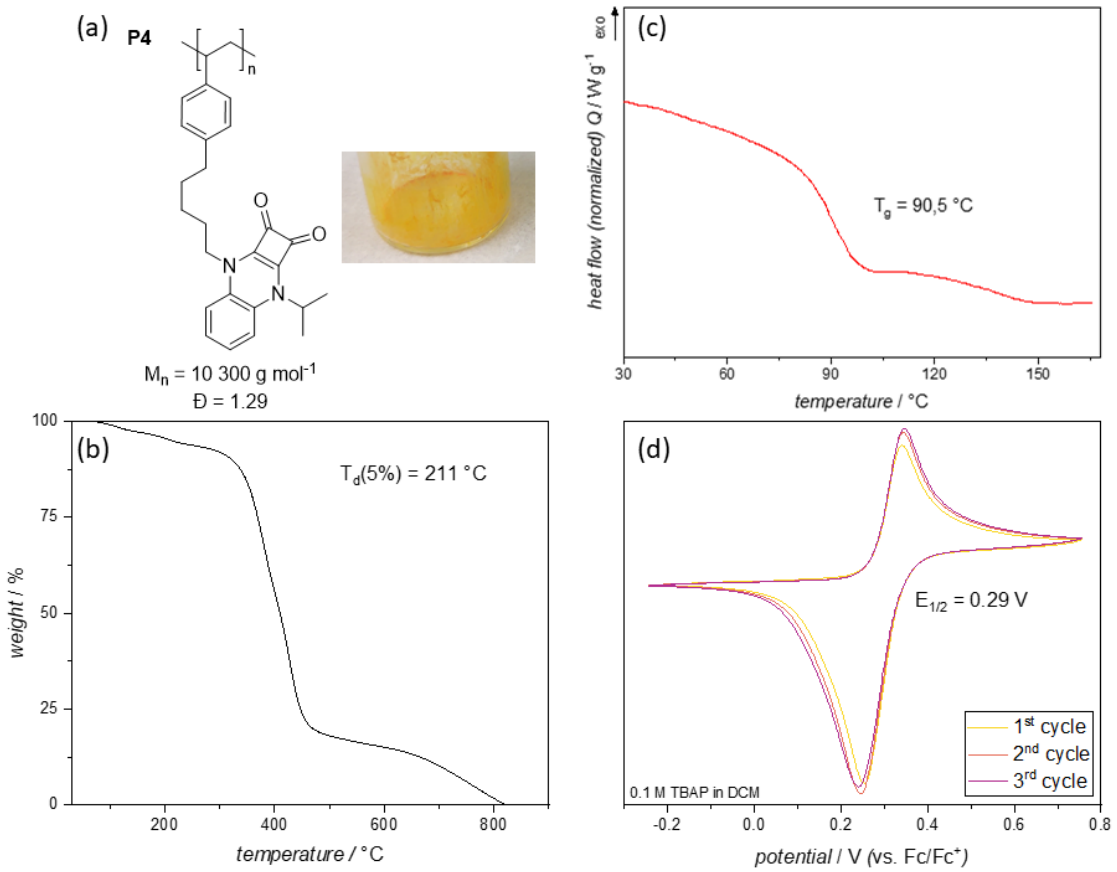

Fig. 5.15 Basic characterization of SQX homopolymer P4. (a) Structure, appearance, molecular weight distribution (M_n) and dispersity Đ of P4. (b) Thermal decomposition of P3 under nitrogen, T_d(5%) was determined to be 211 °C. (c) DSC curve of P4 shows a glass transition point T_g at 90.5 °C. (d) CV in 0.1 tetrabutylammonium perchlorate (TBAP) in dry DCM. Ferrocene was used as an internal reference and the redox potential $E_{1/2}$ was determined as 0.30 V (vs. Fc/Fc$^+$).

M5 and M6 were prepared (see Fig. 5.12). Multiple attempts were made to polymerize M5 with different initiators, CTAs, temperatures and solvents. Despite these efforts, M5 was always recovered unreacted with no indication of a successful conversion. The addition of two CH_2 units to extend the linker between the acrylate and SQX moiety to obtain the monomer M6 finally enabled the synthesis of the acrylate homopolymer P6 (see Fig. 5.16). The bright orange polymer also shows a remarkable high thermal stability and a fairly low T_g at 5.9 °C which is not unusual for polyacrylate (for comparison,

the T_g of polymethylacrylate in literature is 14 °C).[145] Additionally, the redox potential of P6 was slightly higher than the potentials of the styrene-based polymers at 0.41 V vs. Fc/Fc^+. These properties are interesting as P6 could be prepared for electrodes with less supplementary additives. Interestingly, in the case of the methacrylate monomers

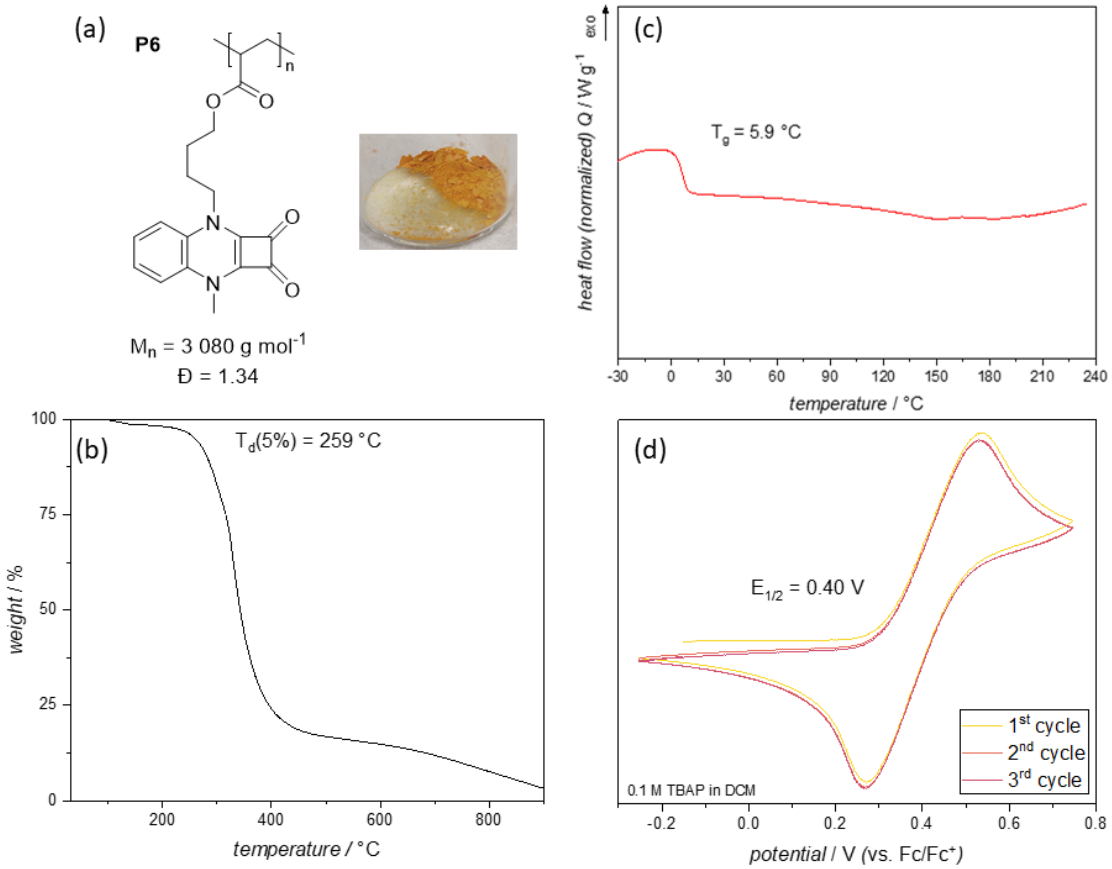

Fig. 5.16 Basic characterization of SQX homopolymer P6. (a) Structure, appearance, M_n and Đ of P6. (b) Thermal decomposition of P6 under nitrogen (T_d(5%) = 259 °C). (c) DSC curve of P6 shows a very low glass transition at 5.9 °C. (d) CV in 0.1 tetrabutylammonium perchlorate (TBAP) in dry DCM. Ferrocene was used as an internal reference and the redox potential $E_{1/2}$ was determined as 0.41 V (vs. Fc/Fc^+).

M7 and M8, both could be polymerized radically despite M7 having a very similar structure to the non polymerizable M5. From these two monomers the SQX polymers P7 and P8 were obtained as a yellow and a dark orange solid, respectively. These SQX-polymethacrylates showed, in line with the other SQX polymers, very high thermal stabilities with decomposition temperatures around 270 °C and high glass transition

temperatures.

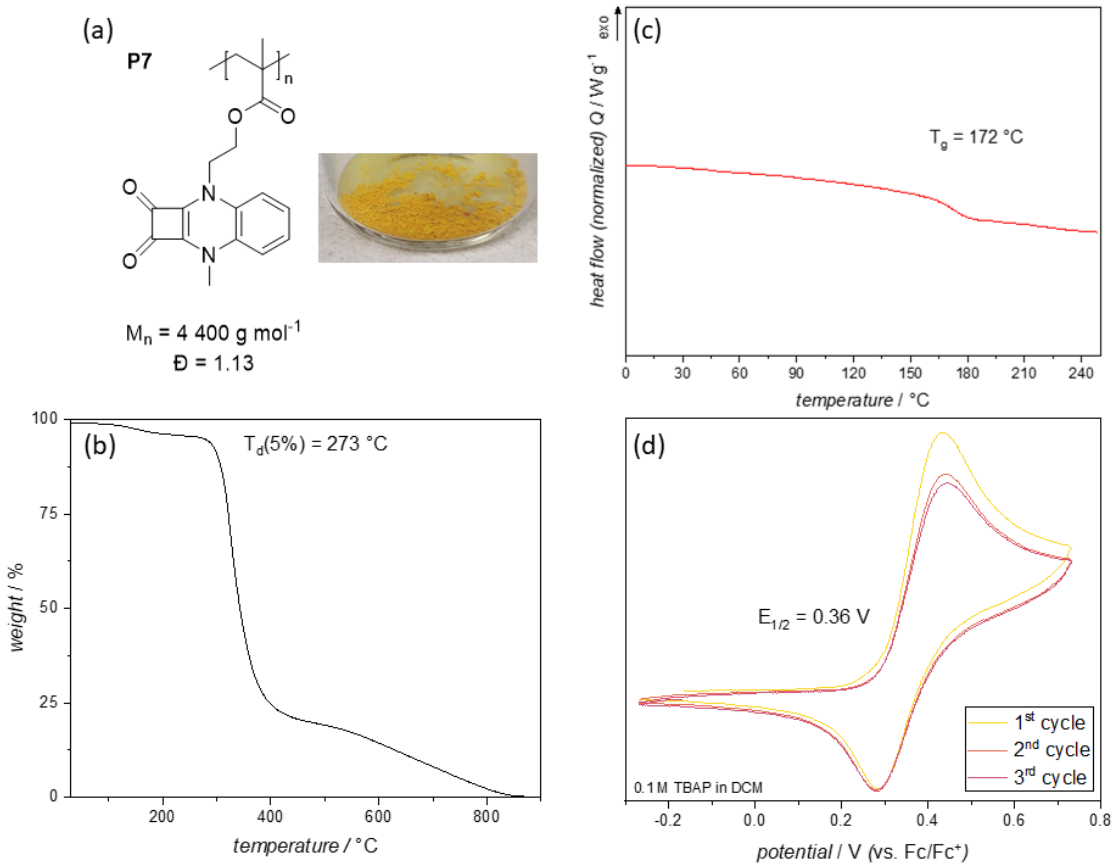

Fig. 5.17 Basic characterization of SQX homopolymer P7. (a) Structure, appearance, M_n and Đ of P7. (b) Thermal decomposition of P7 under nitrogen, T_d(5%) was determined to be 273 °C. (c) DSC curve of P5 shows a glass transition point T_g at 172 °C. (d) CV in 0.1 tetrabutylammonium perchlorate (TBAP) in dry DCM. Ferrocene was used as an internal reference and the redox potential $E_{1/2}$ was determined as 0.35 V (vs. Fc/Fc$^+$).

In conclusion, from TGA it was apparent, that all SQX polymers exhibited the same remarkable thermal stability as their monomers in nitrogen atmosphere with decomposition temperatures above 250 °C (except for P4). This high thermal stability could enable the processing of these polymers at elevated temperatures without thermal decay of the polymers or their functional groups. All polymers featured one main decomposition step that was concluded around 600 °C, indicating a shared decomposition mechanism between the SQX polymers. Interestingly, the thermal stability didn't seem to correlate

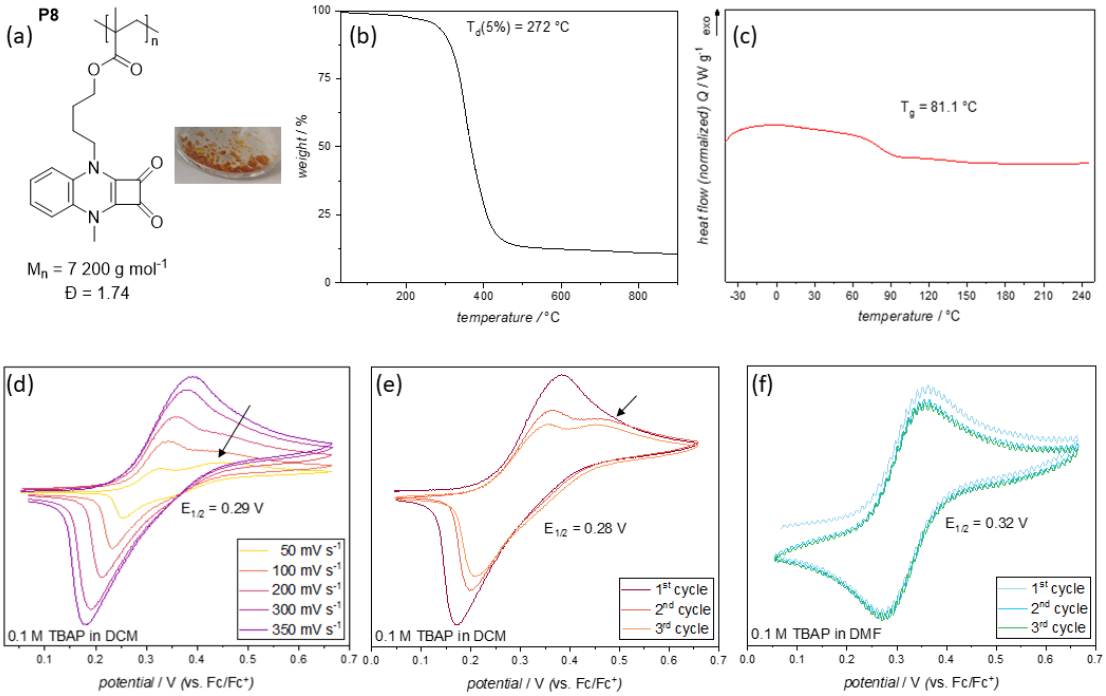

Fig. 5.18 Basic characterization of SQX homopolymer P8. (a) Structure, appearance, M_n and Đ of P8. (b) TGA of P8, T_d(5%) = 272 °C. (c) DSC curve of P8 shows a glass transition point T_g at 81.1 °C. (d) CV of P8 in 0.1 tetrabutylammonium perchlorate (TBAP) in DCM at different scan rates. At low scan rates under 300 mV s^{-1}, a second oxidation peak appears at 0.44 Vadditionally to the redox potential $E_{1/2}$ at 0.29 V(vs. Fc/Fc$^+$). (e) 3 CV cycles were run with a scan rate of 350 mV s^{-1} in DCM. After the first cycle, the current significantly dropped and the second oxidation peak (indicated by an arrow) at 0.44 Vappeared. (f) CV of P6 in DMF with a scan rate of 100 mV s^{-1} shows a reversible oxidation over 3 cycles at a redox potential of 0.32 V.

with the structure of the monomer units as the highest T_d was exhibited by P3 whose structure is polystyrene based with a C5 linker between the polymerizable unit and the SQX unit. P4 had the same polystyrene structure as P3, the only difference was an isopropyl group on the SQX N atom instead of a methyl group. Despite this small structural change, the decomposition temperature of P4 was decreased by 100 °C compared to P3. This drastic effect can't be explained solely by the substitution of the isopropyl group, since P2 is isopropyl substituted with a T_d close to 300 °C.

The glass transition temperatures on the other hand, corresponded well with the underlying polymer structures. In case of the polystyrene based polymers, P2s T_g value was remarkably high with 191 °C due to its rigid structure and bulky isopropyl group limiting the chains mobility. The T_gs of P3 and P4 were in the range of pure PS polymers

Table 5.2 Comparison of relevant properties of the SQX monomers with their respective polymers.

monomer	T_d(5%) / °C[a]	E / V[b]	polymer	T_d(5%) / °C[a]	E / V[b]	T_g / °C
M1	285	0.42	-	-	-	-
M2	308	0.41	P2	290	0.30	191
M3	330	0.31	P3	314	0.32	75.9
M4	233	0.35	P4	211	0.29	90.5
M5	279	0.41	-	-	-	-
M6	250	0.39	P6	259	0.40	5.9
M7	252	0.44	P7	273	0.36[c]	172
M8	200	0.27	P8	272	0.28[c]	81.1

a) Thermal gravimetric analysis (TGA) was carried out under nitrogen atmosphere. b) CV was measured in 0.1 M TBAP in DCM with scan rates ranging from 50 $\mathrm{mV\,s^{-1}}$ to 400 $\mathrm{mV\,s^{-1}}$. Ferrocene was used as an internal reference (all potentials were referenced vs. Fc/Fc^+), for comparison: the redox potential of TEMPO in DCM was determined as 0.27 V (vs. Fc/Fc^+). c) CV over 3 cycles showed a rapid decrease of the responding current.

but being slightly lowered which could be ascribed to the higher mobility of the side groups thanks to the C5 linker.[139] Additionally, the effect of the SQX side groups on the T_gs was also shown as P3s methyl groups corresponded to the lower and P4s isopropyl groups corresponded to the higher values, respectively. From the poly-(meth)acrylate based polymers, P6 had the lowest glass transition temperature at 6 °C. This low T_g value was in line with values previously reported for other poly-acrylate polymers.[146] As expected, the poly-methacrylates P7 and P8 had higher T_gs, with P8 showing a lower glass transition in direct comparison due to the higher chain mobility provided by the longer linker. In regard to the electrochemical redox properties of these polymers, the impact of the structure on the redox potential was ambiguous. All polymers exhibited a reversible oxidation in DCM at potentials above 0.3 V vs. Fc/Fc^+, which was higher than the redox potential of TEMPO in DCM (0.27 V vs. Fc/Fc^+). It was observed that the (meth)acrylate-based polymers generally showed slightly higher redox potentials compared to the polystyrene homopolymers (Table 5.2). The highest values were recorded for P6 and P7 with 0.39 V and 0.36 V vs. Fc/Fc^+, respectively. It was observed that the CV of P7 over 3 cycles showed a rather rapid decrease in the current after each cycle (Fig. 5.17), especially in direct comparison to the very reversible CV of P2 (Fig. 5.13). This would indicate either dissolution of the radical cations in the electrolyte solution or

their decomposition due to instability. It was therefore questionable if P7 is suitable for battery applications since dissolution of organic cathode material is a main concern for bad cyclability and rapid capacity loss in organic batteries.[8] In general, it was observed that the oxidations of the SQX polymers were very reversible over 3 CV-cycles and could be potentially interesting for further electrochemical testing. Nevertheless, the redox potentials were systematically lower than the potentials of their corresponding monomers (Table 5.2).

5.3.1 Electrochemical Testing of the SQX Homopolymers as Cathode Materials

The long-term goal was to implement these SQX polymers as potential cathode materials for battery applications. Therefore, electrodes containing the SQX polymers (SQX-SC-65) were fabricated and built into Li-half cells to investigate their electrochemical performance. The commercial electrolyte LP-30 (1 M $LiPF_6$ in ethylene carbonate (EC) : dimethyl carbonate (DMC), 5:5 wt-%) was utilized for the electrochemical measurements. All of the following described electrochemical experiments were carried out by P.-H. Su at HIU.

The results of the CVs in LP-30 with a scan rate of 0.1 $\mathrm{mV\,s^{-1}}$ are shown in Fig. 5.19. First of all, it can be noted that the redox potentials of all polymers surpassed the potential of PTMA in the same electrolyte (3.62 V vs. Li/Li^+). Especially the SQX polymer P7 showed a higher redox potential (3.73 V vs. Li/Li^+) than the rest of the SQX polymers (see Fig. 5.19). The CV of P8 revealed an unexpected value for its redox potential, 3.66 V versus Li/Li^+, as shown in Figure S19. From the result of the CV in DCM, its redox potential, 0.28 V vs. Fc/Fc+, was lower than the values for all the other polymers and was expected to be lower in lithium half-cells as well. Interestingly, the redox potential of P8 in a lithium half-cell was actually higher than the potentials of P3, P4 and P6, which are 3.64 V, 3.63 V and 3.65 V versus Li/Li^+, respectively (see Fig. 5.19). In comparison to PTMA, which showed a stable electrochemical redox behavior by maintaining responding currents over multiple cycles, a continuous decrease of responding currents was observed in the CVs of all SQX polymers, implying that SQX polymers might be

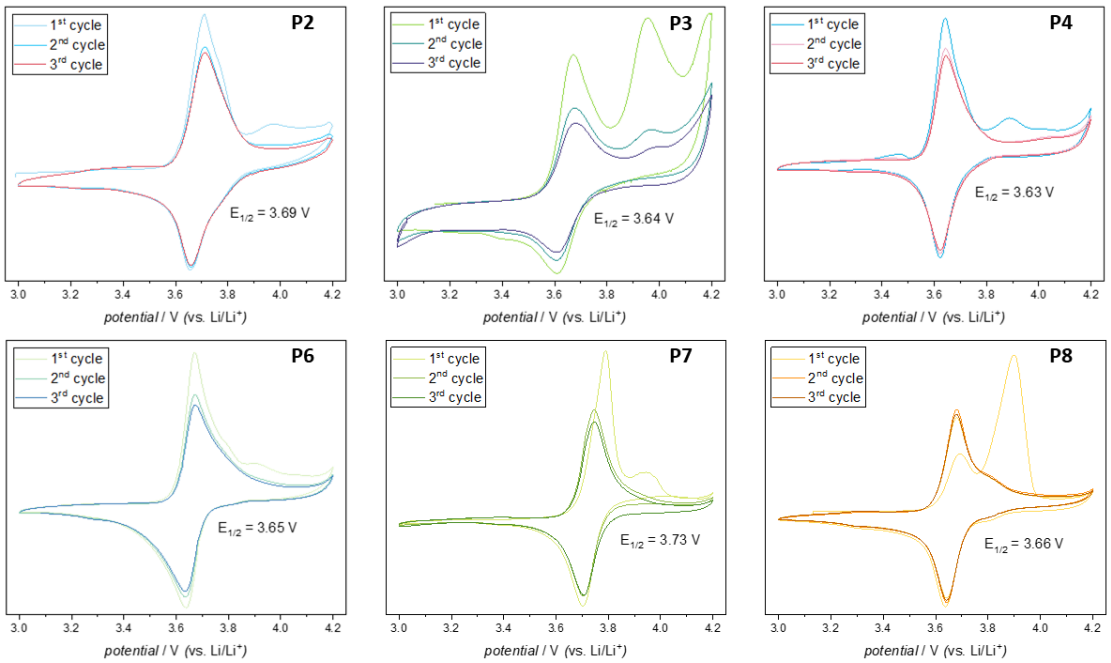

Fig. 5.19 CVs of the SQX homopolymers P2 to P8 in LP-30 at a scan rate of 0.1 $\mathrm{mV\,s^{-1}}$. All CVs showed an irreversible oxidation at around 3.9 V vs. $\mathrm{Li/Li^+}$ that disappeared after the first cycle (except for P3).

highly dissoluble in the electrolyte. Additionally, the SQX polymers showed an additional irreversible oxidation reaction at around 3.9 V vs. $\mathrm{Li/Li^+}$ with a different degree compared to the reversible redox reaction. Especially in P8, the responding current of the oxidation peak in the first cycle appeared much more significant than the current of the redox reaction at 3.66 V vs. $\mathrm{Li/Li^+}$. In the second cycle, the oxidation disappeared and the current of the redox reaction is increased compared to the first cycle.

To alleviate the irreversible oxidation, electrodes with the addition of graphene as the second conductive matrix were fabricated (SQX-SC-65-G). The CV results of P4 and P8 in the new electrode configuration are displayed in Fig. 5.20. In P4, the addition of graphene slightly increased the current of both irreversible oxidations at 3.9 V and above 4.0 V, respectively. Although the implementation of graphene reduced the relative current of the irreversible oxidation at 3.9 V of P8 effectively, it simultaneously induced a significant increase of the responding current of the irreversible oxidation reaction above 4.0 V vs. $\mathrm{Li/Li^+}$. This phenomenon was especially serious in the SQX polymer P6 in the new electrode composition SQX-SC-65-G. As seen in Fig. 5.20, P6 displayed different reversibility in SQX-SC-65-G if the potential ranges were modified (Fig. 5.20

c and d). When the upper potential limit was set to 4.2 V , the currents of the reverse scans showed unusual behavior and the reduction peak of the redox reaction disappeared after the first CV cycle. Cutting the upper limit to 4.0 V avoided this effect and resulted in a reversible redox reaction over all three cycles.

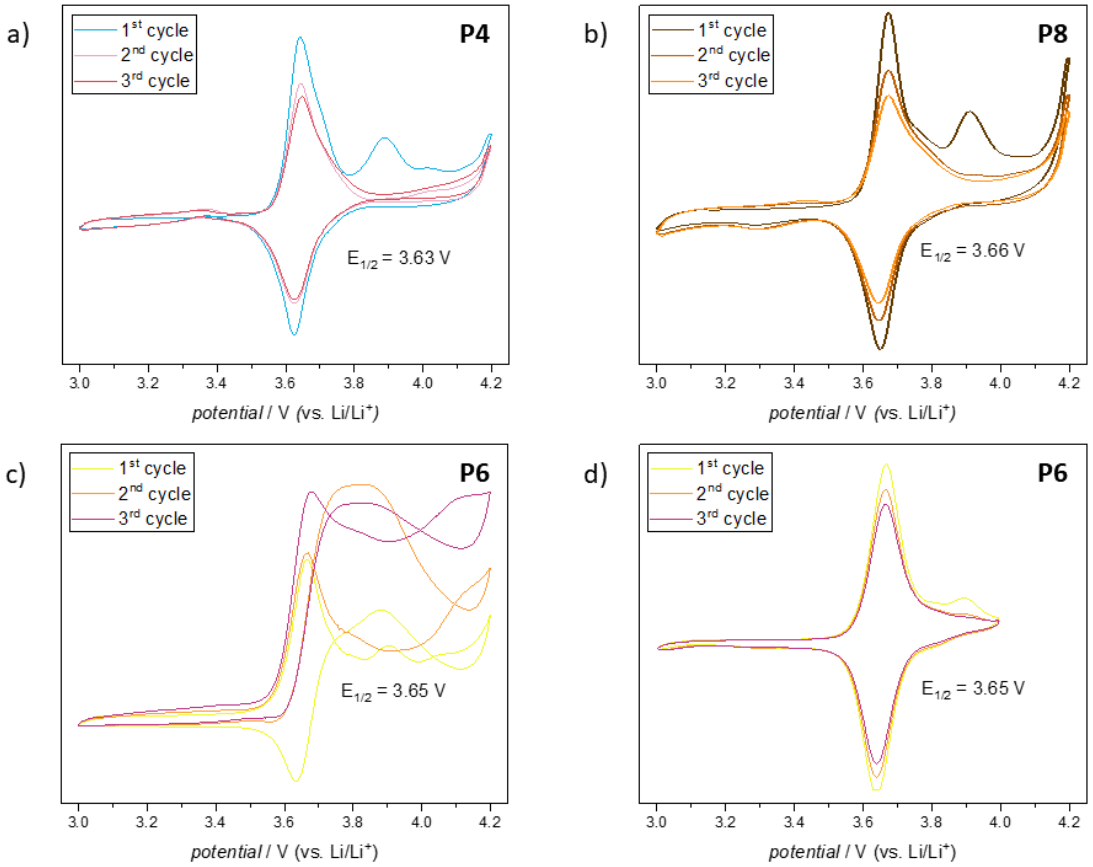

Fig. 5.20 CVs of the SQX polymers P4 (a), P8 (b) and P6 (c and d) recorded in LP-30 with graphene as additional conductive matrix (SQX-SC-65-G). The addition of graphene enhanced the irreversible oxidation above 4.0 V in all recorded CVs and, in case of P6, even influenced the stability of the redox reaction (as displayed in c)). Limiting the upper potential range to 4.0 V stabilized the redox reaction at 3.65 V(see d)).

Following these results, the cut-off voltages of galvanostatic cycling were set to 3.0 V and 4.0 V vs. Li/Li^+, since the irreversible oxidation after 4.0 V became pronounced after the addition of graphene to the electrode (Fig. 5.20). In this voltage range, all SQX polymers were stable and mainly showing reversible redox reactions. Based on the CV

results, the performances of selected SQX polymers, P2, P4 and P8, were further investigated in regard to their cyclability. P2 and P4 were selected due to the good reversibility of the CVs after the first cycle and their less pronounced diffusion effect corresponding to the dissolution of active material from the electrodes in comparison to P6 and P7. On top of this, P8 was also selected due to the significant effect of graphene on the irreversible oxidation at 3.9 V. The electrochemical performance of the SQX polymers

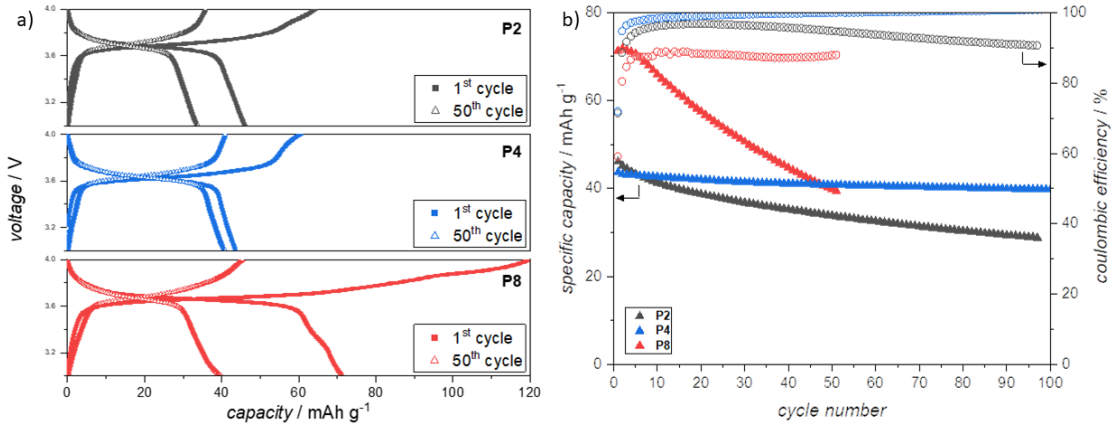

Fig. 5.21 Galvanostatic cycling of the SQX polymers P2, P4 and P8. a) Voltage profiles of the first and 50th discharge cycles from the polymers P2 (black), P4 (blue) and P8 (red). b) Specific capacities (left y-axis, filled out data points) and coulombic efficiencies (right y-axis, hollow data points) of the polymers over up to 100 cycles.

in galvanostatic cycling is shown in Fig. 5.21. From comparison of the voltage profiles of the first and 50th cycles (depicted in Fig. 5.21 a) it could be noted that P8 showed the most drastic loss of capacity over 50 cycles. In the part of the charged voltage profile, P8 (red) showed in the first cycle a high capacity at voltage values higher than 3.8 V, which could correspond to the irreversible oxidation observed in CV at these values. On the other hand, the charged capacity of P2 and P4 above 3.8 V vs. Li/Li^+ was not as significant as for P8. In the part of the discharge voltage profile, the capacities of P2, P4 and P8 were mainly contributed by the redox plateau, in average 3.63 V, 3.60 V and 3.61 V, respectively, which was also consistent with the CV results. Additionally, the voltage profiles at the 50th cycles showed that the capacity was still contributed by the SQX polymers. Regarding the cycling performance, the SQX polymer P8 showed the highest initial specific capacity, 71.3 $\mathrm{mA\,h\,g^{-1}}$, which was close to its theoretical capacity, 78.6 $\mathrm{mA\,h\,g^{-1}}$ (calculated with equation 4.1), although it quickly faded to 40 $\mathrm{mA\,h\,g^{-1}}$

in the next 50 cycles with Coulombic efficiencies lower than 90 % (see Table 5.3 and Fig. 5.21). The fast deterioration of P8s capacity seemed to be consistent with the CV in Fig. 5.20 which also showed a rather rapid decrease in the responding current after each cycle. P2 showed the second highest initial capacity at 46.1 $\mathrm{mA\,h\,g^{-1}}$. While this value was already much lower than the calculated theoretical capacity (77.7 $\mathrm{mA\,h\,g^{-1}}$), the Coulombic efficiency compared to P8 was overall improved to more than 90 % and the capacity faded much slower over time. Despite this, the capacity of P2 after 50 cycles was still lower than the capacity of P8 due to the big difference in initial values (Table 5.3). On the other hand, although P4 showed the lowest initial specific capacity out of the three tested polymers, it displayed the highest Coulombic efficiency and 93 % of the initial capacity was maintained over 50 cycles and even 91 % over 100 cycles. This result was interesting as P4 outperformed P2 and P8 after seven and 48 cycles, respectively, even though it initially had the lowest value. The high cyclability of P4 shows that it would be promising as a potential cathode material.

Table 5.3 Electrochemical properties of selected SQX polymers in LP-30. The redox potentials were referenced against Li/Li^+.

polymer	**$E_{1/2}$ / V**	**theo. capacity** / $\mathrm{mA\,h\,g^{-1}}$	**spec. capacity 1^{st} cycle** / $\mathrm{mA\,h\,g^{-1}}$	**spec. capacity 50^{th} cycle** / $\mathrm{mA\,h\,g^{-1}}$
P2	3.69	77.7	46.1	33.8
P4	3.63	66.8	43.7	40.8
P8	3.66	78.6	71.3	39.9

In conclusion, the Li half-cell testing of the SQX polymers showed that all of them maintained their redoxactivity in LP-30. The CVs showed the appearance of two irreversible oxidations at around 3.9 V and above 4.0 V vs. Li/Li^+, respectively. While the first oxidation would disappear after the first cycle, the second, less pronounced oxidation remained throughout three CV cycles. By addition of graphene as a second conductive matrix to the electrode, the oxidation at 3.9 V could be alleviated but at the same time, the second oxidation was intensified. For the polymer P6 this second oxidation negatively influenced the reversibility of the main redox event at 3.65 V. After limiting the CVs upper potential range to 4.0 V, the redox reaction became fully reversible again. To avoid a similar effect during the galvanostatic cycling tests, the cut-off voltages were set to

3.0 V and 4.0 V vs. Li/Li^+. The cycling of the polymers P2, P4 and P8 revealed that the initial capacities were much lower from their calculated theoretical values. While P8 showed the highest capacity in the first cycle (90.7 % of the theor. capacity), it quickly faded to 50.8 % after 50 cycles. P2s specific capacity after 50 cycles was even lower (43.5 % of the theo. capacity) but overall faded slower than P8 as the initial value was already at only 59.3 % of the calculated one. Interestingly, P4 started off with the lowest capacity (theoretical as well as initial value) but showed high coulombic efficiency, retaining 93.4 % of the initial capacity after 50 cycles and 91.1 % after 100 cycles (39.8 $\mathrm{mA\,h\,g^{-1}}$ corresponding to 61.1 % and 59.6 % of the theoretical capacity, respectively). This high cyclability of P4 in a rather simple testing environment without any optimized parameters is a promising result for the perspective of SQX polymers as electrode materials. The performance of P4 can be regarded as a proof of concept to show the potential and capability of the class of SQX based redox polymers as new organic cathode materials.

6 Summary and Conclusion

In the context of this work, the synthesis and characterization of new polymers based on the smallest cyclic redox-active moieties, namely the amino cyclopropenium cations (ACPs) and the squaric acid amides (SAAs) was targeted. While in section 3.1 the successful synthesis of ACP containing polymer AC6 could be verified by two-dimensional solid-state NMR, the redoxactivity in solution was not living up to the expectation. While the tested ACP molecules EBA- and Pr2-ACP displayed very reversible oxidations at high potentials in acetonitrile (up to $E_{1/2}$= 1.34 V vs. Ag/Ag^+), the synthesized network AC6 didn't show any reversibility in the same conditions. From cyclic voltammetry (CV), it was shown that AC6 still exhibited an oxidation at 0.92 V vs. Fc/Fc^+ but the corresponding reduction peak was strongly shifted to lower potentials by more than 0.8 V. This result suggested that the ACP moieties inside of the polymeric network were able to delocalize positive charge effectively and stabilize the whole system so well that the electrochemical reduction was unfavored and had to occur at much lower potentials. On top of this, all AC networks appeared to be very hygroscopic, which will be a disadvantageous property for potential applications like energy storage.

Much more promising results were obtained in regard to the squaric acid amides (SAAs) (see chapter 4). The potential of this functional groups as redox-active materials for battery applications was demonstrated on the example of 2,5-diphenyl-2,5-diazabicyclo[4.2.0]oct-1(6)-ene-7,8-dione (DDD) (section 4.1). This cyclic SAA was synthesized in one-step and showed exceptionally high thermal stability with a decomposition temperature T_d of 315 °C and high crystallinity confirmed by differential scanning calorimetry (DSC) and single crystal diffraction. In solution CV, DDD showed reversible oxidation at 0.72 V vs. Fc/Fc^+ in DMF. The CVs in Li half-cells in common carbonate electrolytes (ethylene carbonate (EC) and dimethyl carbonate (DMC)) in different Li salts showed an interesting redox behavior of DDD with the evolution of very sharp redox peaks after the first oxidation in certain electrolytes. This unusual evolution was

interpreted as an activation step to homogenize the active sites on the cathode surface. The effect of different electrolyte compositions onto the performance of DDD was thoroughly investigated and it could be demonstrated by that DDD was stable over 100 cycles under optimized conditions. One factor that was strongly influencing the performance of DDD was its high solubility in the carbonate electrolytes.

To counter this solubility issue, two SAA polymers, SA1 and SA2 were successfully synthesized. Both polymers showed high thermal stability with T_ds = 180 °C and 210 °C, respectively. Even though the thermal stabilities of SA1 and SA2 were not as high as DDDs, the decomposition temperatures were well above 100 °C which was beneficial for electrode preparation. The redoxactivity of both polymers was measured *via* CV in DCM and DMF. SA1s oxidation was in the range of DDD (E^{ox} = 0.72 V vs. Fc/Fc^+) but didn't show any reversibility in either solvent. Instead a significant decrease of the responding current was observed after the first CV cycle. SA2 on the other hand, showed a reversible redox reaction at 0.62 V vs. Fc/Fc^+ at different scan rates. The redox potential was slightly lower than the potential of DDD and the CV in carbonate electrolytes (LP-30, EC:DMC 5:5 wt %) in a Li half-cell over 4 cycles showed that the redoxactivity remained. An evolution of sharp redox peaks like in DDD was not observed for SA2, instead the form of the redox signal indicated reduced diffusion as expected for electrode attached analytes. Interestingly, the oxidation peak around 3.93 V vs. Li/Li^+ was slightly shifted after the first cycle (to 3.96 V vs. Li/Li^+). This shift indicated an activation step after the first oxidation, similar to DDD. Another observed similarity was the rather rapid decrease in the specific current after each CV cycle, pointing to possible dissolution of SA2 in the electrolyte. Therefore, a different electrolyte composition would be necessary to enable stable cycling.

Attempts to polymerize asymmetric squaric acid ester acrylamides and acrylates, as well as main chain polycondensates, unfortunately were not successful (see 4.2.1 and 4.2.3).

Lastly, a special class of squaric acid amides, the squaric acid quinoxalines (SQXs), were rediscovered and a selected number of molecules was synthesized and analysed thermally and electrochemically (see 5.1). The synthesis of the main unit SQX-H, was a straightforward condensation of squaric acid with *o*-phenylenediamine. Similar to DDD, decomposition temperatures of the SQX molecules was very high between 277 °C and 338 °C. Only the isopropyl-substituted SQX molecules S2 and S3 showed lower T_ds

around 220 °C (see Fig. 5.6). Interestingly, these groups also influenced the redox properties of S2 and S3 significantly. While all SQX molecules (except for SQX-H) showed reversible oxidation around 0.30 V, the potentials of S2 and S3 were enhanced (0.36 V vs. Fc/Fc^+). Remarkably, the second isopropyl group in S3 didn't elevate its redox potential in comparison to S2. From these results it was established that the SQX moiety showed promising characteristics for redox-active materials.

Due to the symmetric structure of SQX-H, polycondensation with three different linkers were attempted to obtain main-chain SQX polymers. It was observed that the polycondensation with n-alkyl linkers didn't result in full conversion and long polymer chains. Only the polycondensation with dibromo-*p*-xylene resulted in almost full conversion according to size-exclusion chromatography (SEC) (Fig. 5.10). The resulting polymer PC showed a slightly lower T_d than the SQX molecules with 213 °C and a high glass transition temperature T_g at 95 °C. From CV in acetonitrile it was shown that the redox activity of the SQX moiety remained intact and even showed a higher redox potential than in the small molecules ($E_{1/2}$ = 0.45 V vs. Fc/Fc^+).

To synthesize SQX functionalized homopolymers, eight different SQX monomers with different polymerizable units and linker lengths were synthesized (see 5.1). From these monomers, 6 SQX homopolymers, P2 - P8, were successfully polymerized and analyzed (see 5.3). Similar to their respective monomers, all SQX polymers were brightly colored (yellow, orange or red) and showed high thermal stability according with decomposition temperatures well above 200 °C (except for T_d(P4) = 211 °C). From the TGA results no correlation between the stabilities and nature of the polymeric structures could be found. It could be concluded that the high thermal stability was mainly dictated by the presence of SQX moieties. On the other hand, the glass transition temperatures were heavily dictated by the nature of the polymerizable units, linkers lengths and type of substituent on the SQX moiety. All T_g values were in accordance to the expected literature values with appropriate deviations in respect to their structures. Apart from the thermal properties, the CV measurements in solution showed that all polymers exhibited reversible oxidations over three cycles. Interestingly, P8 showed an additional irreversible oxidation peak for scan rates lower than 300 $\mathrm{mV\,s^{-1}}$ at 0.44 V vs. Fc/Fc^+ that was not observed for any other polymer. More curiously, this oxidation also appeared at a scan rate of 350 $\mathrm{mV\,s^{-1}}$ after the first cycle, while simultaneously the current of the redox reaction declines. This observation indicated that this signal might result from a side product

generated after the first oxidation. In DMF the second oxidation didn't occur and the overall shape of the redox reaction was much more reversible.

The redox properties of the SQX polymers were tested in Li half-cells to examine their suitability for battery applications (see 5.3.1). The cathodes were fabricated by mixing the polymers with conductive carbon (SC-65) and polyvinylidene flouride (PVDF). LP-30 (1 M $LiPF_6$ in 5:5 wt-% EC:DMC) was used as the electrolyte. Each polymer showed reversible oxidation between 3.63 V and 3.73 V vs. Li/Li^+. In the CVs, two additional irreversible oxidations were apparent, the first one occured at around 3.9 V and the second one above 4.1 V vs. Li/Li^+. While the second oxidation stayed visible throughout the CV measurements, the first oxidation disappeared after the first cycles (except in P3). This irreversible oxidation appeared very prominent in P8, where the specific current in the first CV cycle was higher than the current of the reversible redox reaction. To suppress this side reaction, graphene was added as a second conductive matrix to the cathode. While the oxidation at 3.9 V was alleviated, the second oxidation above 4.1 V was significantly increased. For galvanostatic cycling, the cut-off voltages were set to 3.0 V and 4.0 V vs. Li/Li^+ to avoid these side reactions. From three selected SQX polymers, the polymer P4 showed the highest cyclability (see Fig. 5.21). Despite P8 showing the highest initial capacity (71.3 $\mathrm{mA\,h\,g^{-1}}$), it was fading very quickly to just 56 % of the initial capacity by the 50th cycle (Table 5.3). P2 showed a better cyclability and retained 73.3 % of its initial capacity after 50 cycles. Since P2s initial capacity was much lower than P8s, P2 overall had the lowest capacity after 50 cycles. P4 outperformed both polymers by retaining 93 % after 50 and 91 % of its capacity (39.8 $\mathrm{mA\,h\,g^{-1}}$) after 100 cycles, respectively. This result was very promising as this exceptional cyclability was achieved without any optimization in a rather simple Li half-cell setup. Additionally, the theoretical capacity of P4 (66.8 $\mathrm{mA\,h\,g^{-1}}$) was not achieved yet, further optimization could provide a high performing cathode material at competitive capacity values. Furthermore, it was shown that the condensation polymer PC displayed an even higher redox potential in solution that was not examined in Li half-cells yet. This polymer could also show promising results.

Apart from the specific application in batteries, SQX polymers could be interesting for any application of redox-active organic materials (ROMs). Overall, it could be demonstrated that over the course of this work new redox-active polymers based on SAA and

SQX functional groups were successfully synthesized and tested in regard to their redox-activity. All polymers were analysed (key characteristics in IR pointed out for simple identification) and showed high thermal stability and good processability. On top of this, the SQX unit can be synthesized by simple condensation which could be an important factor for accessibility and applicability. Due to these findings, it can be noted that the results outlined in this work will be beneficial for future research in the area of SQX-containing materials and functional polymers.

7 Experimental section

7.1 Material and methods

All chemicals were used as purchased (abcr, Sigma Aldrich, Thermo Scientific, VWR) if not noted otherwise. Polymerizations were carried out in a nitrogen atmosphere and the reaction solutions were degassed with three freeze-pump-thaw-cycles.

7.1.1 Instrumentations

Nuclear magnetic resonance (NMR) spectra were recorded on a BRUKER Ascend 400 NMR spectrometer at ambient temperatures in deuterated solvents. All spectra were referenced to their residual solvent signals (chloroform-d, chemical shifts (δ): ^{1}H-NMR = 7.26 ppm, ^{13}C-NMR = 77.16 ppm; dimethylsulfoxide-d6, chemical shifts (δ): ^{1}H-NMR = 2.50 ppm; ^{13}C-NMR = 39.52 ppm).[147]
Size exclusion chromatography (SEC) was performed in dimethylacetamide (DMAc) on a PSS Polymer Standards Service SECcurity GPC system equipped with three Agilent PLgel 5μm Mixed-C columns (7.5 x 300 mm) at an operating temperature of 50 $^{\circ}\mathrm{C}$ and with a flow rate of 0.5 mL min^{-1}. The system was calibrated with polystyrene (PS) and poly(methyl methacrylate) (PMMA) standards ranging from 370 to 2.5 x 10^{6} g mol^{-1} (PS) and 800 to 2.2 x 10^{6} g mol^{-1} (PMMA).
Infrared (IR) spectra were recorded on a BRUKER VERTEX 80 Fourier transform infrared (FTIR) spectrometer equipped with a PIKE MIRacle™ universal attenuated total reflection (ATR) sampling tool with a diamond ATR crystal.
Elemental analysis (EA) was performed with a vario MICRO cube analyzer from Elementar. All thermogravimetric analysis (TGA) was carried out using the TA instruments TGA 5500 analyzer. The analysis was done under nitrogen flow using platinum pans.

Further thermal analytics were performed with the differential scanning calorimeter (DSC) DSC2500 from TA instruments.
The cyclic voltammetry (CV) measurements were carried out on a Metrohm Autolab PGSTAT with a glassy carbon working electrode (WE), a platinum wire counter electrode and an Ag/Ag^+ reference electrode (RE). Ferrocene (Fc/Fc^+) was used as an internal standard to reference all CVs.

7.1.2 General procedures

7.1.2.1 ACP-network synthesis

The diamine (1.5 eq.) was dissolved in DCM (30 mL) with *N,N*-diisopropylethylamine (DIPEA) (5.5 eq.) at 0 °C first before pentachlorocyclopropane (PCCP) (1.0 eq. in 10 mL DCM) is slowly dropped into the solution. After complete addition, the reaction mixture is let to warm up to room temperature and stirred over night. The mixture turned turbid upon addition of PCCP and then orange. For work-up, the organic phase was washed with diluted aqueous HCl solution, diluted $NaHCO_3$ solution, deionized water and then brine. After drying with $MgSO_4$ the organic solvent was removed *in vacuo*.

7.1.2.2 SAA acrylamide monomers

Boc-protection and deprotection of diamines
The diamine (1.0 eq.) was dissolved in dry THF (20 mL) under a nitrogen atmosphere and cooled to 0°CȦfter cooling down, a solution of di-*tert*-butyl dicarbonate (Boc_2O, 1.0 eq.) in dry THF (15 mL) was added dropwise. The mixture was then allowed to reach room temperature and stirred overnight. In the next step the solvent was removed, and the crude was dissolved in ethyl acetate (100 mL) and washed three times with water and brine. The organic phase was dried and concentrated *in vacuo*, affording the product as a white solid, which was used without further purification.

C2H-Boc:
^{1}H-NMR (400 MHz, $CDCl_3$): δ (ppm) = 4.82 - 5.04 (bs, 1H), 3.09 - 3.27 (m, 2H), 2.77

(t, 1H, J = 6.1 Hz), 1.42 (s, 9H), 1.27 - 1.36 (m, 1H).
FT-IR: ν = 3357, 2985, 2933, 1684, 1528, 1278, 1163, 630 cm^{-1}.

C2M-Boc:
^{1}H-NMR (400 MHz, $CDCl_3$): δ (ppm) = 3.23 - 3.36 (bs, 2H), 2.84 (s, 3H), 2.70 (t, 2H, J = 6.9 Hz), 2.42 (s, 2H), 1.77 (s, 1H), 1.42 (s, 9H).
FT-IR: ν = 2976, 1678, 1396, 1118, 876, 761 cm^{-1}.

C3H-Boc:
^{1}H-NMR (400 MHz, $CDCl_3$): δ (ppm) = 4.58 - 5.04 (m, 1H), 3.09 - 3.25 (m, 2H), 2.75 (t, 1H, J = 7.6 Hz), 1.54 - 1.60 (m, 2H), 1.42 (s, 9H).
FT-IR: ν = 3338, 2976, 2928, 1687, 1514, 1363, 1248, 1166, 641 cm^{-1}.

C3M-Boc:
^{1}H-NMR (400 MHz, $CDCl_3$): δ (ppm) = 3.11 - 3.33 (m, 2H), 2.83 (s, 3H), 2.56 (t, 1H, J = 7.7 Hz), 1.93 - 2.02 (m, 1H), 1.64 - 1.77 (m, 2H), 1.44 (s, 9H).
FT-IR: ν = 2973, 2930, 1688, 1480, 1392, 1363, 1158, 771 cm^{-1}.

Acrylamide formation from the Boc-protected diamine

In an oven-dried round-bottom flask, acryloyl chloride (1.2 eq.) was dissolved under nitrogen atmosphere in anhydrous DCM (20 mL). Then the solution was cooled for 30 min using an ice bath, before a mixture of the N-Boc-diamine (1.0 eq.) and TEA (6.5 eq.) dissolved in anhydrous DCM (20 mL) was added dropwise over 3 h. Upon addition, the solution turned yellow. After complete addition, the reaction mixture was allowed to warm up to room temperature and stirred overnight. The crude product was washed with water and brine three times. The organic layers were dried over magnesium sulfate (Mg_2SO_4), filtered, and concentrated *in vacuo*.

C2H-Boc-acryl:
^{1}H-NMR (400 MHz, $CDCl_3$): δ (ppm) = 6.09 - 6.23 (m, 1H), 5.34 - 5.56 (m, 1H), 4.96 - 5.10 (m, 1H), 3.09 - 3.40 (m, 6H), 1.35 (s, 9H).

C2M-Boc-acryl:
^{1}H-NMR (400 MHz, $CDCl_3$): δ (ppm) = 6.48 - 6.68 (m, 1H), 6.20 - 6.42 (m, 1H), 5.61 - 5.77 (m, 1H), 3.45 - 3.62 (m, 2H), 3.31 - 3.44 (m, 2H), 3.00 - 3.13 (m, 3H), 2.84 - 2.92 (m, 3H), 1.45 (s, 9H).

FT-IR: ν = 2975, 2930, 1689, 1394, 1151, 770 cm^{-1}.

C3H-Boc-acryl:

^{1}H-NMR (400 MHz, $CDCl_3$): δ (ppm) = 6.47 - 6.65 (bs, 1H), 6.05 - 6.36 (m, 2H), 5.57 - 5.66 (m, 1H), 4.81 - 5.00 (m, 1H), 3.37 (q, 2H, J = 7.2 Hz), 3.16 (pquin, 3H, J = 7.2 Hz), 1.64 (pquin, 2H, J = 6.3 Hz), 1.43 (s, 9H).

FT-IR: ν = 3311, 2975, 2928, 1690, 1517, 1247, 1167, 648 cm^{-1}.

C3M-Boc-acryl:

FT-IR: ν = 2973, 2932, 1686, 1392, 1148, 771 cm^{-1}.

Deprotection and formation of the ammonium salt

The Boc-protected acrylamide (1.0 eq.) was dissolved in an oven-dried round bottom flask under Argon atmosphere in anhydrous DCM (10 mL). This solution was treated with a mixture of trifluoroacetic acid and anhydrous DCM (10 mL, v:v, 1:1). The solution turned cloudy almost instantly and the reaction mixture was allowed to stir over night at RT. Toluene was added to the yellow crude mxture to remove TFA by azeotropic evaporation *in vacuo*. The remaining oily crude product was dissolved in ethanol (25 mL), filtered, and concentrated *in vacuo* before being subjected to the next reaction step directly after.

Synthesis of the squaric ester acrylamides

Squaric acid diethyl ester (1.1 eq.) and TEA (1.5 eq.) were dissolved in ethanol (20 mL). The ammonium TFA salt (3.1 eq.) was dissolved in ethanol (5 mL) and added dropwise to the reaction mixture over the course of one hour. An initial formation of white precipitate was observed. Over time, the precipitate disappeared and the reaction mixture turned yellow. The reaction was stopped after 6 h and concentrated *in vacuo*. All crude products were purified by column chromatography in silica.

M-C2H:

^{1}H-NMR (400 MHz, DMSO$-d_6$): δ (ppm) = 6.00 - 6.27 (m, 2H), 5.54 - 5.65 (m, 1H), 4.53 - 4.71 (m, 3H), 3.48 - 3.64 (m, 2H), 3.26 - 3.30 (m, 2H), 1.31 - 1.40 (m, 3H).

FT-IR: ν = 3401, 2978, 2700, 1802, 1672, 1601, 1200, 1127, 798, 719 cm^{-1}.

M-C3H:

^{1}H-NMR (400 MHz, DMSO$-d_6$): δ (ppm) = 8.50 - 8.80 (m, 1H), 8.06 - 8.14 (bs, 1H),

6.00 - 6.24 (m, 2H), 5.52 - 5.64 (m, 1H), 4.59 - 4.68 (m, 2H), 3.46 - 3.53 (m, 1H), 3.27 - 3.32 (m, 1H), 3.15 (q, 2H, J = 6.7 Hz), 1.69 (quin, 2H, J = 6.9 Hz), 1.35 (q, 3H, J = 7.3 Hz).
FT-IR: ν = 3270, 2982, 1806, 1731, 1673, 1595, 1198, 1125, 798, 719 cm^{-1}.
M-C3M:
^{1}H-NMR (400 MHz, DMSO−d_6): δ (ppm) = 6.65 - 6.87 (m, 1H), 6.00 - 6.18 (m, 1H), 5.60 - 5.70 (m, 1H), 4.58 - 4.70 (m, 2H), 3.55 - 3.65 (m, 1H), 3.37 - 3.46 (m, 1H), 2.84 - 3.26 (m, 6H), 1.77 - 1.90 (m, 2H), 1.30 - 1.41 (m, 3H).
FT-IR: ν = 2925, 1808, 1675, 1594, 1186, 1133, 799, 719 cm^{-1}.

7.1.3 DDD synthesis

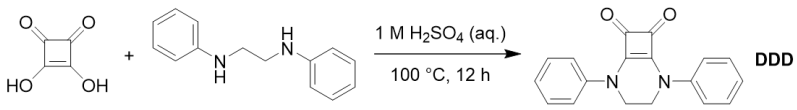

Squaric acid (500 mg, 4.38 mmol, 1.00 eq.) and *N,N'*-diphenylethylene-1,2-diamine (930 mg, 4.38 mmol, 1.00 eq.) were dissolved in an aqueous solution of H_2SO_4 (1M, 25 mL). The mixture was heated to 100 °C and stirred for 12 h. The mixture was allowed to cool down to ambient temperature and the formed precipitate was washed with H_2O (4 x 50 mL) and the washed precipitate was dried under reduced pressure to obtain the product as a colorless powder (940 mg, 3.24 mmol, 74%).
^{1}H-NMR (400 MHz, DMSO−d_6): δ (ppm) = 7.55 – 7.42 (m, 8H), 7.23 – 7.16 (m, 2H), 4.11 (s, 4H) ppm.
^{13}C-NMR (100 MHz, DMSO−d_6): δ (ppm) = 179.6, 165.1, 140.4, 129.2, 124.2, 118.5, 45.3 ppm.
FT-IR: ν = 1784, 1692, 1573, 1483, 1304, 1094, 764, 693 cm^{-1}.
MS(APCI): m/z calculated for $[M + H]^+$ = 291.11, found: 290.4 (83.5 %), 291.1 (16.5 %); Anal. Calcd for $C_{18}H_{14}N_2O_2$ (%): C, 74.47; H, 4.86; N, 9.65. Found (%): C, 73.32; H, 4.46; N, 9.68.

7.1.4 SQX synthesis

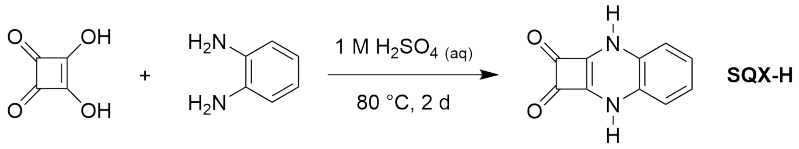

SQX-H: 3,4-Dihydroxy-3-cyclobutene-1,2-dione (squaric acid (SA), 11.5 g, 101 mmol, 1.0 eq.) was mixed with 1,2-diaminobenzene (11.0 g, 101 mmol, 1.0 eq.) in 500 mL of 1 M aqueous sulfuric acidic solution. The reaction mixture was heated to 80 °C and stirred for 2 days. After cooling down, the precipitated solid was collected and washed with deionized water until the filtrate was neutral. The product was dried at 70 °C *in vacuo* overnight and obtained as a dark-red solid (14.7 g, 78.7 mmol, 77 % yield).
^{1}H-NMR (400 MHz, DMSO$-$d$_6$): δ (ppm) = 10.0 (s, 2H), 6.28 – 6.72 (m, 4H).
^{13}C-NMR (100 MHz, DMSO$-$d$_6$): δ (ppm) = 178.2, 174.4, 131.7, 124.9, 116.4.
FT-IR: ν = 3120, 2952, 1788, 1654, 1606, 1553, 1474, 775, 728, 664, 600 cm^{-1}.

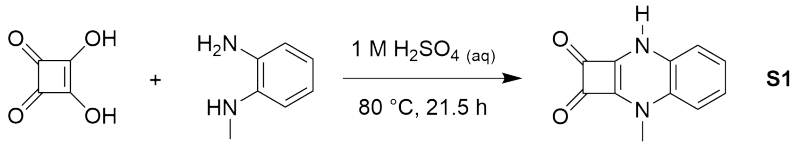

S1: 3,4-Dihydroxy-3-cyclobutene-1,2-dione (SA, 9.34 g, 81.9 mmol, 1.0 eq.) was mixed with 1,2-diaminobenzene (10.0 g, 81.9 mmol, 1.0 eq.) in 500 mL of 1 M aqueous sulfuric acidic solution. The reaction mixture was heated to 80 °C and stirred for 21.5 h. After cooling down, the precipitated solid was collected and washed with deionized water until the filtrate was neutral. The product was dried at 70 °C *in vacuo* overnight and obtained as a dark-brown solid S2 (13.8 g, 68.8 mmol, 84 % yield).
^{1}H-NMR (400 MHz, DMSO$-$d$_6$): δ (ppm) = 10.1 (s, 1H), 6.29 – 6.80 (m, 4H), 2.99 (s, 3H).
^{13}C-NMR (100 MHz, DMSO$-$d$_6$): δ (ppm) = 178.1, 177.3, 174.3, 173.4, 133.5, 132.8, 125.5, 124.7, 115.8, 114.0, 32.7.
FT-IR: ν = 3159, 2955, 1796, 1678, 1563, 1439, 1378, 1299, 765, 639 cm^{-1}.

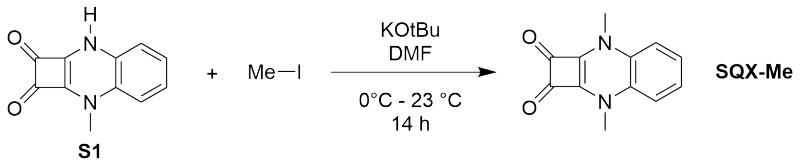

SQX-Me: **S1** (500 mg, 2.50 mmol, 1.0 eq.) was dissolved in 10 mL DMF in an ice bath with potassium tert-butoxide (KOtBu, 420 mg, 3.75 mmol, 1.5 eq.). The mixture turned red and was stirred at 0 °C for additional 25 min before dropwise addition of iodomethane (390 mg, 2.75 mmol, 1.1 eq.) in 10 mL DMF. After complete addition, the ice bath was removed and the mixture was allowed to slowly warm up to room temperature (23 °C) and stirred for 14 h. After the reaction was stopped, the mixture was filtered and the precipitate was thoroughly washed with methanol and dried at 70 °C *in vacuo*. The product was obtained as an orange solid (325 mg, 1.52 mmol, 61 % yield).
^{1}H-NMR (400 MHz, DMSO−d_6): δ (ppm) = 6.83 (dd, 2H, J = 6.2, 3.3 Hz), 6.57 (dd, 4H, J = 6.2, 3.3 Hz), 3.01 (s, 6H).
^{13}C-NMR (100 MHz, DMSO−d_6): δ (ppm) = 178.1, 173.8, 135.0, 125.7, 113.2, 33.3.
FT-IR: ν = 1933, 1799, 1678, 1608, 1564, 1483, 1411, 753, 636 cm^{-1}.

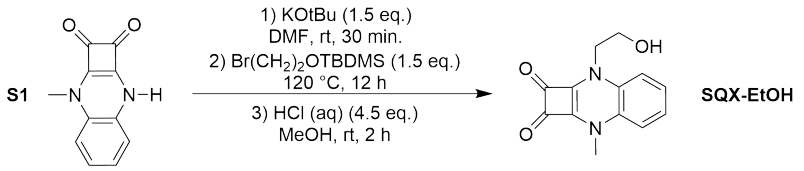

SQX-EtOH: In a sealed tube **S1** (1.00 g, 5.00 mmol, 1.00 eq.) was suspended in anhydrous DMF (10 mL) under argon atmosphere. KOtBu (842 mg, 7.50 mmol, 1.50 eq.) was added to the reaction mixture which changed colors from brown to dark red. The mixture was stirred for 30 minutes and Br(CH_2)$_2$OTBDMS (1.65 mL, 7.50 mmol, 1.50 eq.) was added. The reaction was stirred at 120°C for 12 h after which the TLC showed full conversion. Water (10 mL) was added and the resulting precipitate was filtered of and suspended in MeOH (50 mL) and HCl (18.0 mL in MeOH 1.25 M, 22.5 mmol, 4.50 eq.). After stirring for 2 h at ambient temperature water (50 mL) was added and the mixture was extracted with CH_2Cl_2 (3 x 50 mL). The organic layer was dried over Na_2SO_4 and all volatiles were removed in vacuo. The product was obtained as a yellow

powder (850 mg, 3.49 mmol, 70 % yield).
^{1}H-NMR (400 MHz, DMSO−d_6): δ (ppm) = 6.85 – 6.75 (m, 2H), 6.68 (dd, J = 7.4, 1.9 Hz, 1H), 6.58 (dd, J = 7.3, 2.0 Hz, 1H), 5.07 (s, 1H), 3.60 – 3.51 (m, 4H), 3.02 (s, 3H).
^{13}C-NMR (100 MHz, DMSO−d_6): δ (ppm) = 177.6, 177.1, 174.4, 172.9, 134.7, 133.3, 125.1 (2C), 114.0, 113.9, 56.9, 47.9, 32.9.
FT-IR: ν = 3477, 1798, 1668, 1602, 1564, 1477, 1433, 1409, 1385, 1282, 1203, 1048, 757, 640 cm^{-1}.

SQX-BuOH: In a sealed tube **S1** (500 mg, 2.50 mmol, 1.00 eq.) was suspended in anhydrous DMF (5 mL) under argon atmosphere. KOtBu (336 mg, 3.00 mmol, 1.20 eq.) was added to the reaction mixture which changed colors from brown to dark red. The mixture was stirred for 30 minutes and Br(CH_2)$_4$OTBDMS (0.75 mL, 3.00 mmol, 1.20 eq.) was added. The reaction was stirred at 120°C for 12 h after which the TLC showed full conversion. Water (10 mL) was added and the resulting precipitate was filtered of and suspended in MeOH (50 mL) and HCl (18.0 mL in MeOH 1.25 M, 11.3 mmol, 4.50 eq.). After stirring for 2 h at ambient temperature water (50 mL) was added and the mixture was extracted with CH_2Cl_2 (3 x 50 mL). The organic layer was dried over Na_2SO_4 and all volatiles were removed in vacuo. The product was obtained as a yellow powder (600 mg, 2.20 mmol, 88 % yield).
^{1}H-NMR (400 MHz, DMSO−d_6): δ (ppm) = 6.78 (dd, J = 5.8, 3.4 Hz, 2H), 6.44 (dd, J = 5.8, 3.4 Hz, 1H), 6.39 (dd, J = 5.8, 3.4 Hz, 1H), 3.72 (t, J = 6.0 Hz, 2H), 3.61 (t, J = 6.9 Hz, 2H), 3.12 (s, 3H), 1.86 (s, 1H), 1.82 (p, J = 7.2 Hz, 2H), 1.71 (dt, J = 8.2, 6.0 Hz, 2H).
^{13}C-NMR (100 MHz, DMSO−d_6): δ (ppm) = 178.1, 177.8, 173.9, 173.8, 135.1, 133.7, 125.8, 125.5, 113.7, 113.6, 62.3, 46.0, 33.3, 29.0, 23.9.
FT-IR: ν = 3496, 2954, 1794, 1671, 1606, 1568, 1479, 1440, 1412, 1384, 1231, 1061,

751, 638 cm^{-1}.

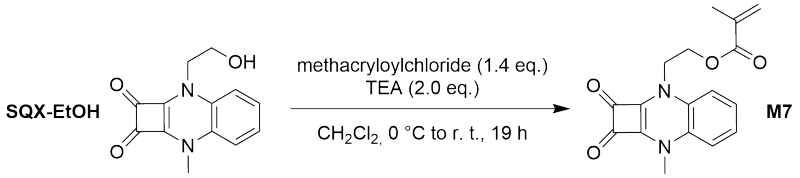

M7: **SQX-EtOH** (302 mg, 1.24 mmol, 1.00 eq.) was dissolved in anhydrous CH2Cl2 and at 0°C triethylamine (TEA, 0.34 mL, 2.46 mmol, 2.00 eq.) and freshly distilled methacrolylchloride (187 mg, 1.79 mmol, 1.44 eq.) were added. The mixture was slowly let to warm up to room temperature and after 19 h, the crude mixture was washed with aq. HCl, aq. $NaHCO_3$, water and brine. After drying the organic phase with $MgSO_4$ and removal of the solvent in vacuo, the product was purified by column chromatography on SiO_2 (eluent; petrol ether) and obtained as an orange yellow solid M7 (381 mg, 1.22 mmol, 99 % yield). ^{1}H-NMR (400 MHz, DMSO$-d_6$): δ (ppm) = 6.75 – 6.88 (m, 3H), 6.57 – 6.64 (m, 1H), 5.99 – 6.03 (m, 1H), 5.64 – 5.69 (m, 1H), 4.29 (t, J = 4.7 Hz, 2H), 3.82 (t, J = 4.7 Hz, 2H), 3.01 (s, 3H), 1.84 (s, 3H).
^{13}C-NMR (100 MHz, DMSO$-d_6$): δ (ppm) = 177.7, 176.8, 173.7, 173.0, 166.3, 135.5, 134.5, 132.8, 126.3, 125.4, 125.3, 114.2, 113.8, 60.4, 44.3, 32.9, 17.9.
FT-IR: ν = 1795, 1717, 1691, 1609, 1573, 1479, 1439, 1411, 1157, 743, 647 cm^{-1}.

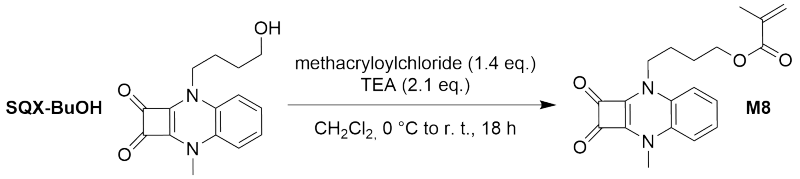

M8: **SQX-BuOH** (950 mg, 3.49 mmol, 1.00 eq.) was dissolved in anhydrous CH_2Cl_2 and at 0°C triethylamine (TEA, 1.02 mL, 7.32 mmol, 2.10 eq.) and freshly distilled methacrolylchloride (461 mg, 4.41 mmol, 1.26 eq.) were added. The mixture was slowly let to warm up to room temperature and after 18 h, the crude mixture was washed with aq. HCl, aq. $NaHCO_3$, water and brine. After drying the organic phase with $MgSO_4$ and removal of the solvent in vacuo, the crude product was purified over

column chromatography on SiO_2 (eluent; ethyl acetate). The product was obtained as a yellow powder M8 (457 mg, 1.34 mmol, 39 % yield). ^{1}H-NMR (400 MHz, DMSO−d_6): δ (ppm) = 6.54 – 6.85 (m, 4H), 5.97 – 6.04 (m, 1H), 5.62 – 5.69 (m, 1H), 4.13 (t, J = 5.95 Hz, 2H), 3.52 (t, J = 5.95 Hz, 2H), 3.00 (s, 3H), 1.83 – 1.88 (m, 3H), 1.64 – 1.77 (m, 4H).
^{13}C-NMR (100 MHz, DMSO−d_6): δ (ppm) = 177.4, 177.0, 173.4, 173.3, 166.5, 135.9, 134.6, 133.1, 125.6, 125.3, 125.2, 114.0, 113.7, 63.6, 44.9, 32.9, 25.1, 23.0, 18.0
FT-IR: ν = 2957, 1792, 1714, 1685, 1607, 1567, 1480, 1437, 1401, 1292, 1161,756, 638 cm^{-1}.

7.1.5 SQX polymers

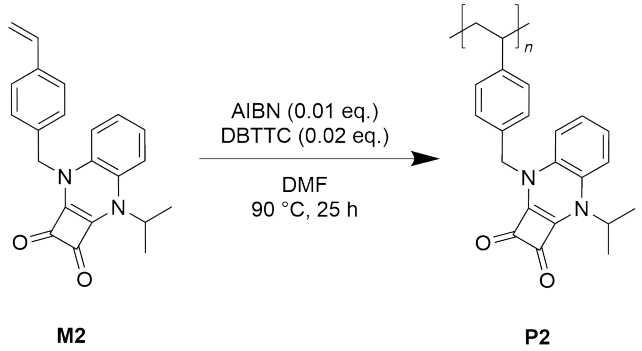

P2: **M2** (800 mg, 2.32 mmol, 1.0 eq.) was dissolved in 3 mL dry DMF with DBTTC (14.7 mg, 0.05 mmol, 0.02 eq.) and AIBN (5.0 mg, 0.03 mmol, 0.01 eq.). After degassing the solution with three freeze-pump-thaw cycles, the polymerization was started at 90 °C and stopped after 25 h by cooling in an ice bath. The polymer was precipitated in cool diethylether (Et_2O) and dried at 40 °C *in vacuo* to obtain a bright orange solid (391 mg, 49 % yield).
^{1}H-NMR (400 MHz, DMSO−d_6): δ (ppm) = 6.11 – 7.42 (m, 8H), 3.90 – 4.84 (m, 3H), 0.99 – 1.57 (m, 9H).
FT-IR: ν = 2929, 1786, 1690, 1605, 1565, 1479, 1420, 1282, 744, 630 cm^{-1}.

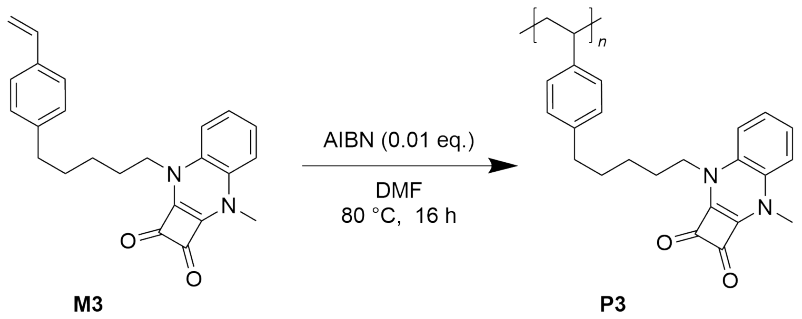

P3: **M3** (312 mg, 0.78 mmol, 1.0 eq.) was dissolved in 2 mL dry DMF with AIBN (1.5 mg, 0.01 mmol, 0.01 eq.). After degassing the solution with three freeze-pump-thaw cycles, the polymerization was started at 80 °C and stopped after 16 h by cooling in an ice bath. The polymer was precipitated in cool diethylether (Et_2O) and dried at 40 °C *in vacuo* to obtain an orange solid (183 mg, 27 % yield).
^{1}H-NMR (400 MHz, DMSO$-d_6$): δ (ppm) = 6.40 – 7.39 (m, 8H), 3.23 – 3.50 (m, 2H), 2.87 - 3.00 (m, 3H), 0.99 – 1.98 (m, 11H).
FT-IR: ν = 2924, 1795, 1690, 1609, 1570, 1479, 746, 638 cm^{-1}.

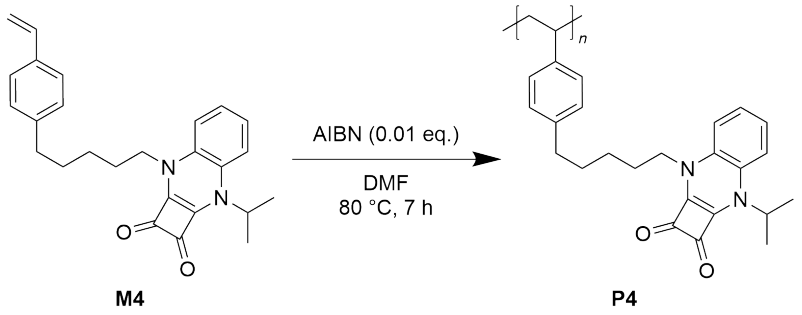

P4: **M4** (550 mg, 1.48 mmol, 1.0 eq.) was dissolved in 2 mL dry DMF with AIBN (2.4 mg, 0.01 mmol, 0.01 eq.). After degassing the solution with three freeze-pump-thaw cycles, the polymerization was started at 80 °C and stopped after 7 h by cooling in an ice bath. The polymer was precipitated in cool diethylether (Et_2O) and dried at 40 °C *in vacuo* to obtain an orange solid (115 mg, 21 % yield).
^{1}H-NMR (400 MHz, DMSO$-d_6$): δ (ppm) = 6.35 – 7.03 (m, 8H), 3.94 – 4.21 (m, 1H), 3.35 – 3.58 (m, 2H), 2.19 - 2.51 (m, 3H), 0.97 – 1.72 (m, 14H).

FT-IR: ν = 2928, 1786, 1690, 1606, 1566, 1480, 1424, 1283, 732, 629 cm^{-1}.

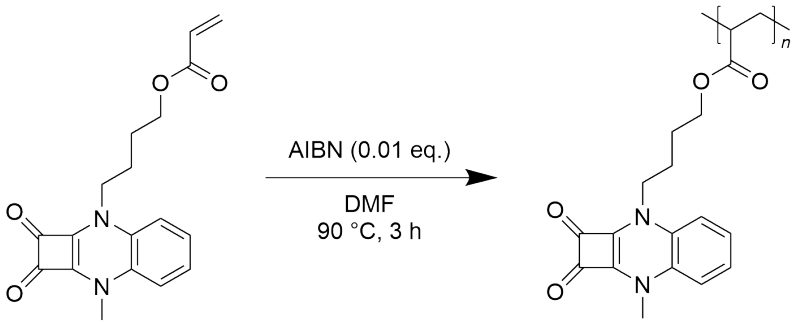

M6 **P6**

P6: **M6** (300 mg, 0.92 mmol, 1.0 eq.) was dissolved in 2 mL dry DMF with AIBN (1.8 mg, 0.01 mmol, 0.01 eq.). After degassing the solution with three freeze-pump-thaw cycles, the polymerization was started at 90 °C and stopped after 3 h by cooling in an ice bath. The polymer was precipitated in cool diethylether (Et_2O) and dried at 40 °C *in vacuo* to obtain a bright orange solid (71.3 mg, 24 % yield).
^{1}H-NMR (400 MHz, DMSO$-d_6$): δ (ppm) = 6.45 – 6.98 (m, 4H), 3.86 – 4.19 (m, 2H), 3.38 – 3.52 (m, 2H), 2.90 – 3.02 (m, 4H), 1.12 – 1.76 (m, 6H).
FT-IR: ν = 2930, 1795, 1728, 1683, 1607, 1568, 1478, 1439, 1406, 1237, 747, 638 cm^{-1}.

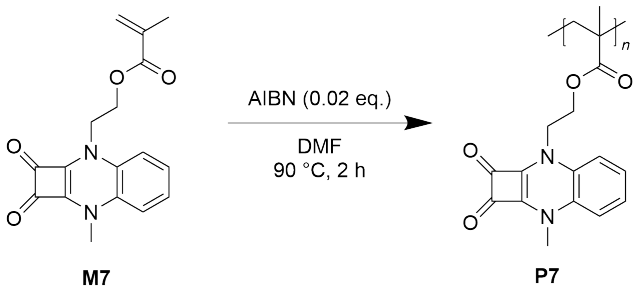

M7 **P7**

P7: **M7** (150 mg, 0.48 mmol, 1.0 eq.) was dissolved in 0.5 mL dry DMF with AIBN (2.0 mg, 0.01 mmol, 0.01 eq.). After degassing the solution with three freeze-pump-thaw cycles, the polymerization was started at 90 °C and stopped after 2 h by cooling in an ice bath. The polymer was precipitated in cool diethylether (Et_2O) and dried at 40 °C

in vacuo to obtain a yellow solid (13 mg, 9 % yield).
^{1}H-NMR (400 MHz, DMSO−d_6): δ (ppm) = 6.49 – 6.94 (m, 4H), 3.61 – 4.13 (m, 4H), 2.92 – 3.11 (m, 3H), 1.42 – 1.85 (m, 2H), 0.61 - 1.07 (m, 3H).
FT-IR: ν = 2930, 1798, 1728, 1689, 1611, 1572, 1481, 1440, 1408, 1242, 750, 639 cm^{-1}.

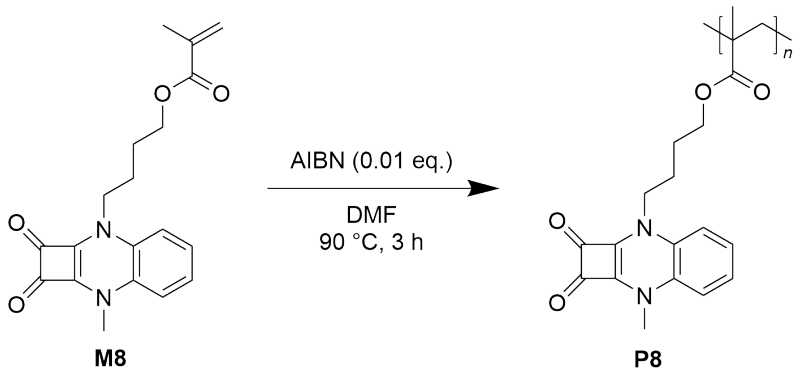

P8: **M8** (410 mg, 1.2 mmol, 1.0 eq.) was dissolved in 2.0 mL dry DMF with AIBN (2.0 mg, 0.01 mmol, 0.01 eq.). After degassing the solution with three freeze-pump-thaw cycles, the polymerization was started at 90 °C and stopped after 3 h by cooling in an ice bath. The polymer was precipitated in cool diethylether (Et_2O) and dried at 40 °C *in vacuo* to obtain a dark orange solid (143 mg, 35 % yield).
^{1}H-NMR (400 MHz, DMSO−d_6): δ (ppm) = 6.49 – 6.88 (m, 4H), 3.76 – 4.00 (m, 2H), 3.36 - 3.51 (m, 2H), 2.90 – 3.00 (m, 3H), 1.53 – 1.72 (m, 6H), 0.64 - 0.98 (m, 3H).
FT-IR: ν = 2939, 1793, 1685, 1609, 1569, 1479, 1439, 1407, 1238, 748, 638 cm^{-1}.

A Appendix

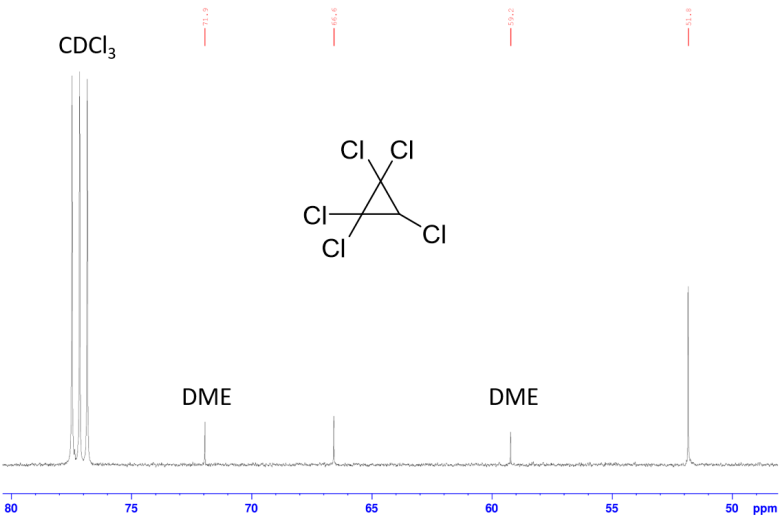

Fig. A.1 ^{13}C-NMR (100 MHz, $CDCl_3$) of pentachlorocyclopropane (PCCP).

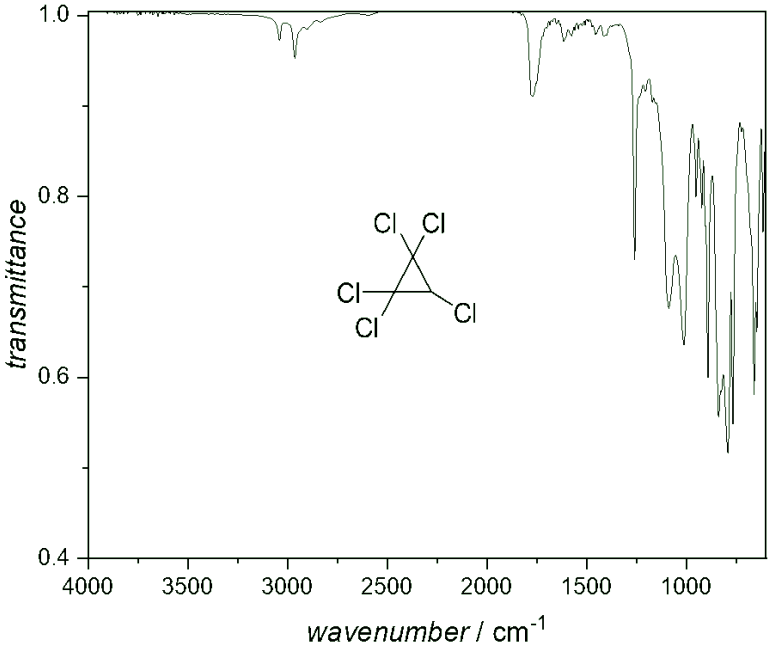

Fig. A.2 FTIR spectrum of PCCP.

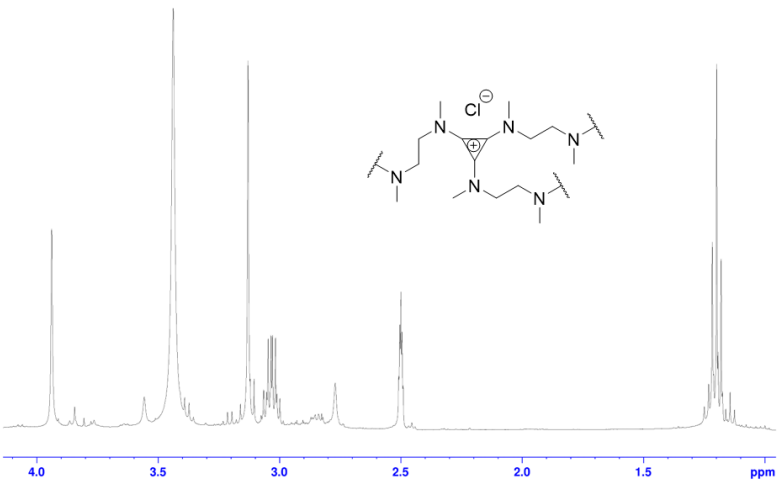

Fig. A.3 ^{1}H-NMR (400 MHz, DMSO) of AC2.

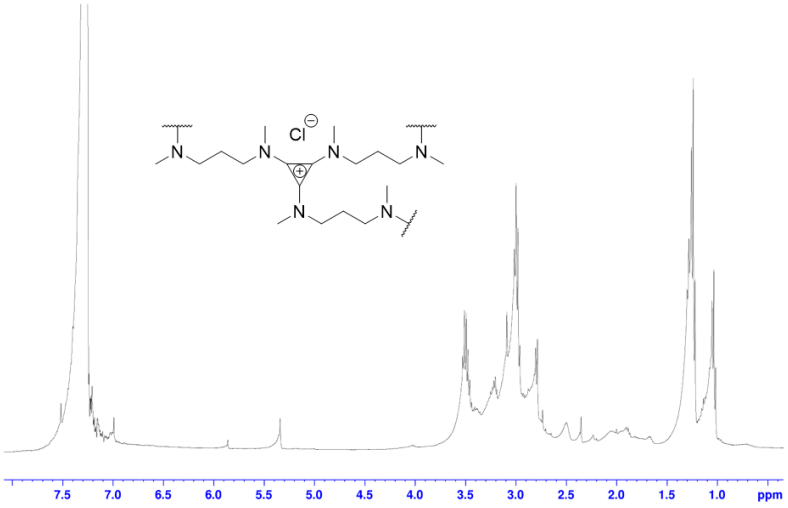

Fig. A.4 ^{1}H-NMR (400 MHz, $CDCl_3$) of AC3.

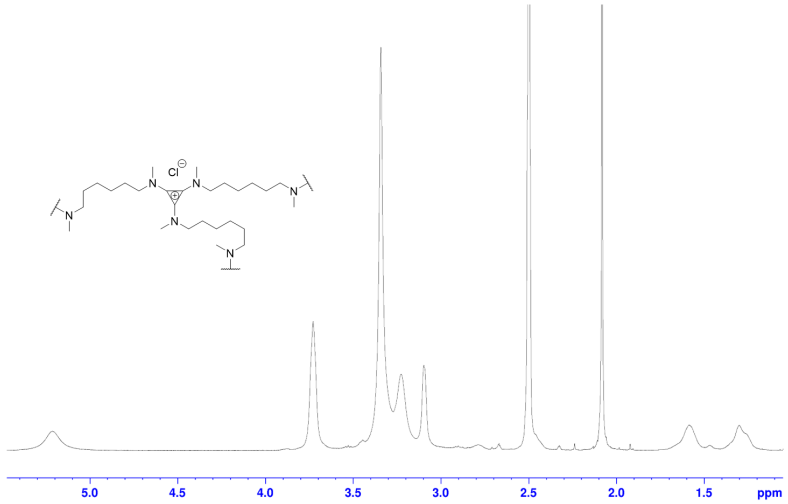

Fig. A.5 ^{1}H-NMR (400 MHz, DMSO) of AC6.

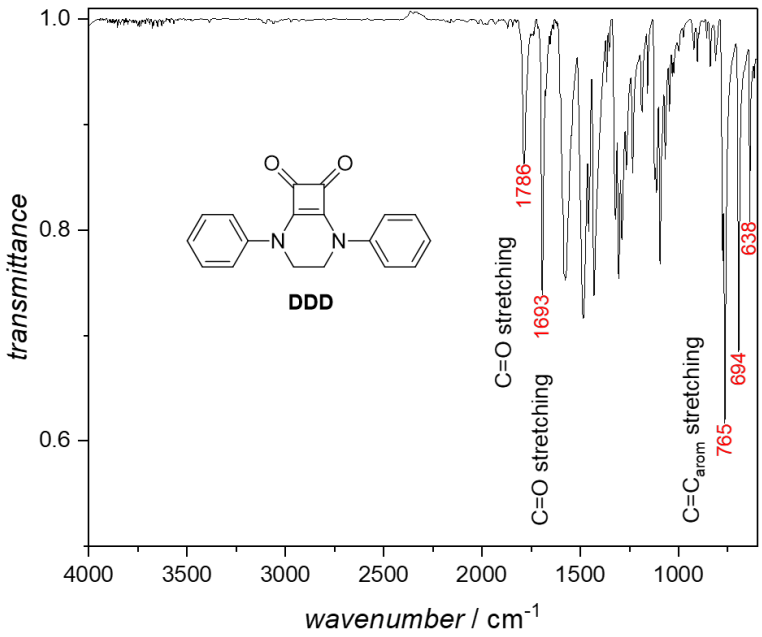

Fig. A.6 FTIR-spectrum of 2,5-diphenyl-2,5-diazabicyclo[4.2.0]oct-1(6)-ene-7,8-dione (DDD).

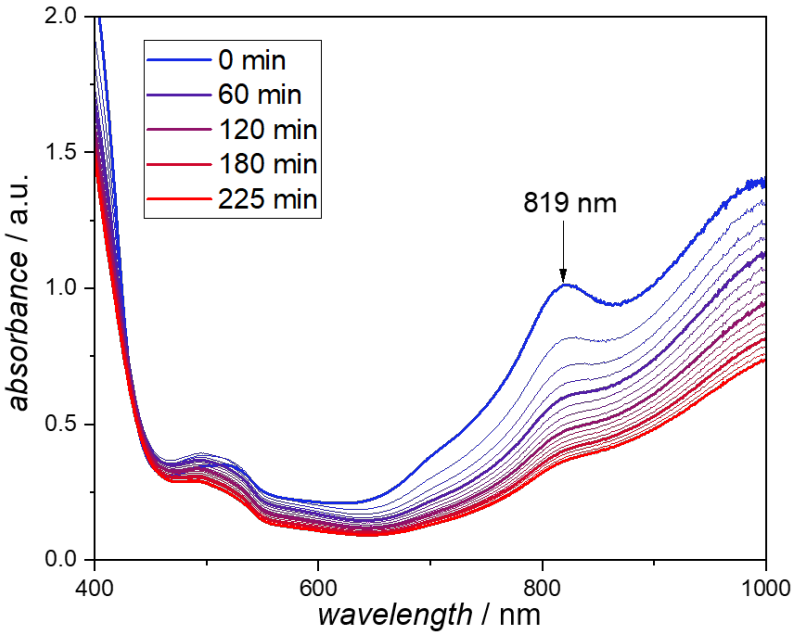

Fig. A.7 UV-Vis spectrum of the radical cation $DDD^{\cdot+}$ over 225 min (measured and plotted by M. E. Baumert at TU Dortmund). The absorption band at 819 nm slowly degraded over time.

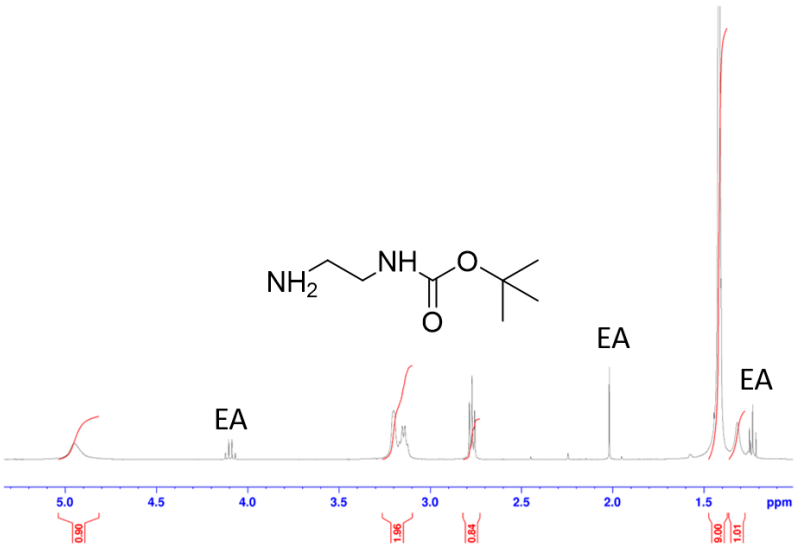

Fig. A.8 ^{1}H-NMR (400 MHz, $CDCl_3$) of C2H-Boc. The ethyl acetate (EA) signals were marked.

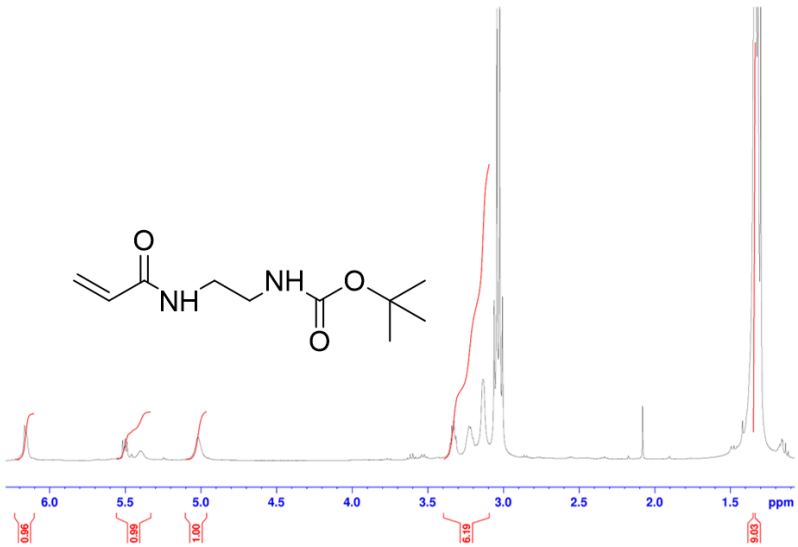

Fig. A.9 ^{1}H-NMR (400 MHz, $CDCl_3$) of C2H-Boc-acrylamide.

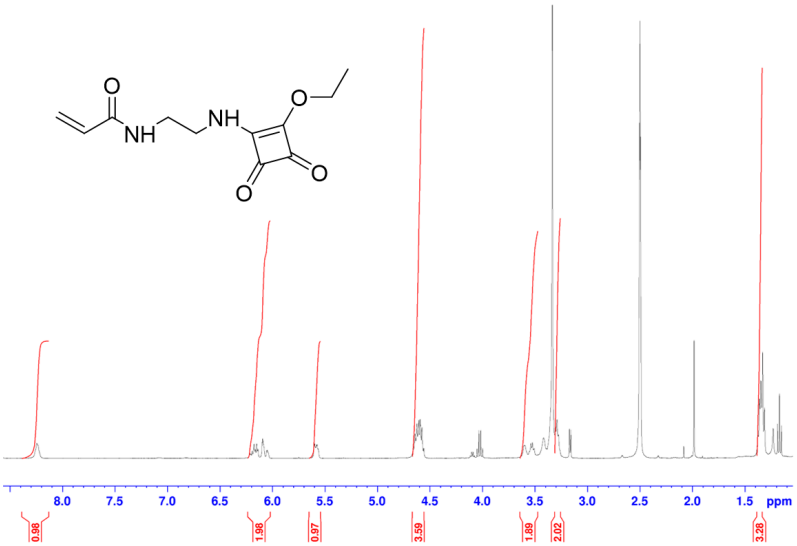

Fig. A.10 ^{1}H-NMR (400 MHz, DMSO) of M-C2H.

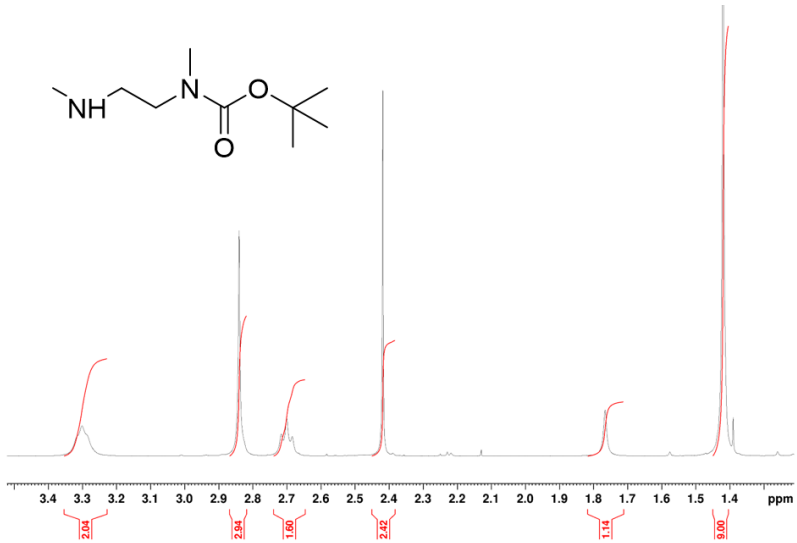

Fig. A.11 ^{1}H-NMR (400 MHz, $CDCl_3$) of C2M-Boc.

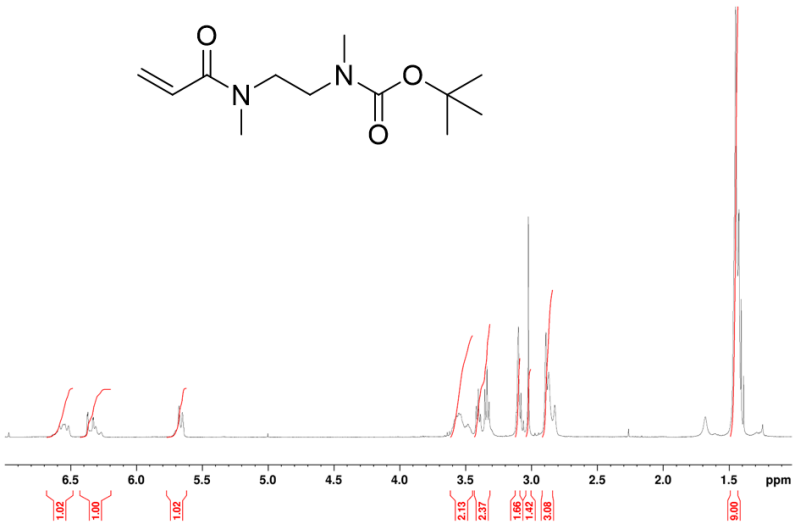

Fig. A.12 ^{1}H-NMR (400 MHz, $CDCl_3$) of C2M-Boc-acrylamide.

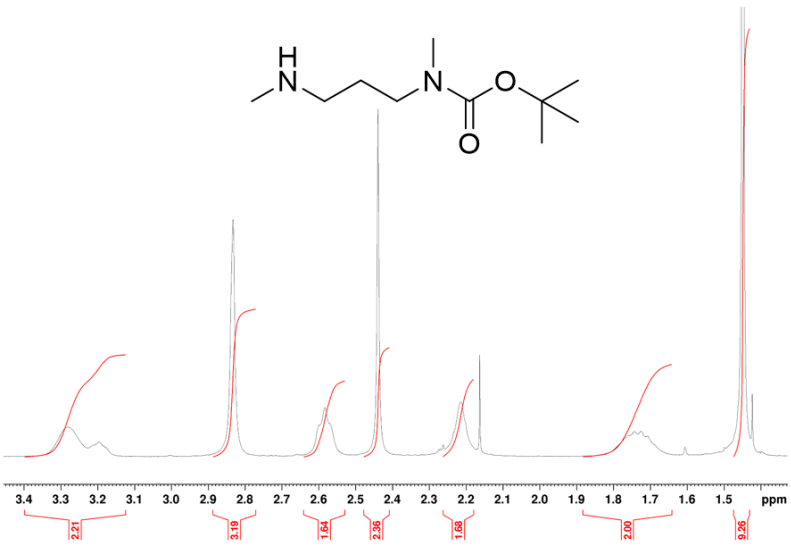

Fig. A.13 ^{1}H-NMR (400 MHz, $CDCl_3$) of C3M-Boc.

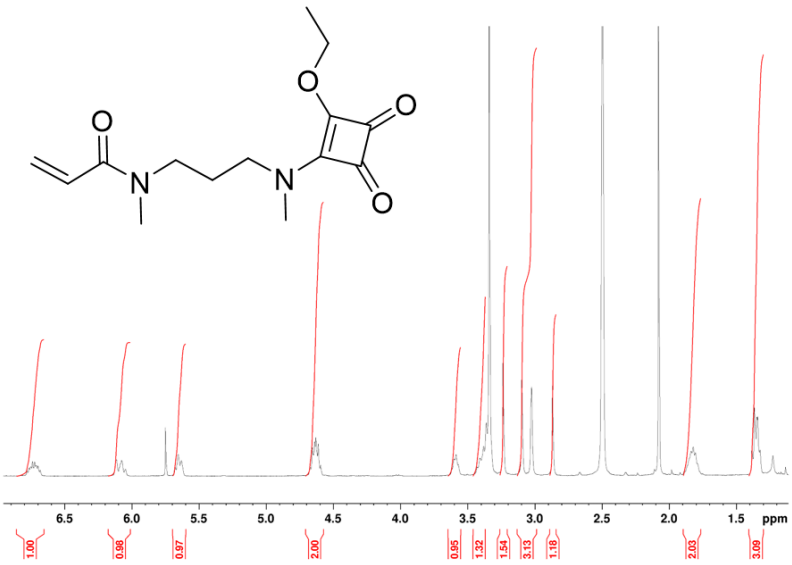

Fig. A.14 ^{1}H-NMR (400 MHz, DMSO) of M-C3M.

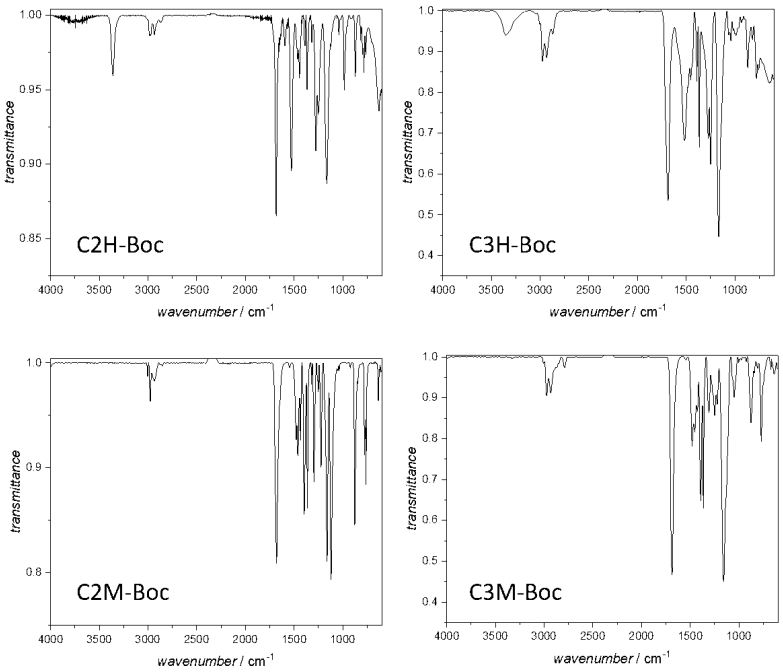

Fig. A.15 FTIR spectra of the Boc-protected diamines C2H to C3M.

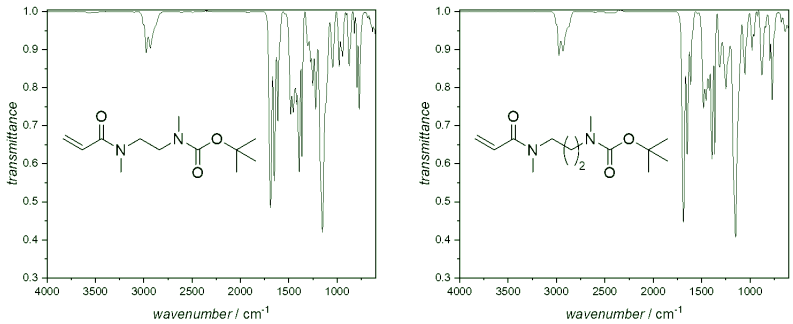

Fig. A.16 FTIR spectra of the Boc-protected acrylamides C2M and C3M.

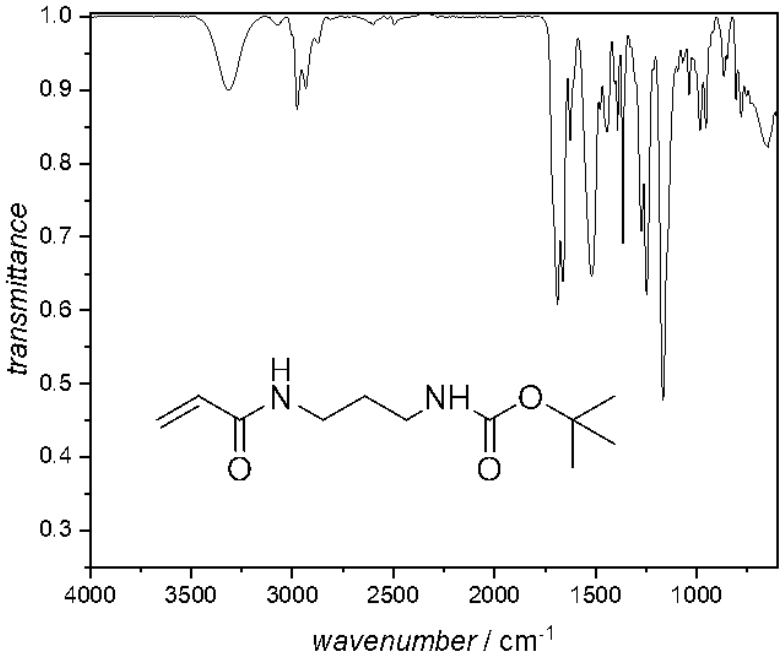

Fig. A.17 FTIR spectra of the Boc-protected acrylamide C3H.

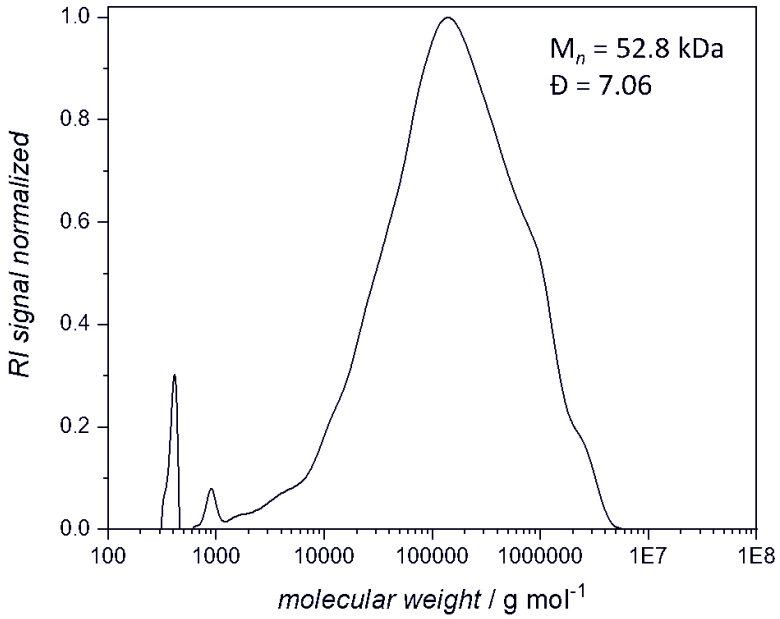

Fig. A.18 SEC trace of the autopolymerization product of M-C2M in dimethylacetamide (DMAc). The SEC was calibrated with PMMA standards.

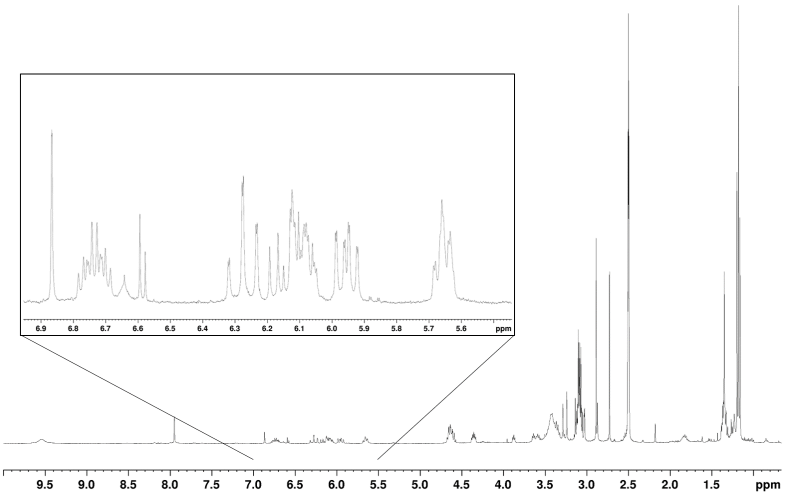

Fig. A.19 ^{1}H-NMR (400 MHz, DMSO) of the copolymerization of M-C3H with A. The signals in the olefinic region showed no conversion of monomer.

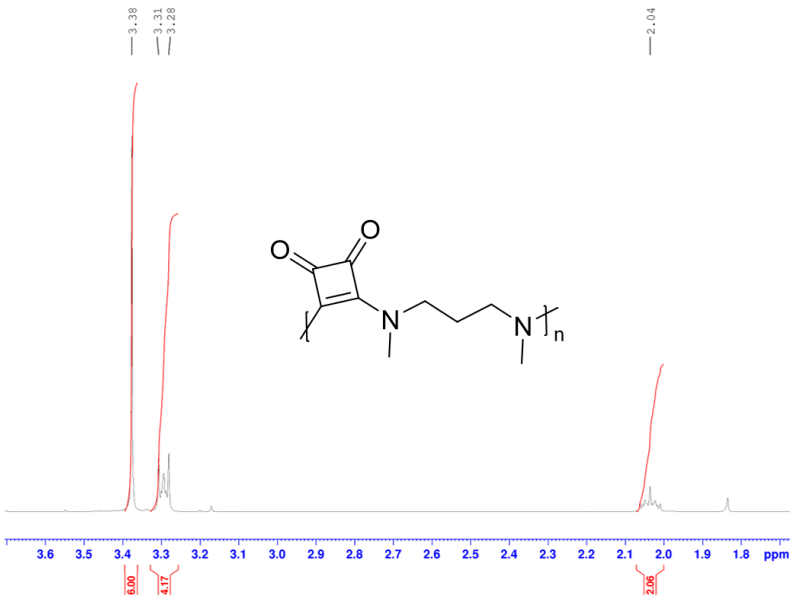

Fig. A.20 ^{1}H-NMR (400 MHz, $CDCl_3$) of the condensation product of squaric acid ethyl ester (SAE) and dimethylpropylene diamine.

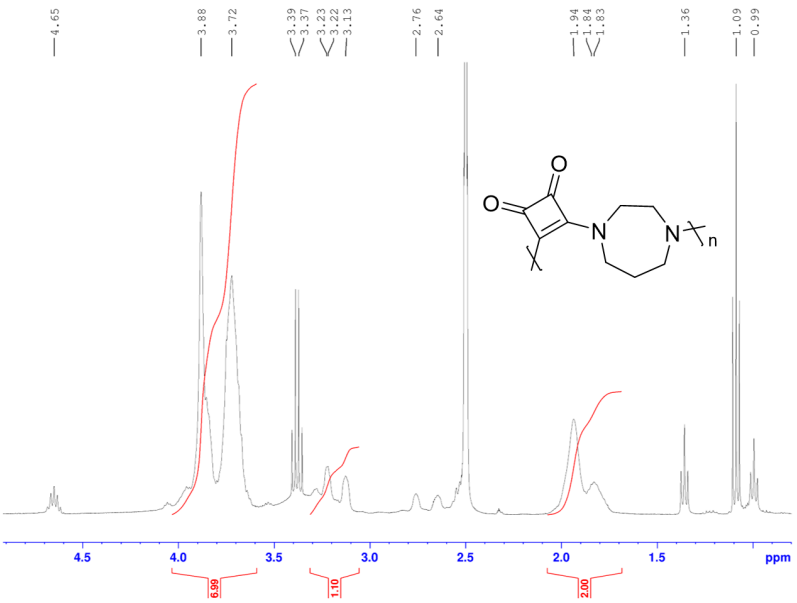

Fig. A.21 ^{1}H-NMR (400 MHz, DMSO) of the condensation product of squaric acid ethyl ester (SAE) and homopiperazine.

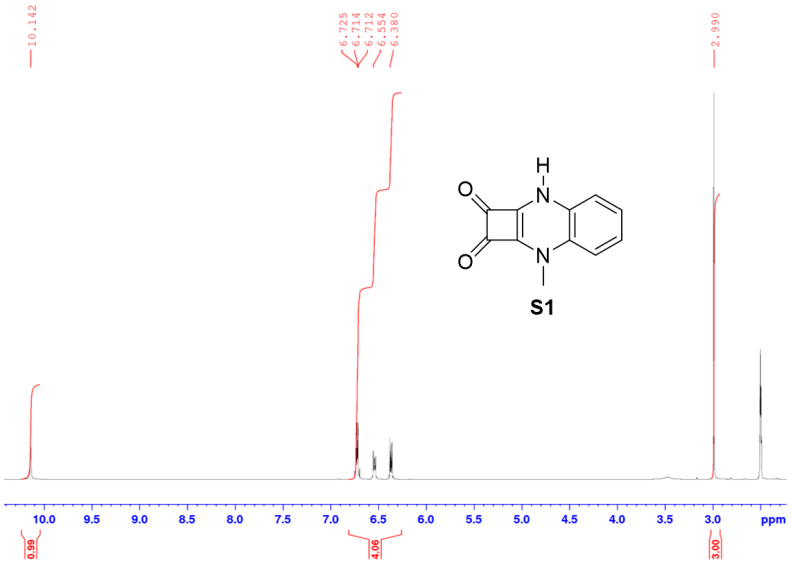

Fig. A.22 [1]H-NMR (400 MHz, DMSO) of S1.

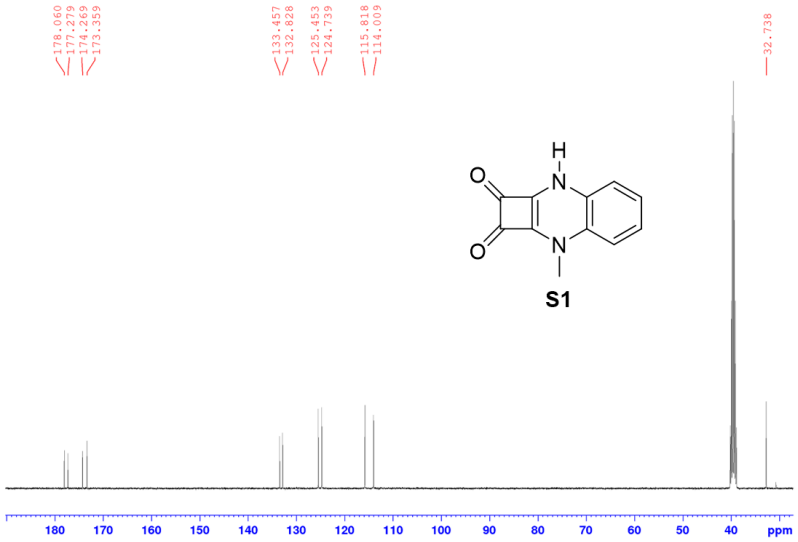

Fig. A.23 [13]C-NMR (100 MHz, DMSO) of S1.

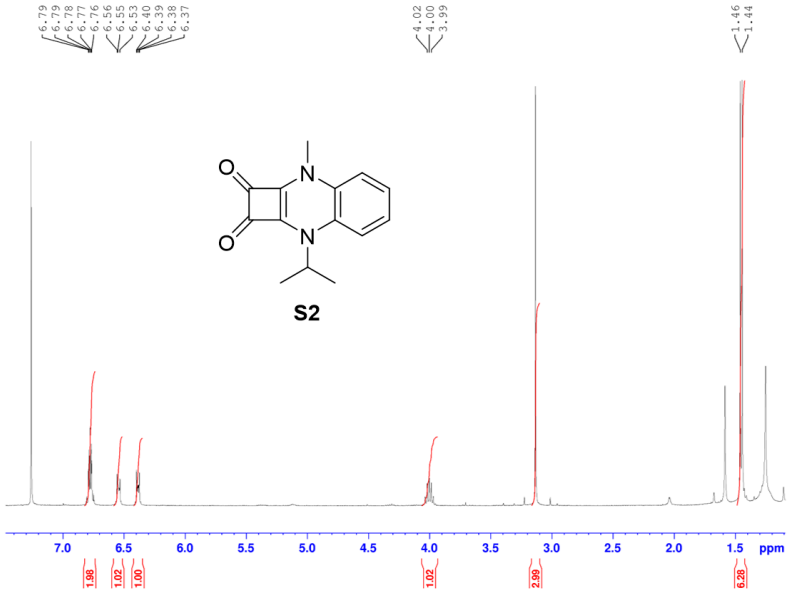

Fig. A.24 ^{1}H-NMR (400 MHz, $CDCl_3$) of S2.

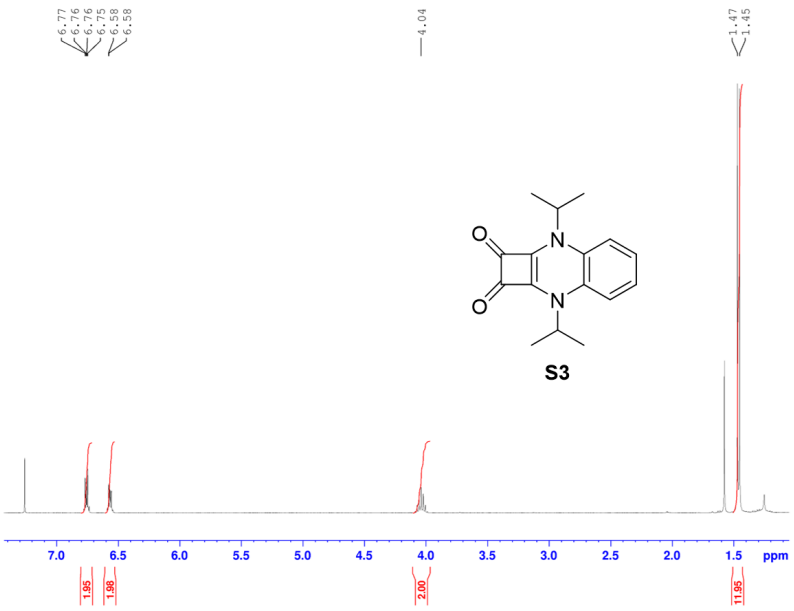

Fig. A.25 ^{1}H-NMR (400 MHz, $CDCl_3$) of S3.

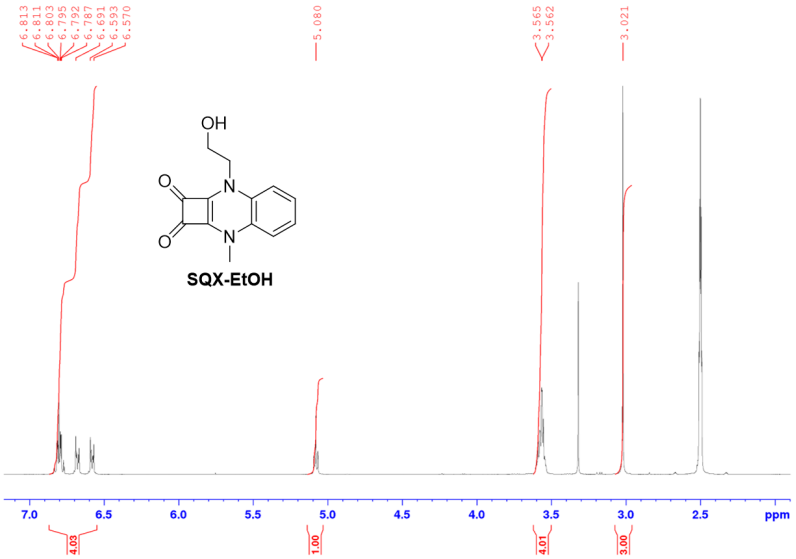

Fig. A.26 ^{1}H-NMR (400 MHz, DMSO) of SQX-EtOH.

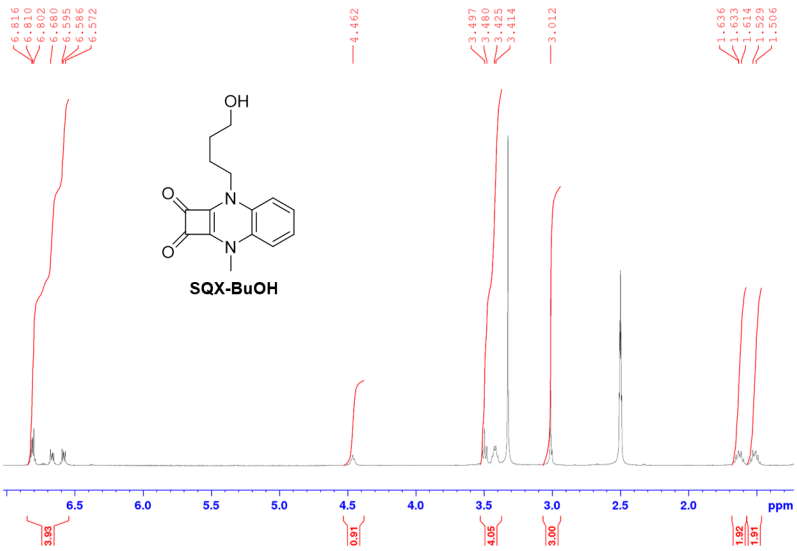

Fig. A.27 ^{1}H-NMR (400 MHz, DMSO) of SQX-BuOH.

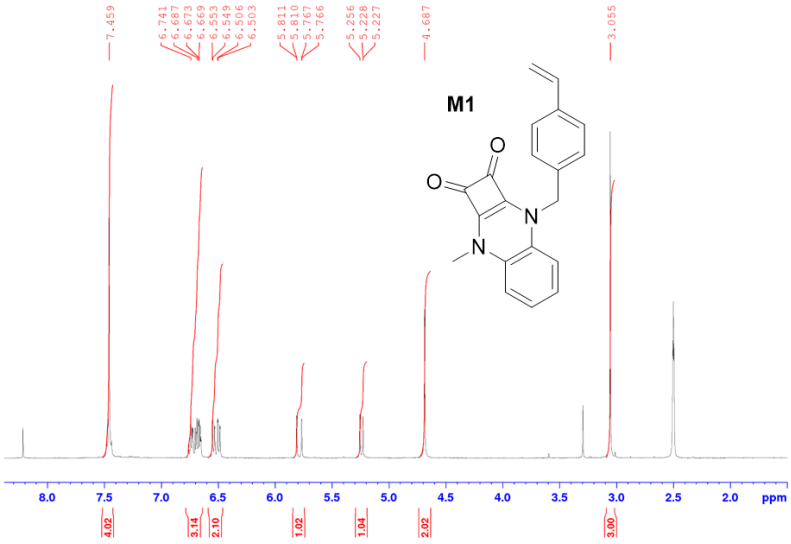

Fig. A.28 ^{1}H-NMR (400 MHz, DMSO) of M1.

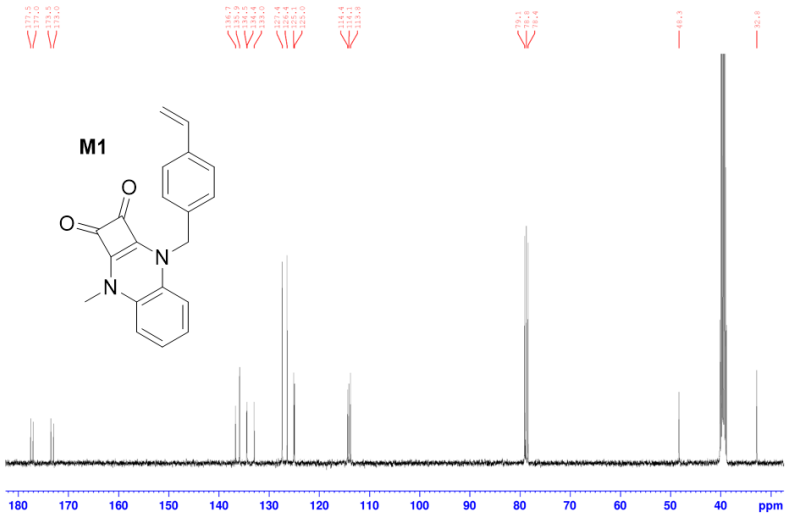

Fig. A.29 ^{13}C-NMR (100 MHz, DMSO) of M1.

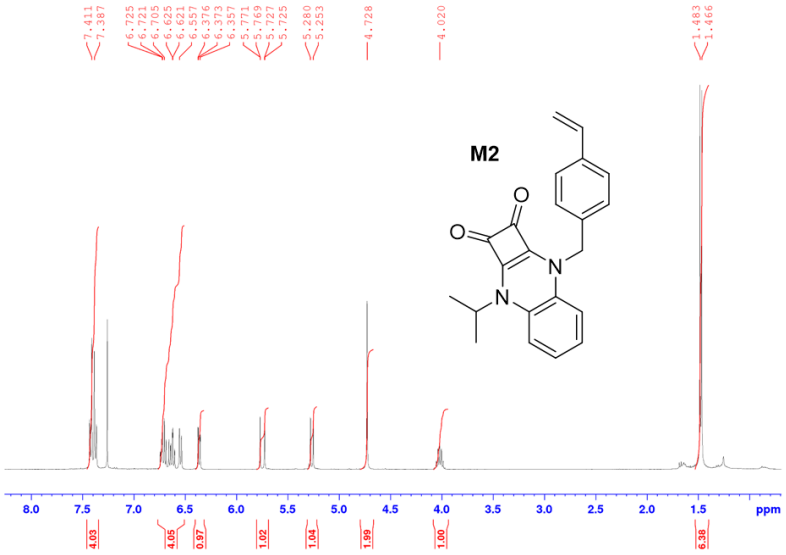

Fig. A.30 ^{1}H-NMR (400 MHz, $CDCl_3$) of M2.

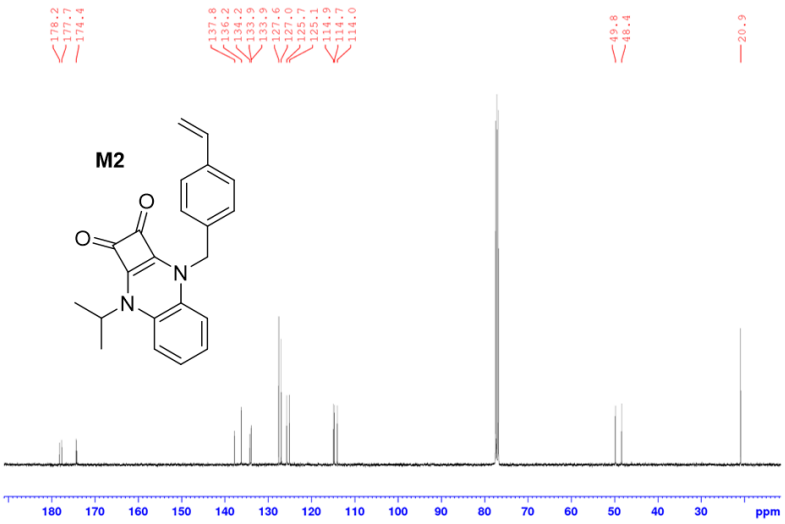

Fig. A.31 ^{13}C-NMR (100 MHz, $CDCl_3$) of M2.

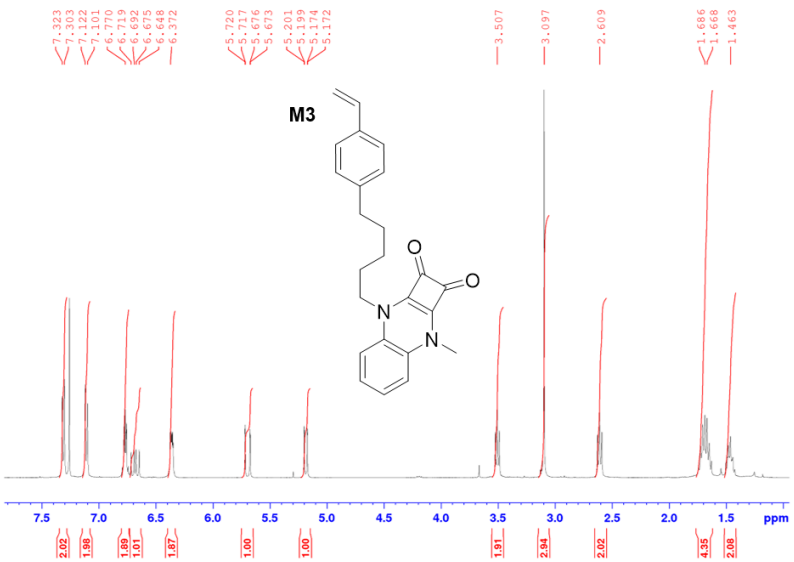

Fig. A.32 ^{1}H-NMR (400 MHz, $CDCl_3$) of M3.

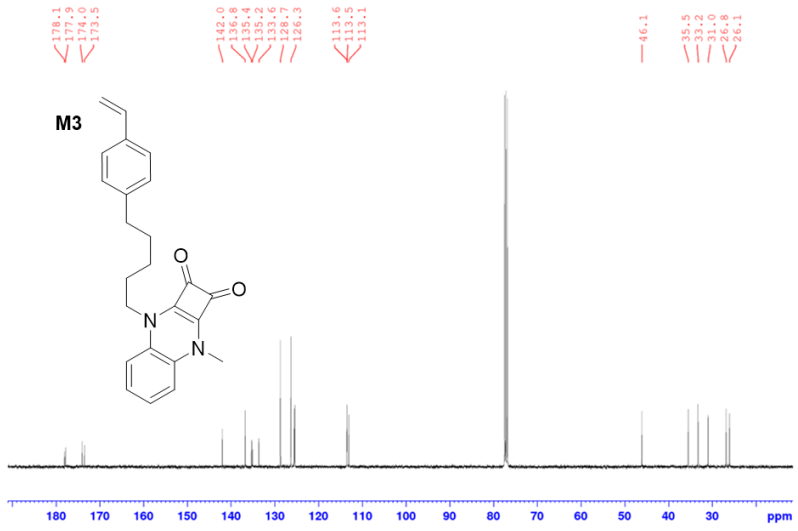

Fig. A.33 ^{13}C-NMR (100 MHz, $CDCl_3$) of M3.

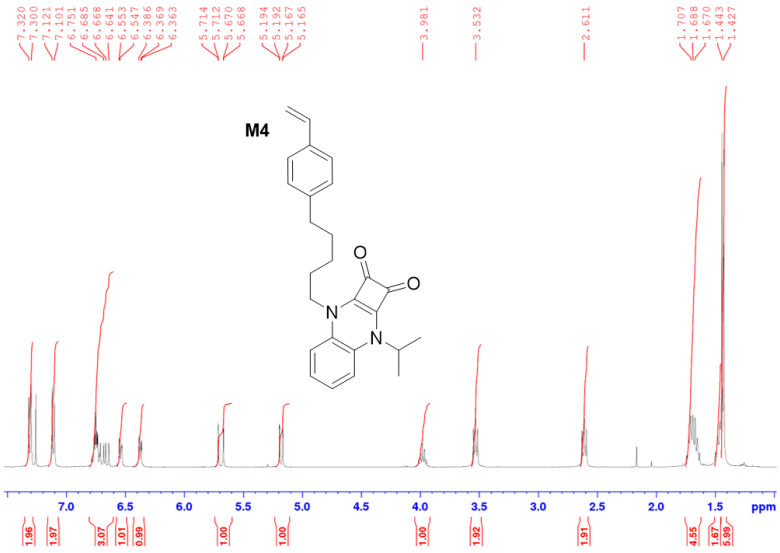

Fig. A.34 ^{1}H-NMR (400 MHz, $CDCl_3$) of M4.

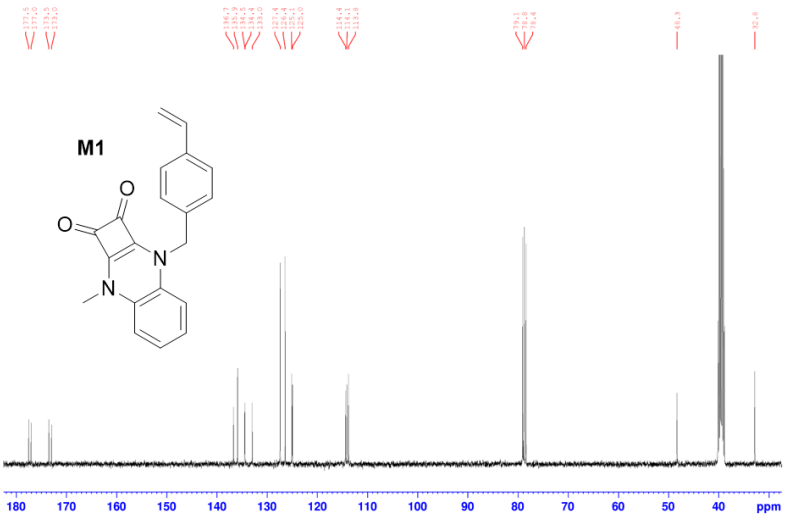

Fig. A.35 ^{13}C-NMR (100 MHz, $CDCl_3$) of M4.

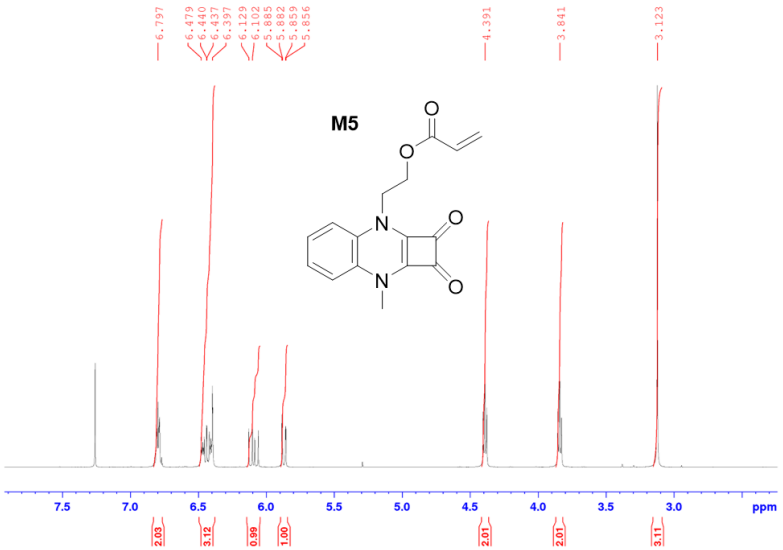

Fig. A.36 ^{1}H-NMR (400 MHz, $CDCl_3$) of M5.

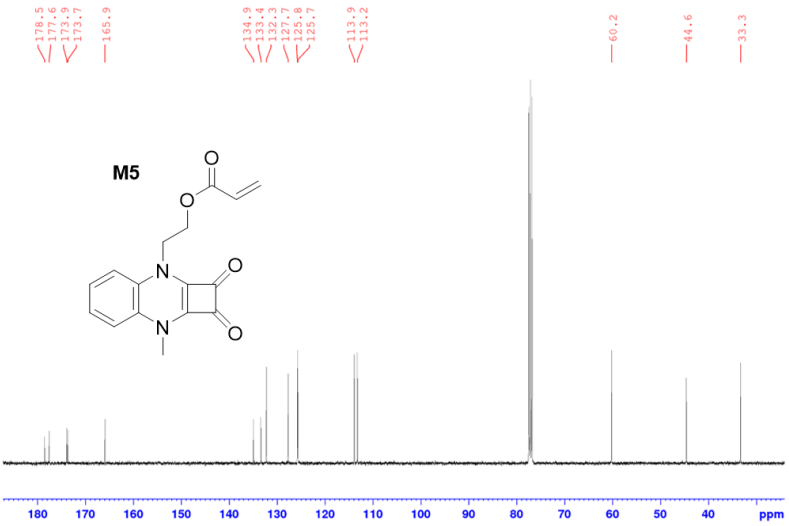

Fig. A.37 ^{13}C-NMR (100 MHz, $CDCl_3$) of M5.

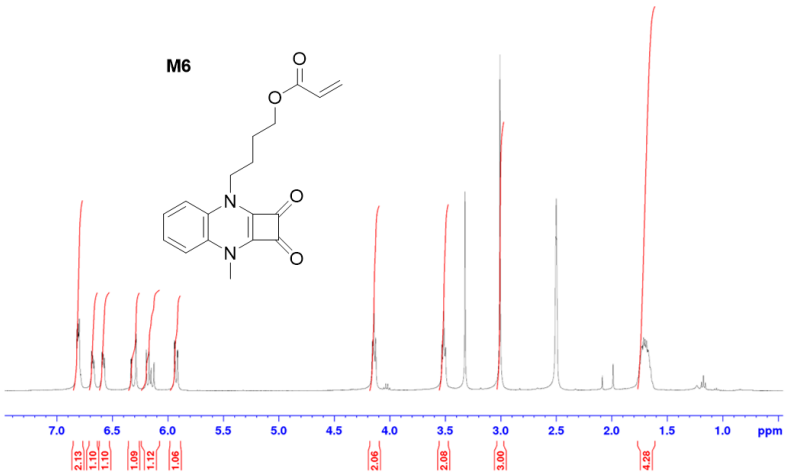

Fig. A.38 ^{1}H-NMR (400 MHz, DMSO) of M6.

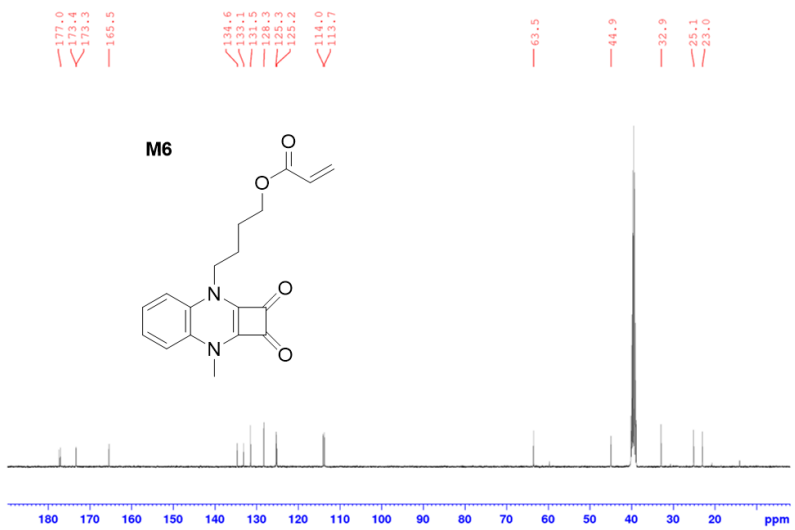

Fig. A.39 ^{13}C-NMR (100 MHz, DMSO) of M6.

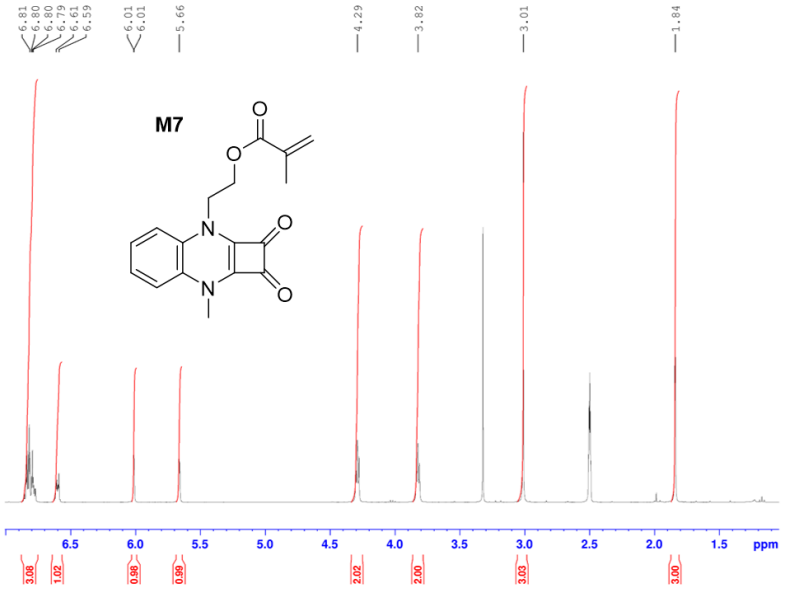

Fig. A.40 ^{1}H-NMR (400 MHz, DMSO) of M7.

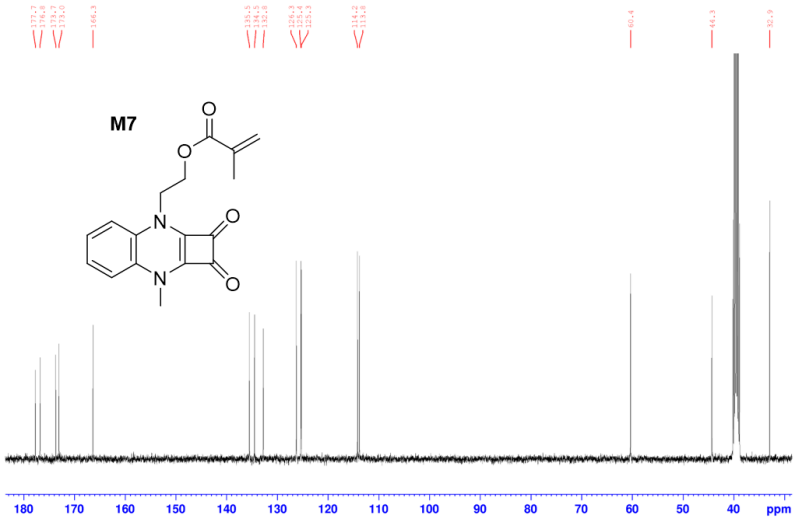

Fig. A.41 ^{13}C-NMR (100 MHz, DMSO) of M7.

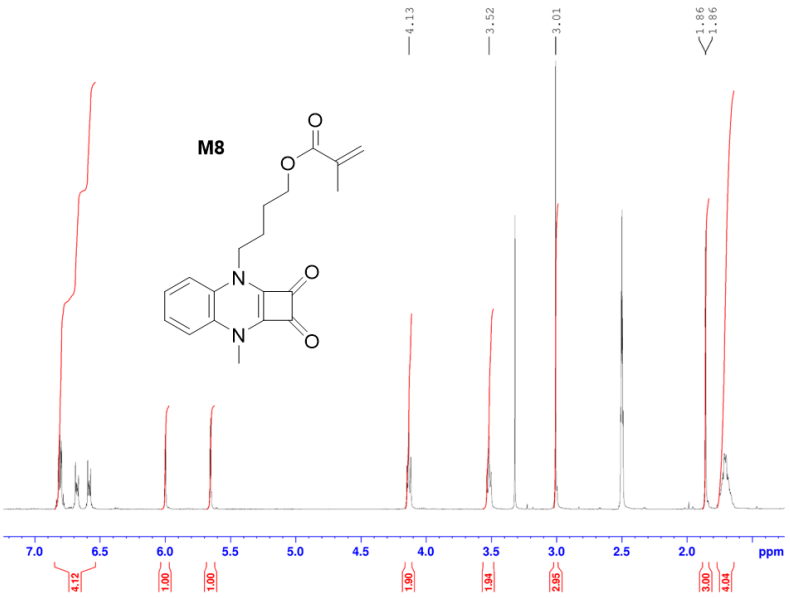

Fig. A.42 ^{1}H-NMR (400 MHz, DMSO) of M8.

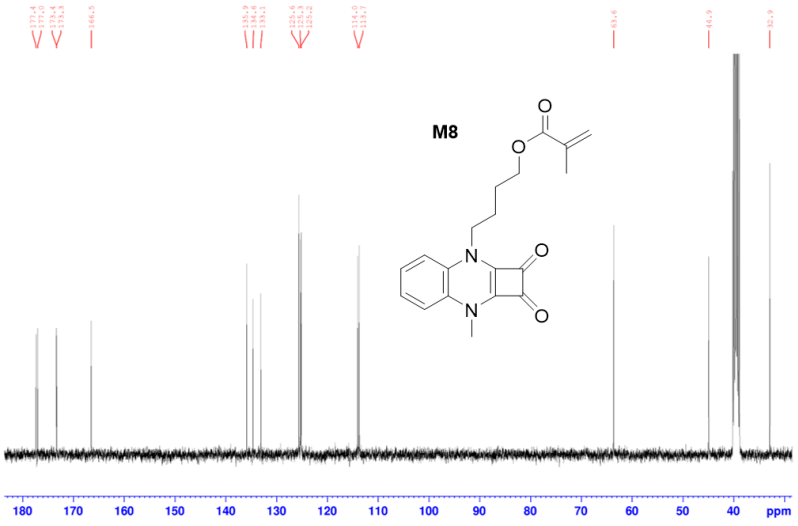

Fig. A.43 ^{13}C-NMR (100 MHz, DMSO) of M8.

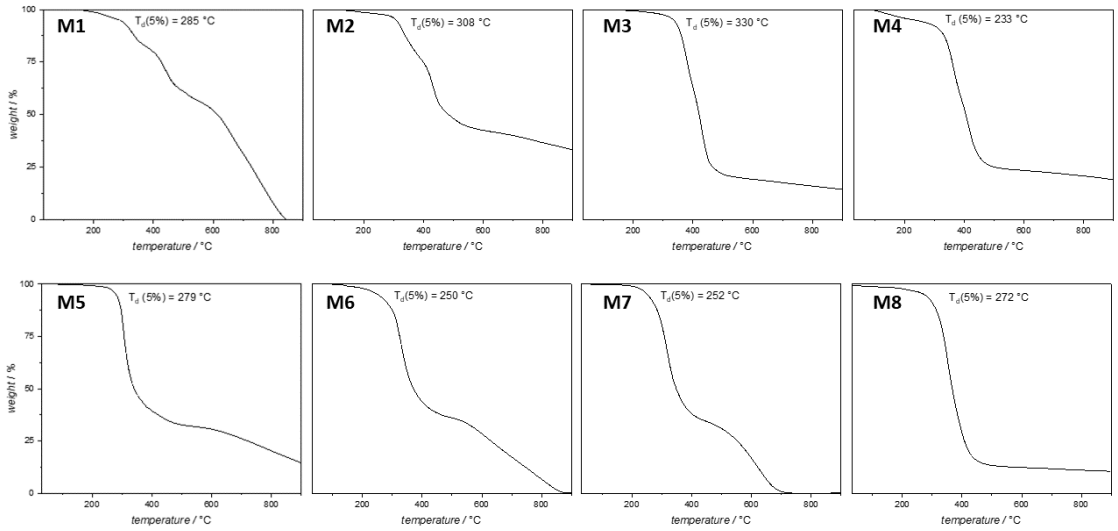

Fig. A.44 Thermal gravimetric analysis (TGA) curves from the SQX monomers M1 to M8 in nitrogen atmosphere from 30 - 900 °C.

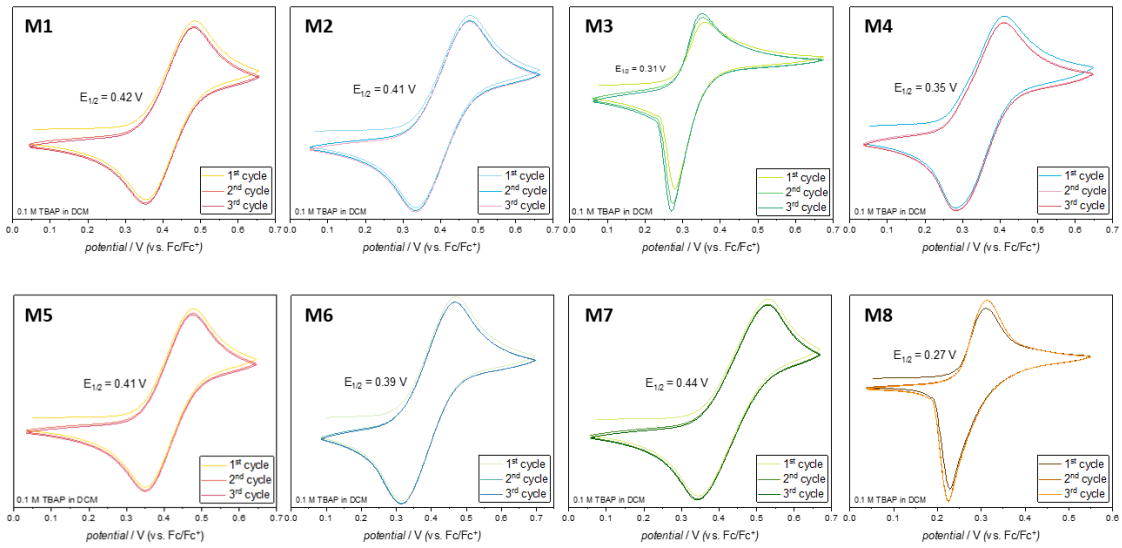

Fig. A.45 Cyclic voltammograms of the SQX monomers M1 to M8 in 0.1 M TBAP in DCM (referenced against ferrocene).

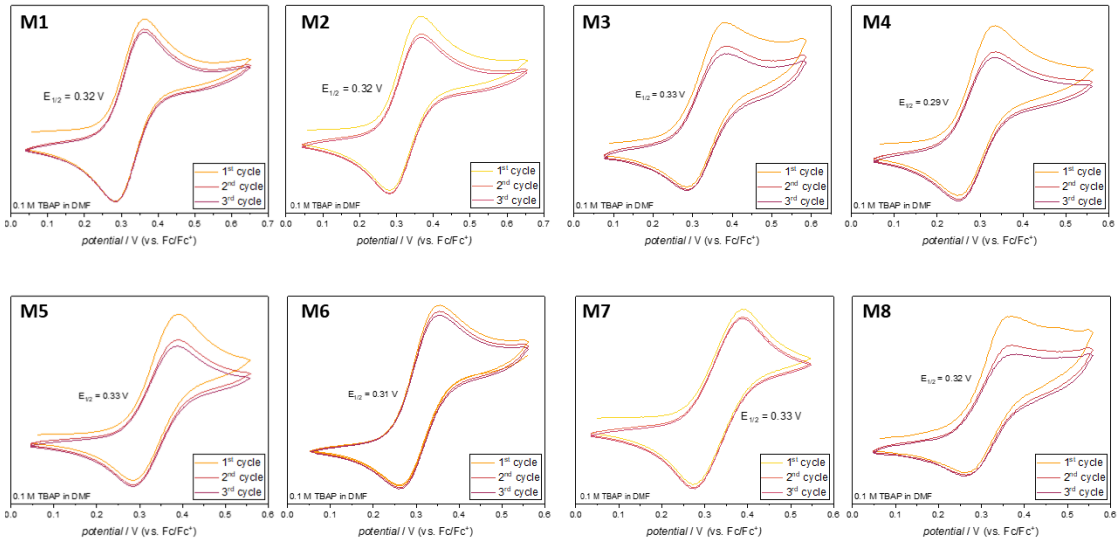

Fig. A.46 Cyclic voltammograms of the SQX monomers M1 to M8 in 0.1 M TBAP in DMF (referenced against ferrocene).

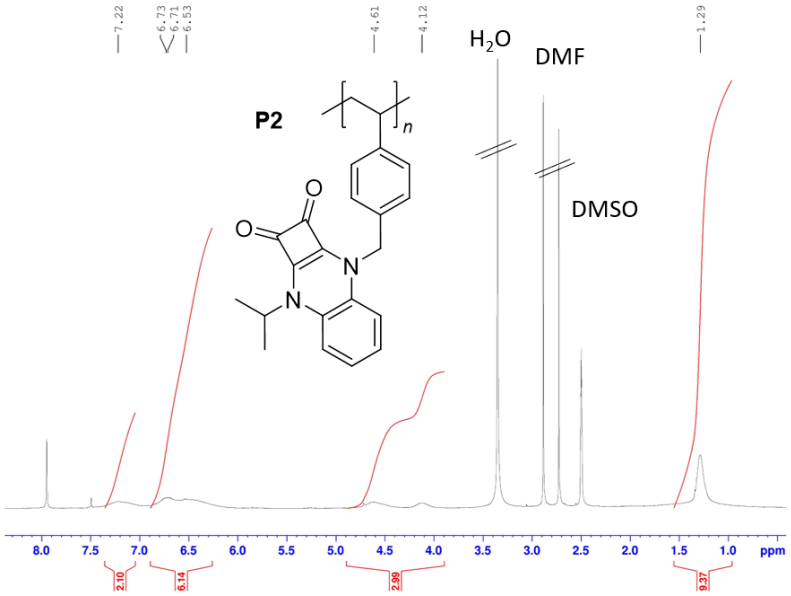

Fig. A.47 ^{1}H-NMR (400 MHz, DMSO) of P2.

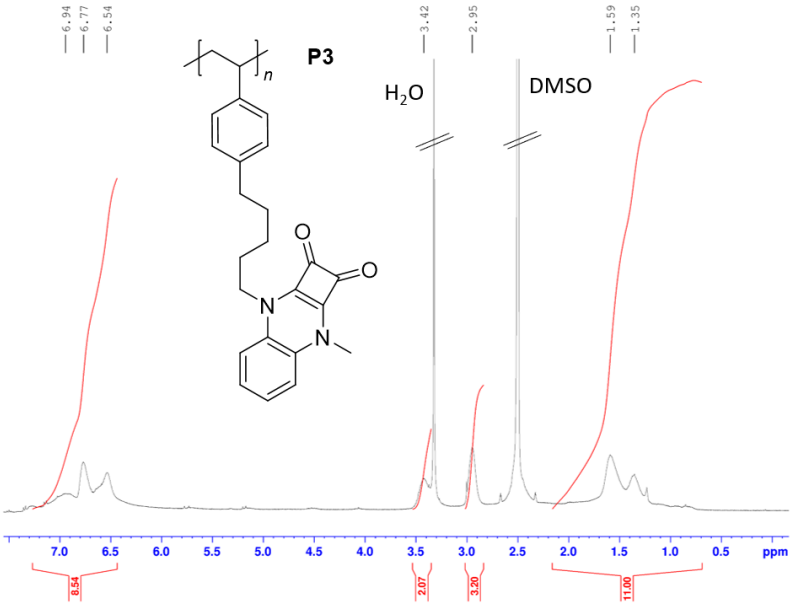

Fig. A.48 ^{1}H-NMR (400 MHz, DMSO) of P3.

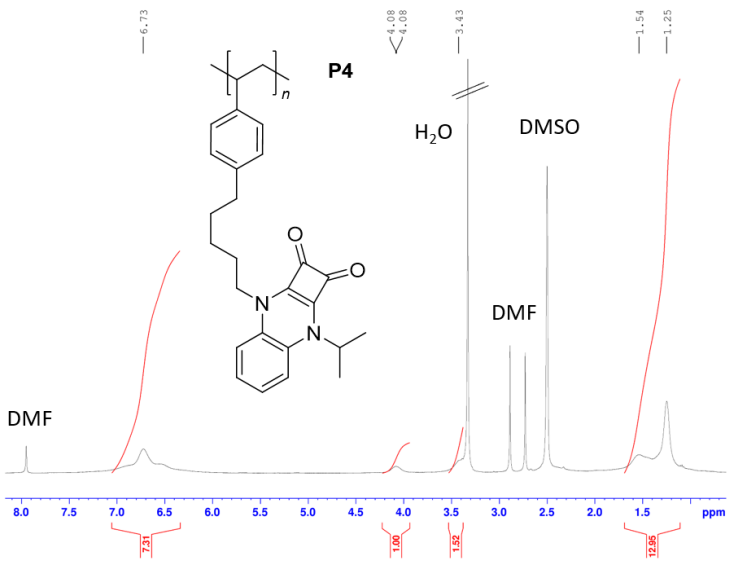

Fig. A.49 ^{1}H-NMR (400 MHz, DMSO) of P4.

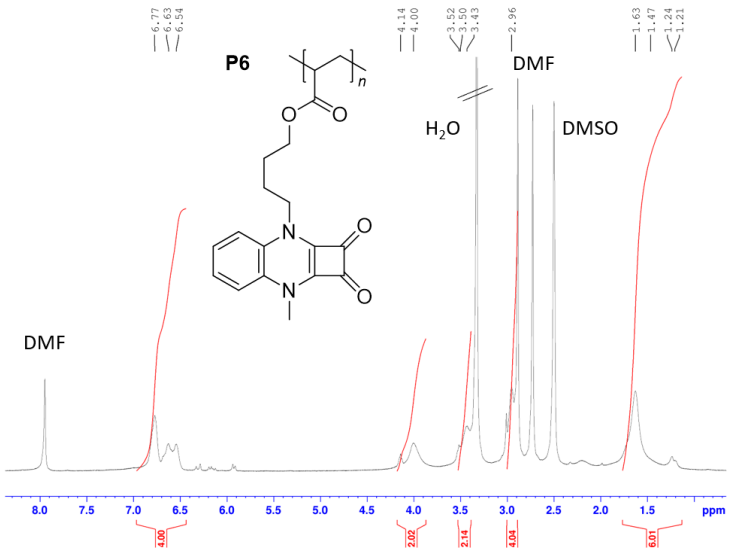

Fig. A.50 ^{1}H-NMR (400 MHz, DMSO) of P6.

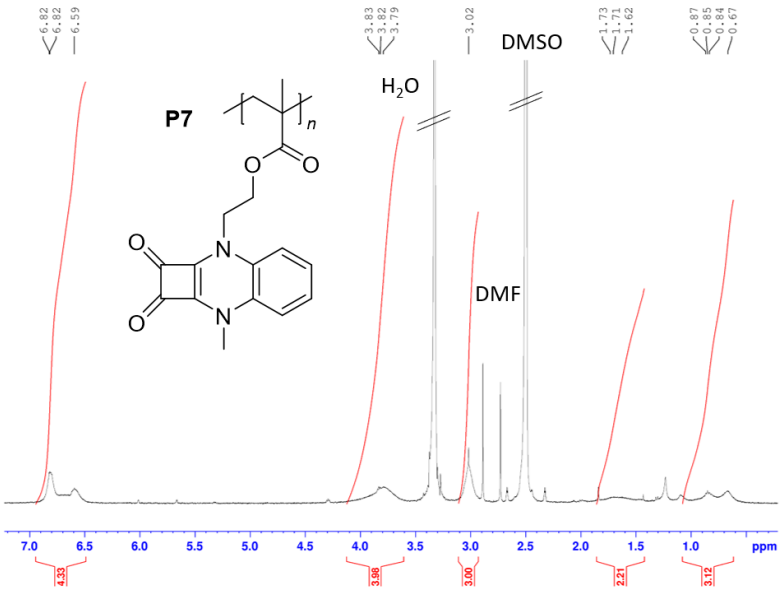

Fig. A.51 ^{1}H-NMR (400 MHz, DMSO) of P7.

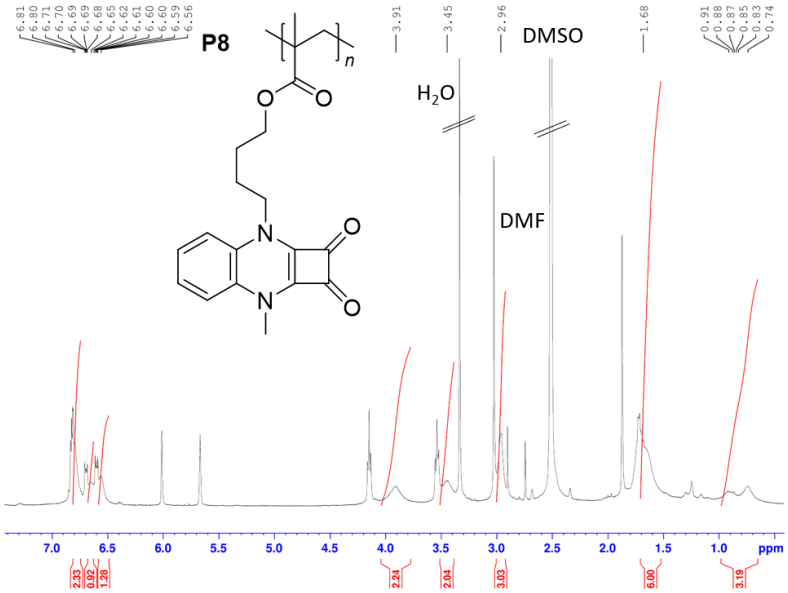

Fig. A.52 ^{1}H-NMR (400 MHz, DMSO) of P8.

List of Figures

List of Schemes

Bibliography

[1] Chen, Y.; Kang, Y.; Zhao, Y.; Wang, L.; Liu, J.; Li, Y.; Liang, Z.; He, X.; Li, X.; Tavajohi, N.; Li, B., *J. Energy Chem.* **2021**, *59*, 83.

[2] Mayyas, A.; Steward, D.; Mann, M., *Sustain. Mater. Technol.* **2019**, *19*, e00087.

[3] Usai, L.; Lamb, J.J.; Hertwich, E.; Burheim, O.S.; Strømman, A.H., *Environ. Res.: Infrastruct. Sustain.* **2022**, *2* (1), 011002.

[4] Gracia, R.; Mecerreyes, D., *Polym. Chem.* **2013**, *4* (7), 2206.

[5] Armand, M.; Tarascon, J.M., *Nature* **2008**, *451* (7179), 652.

[6] Hager, M.D.; Esser, B.; Feng, X.; Schuhmann, W.; Theato, P.; Schubert, U.S., *Adv. Mater.* **2020**, *32* (39), e2000587.

[7] Muench, S.; Wild, A.; Friebe, C.; Häupler, B.; Janoschka, T.; Schubert, U.S., *Chem. Rev.* **2016**, *116* (16), 9438.

[8] Poizot, P.; Gaubicher, J.; Renault, S.; Dubois, L.; Liang, Y.; Yao, Y., *Chem. Rev.* **2020**, *120* (14), 6490.

[9] Goujon, N.; Casado, N.; Patil, N.; Marcilla, R.; Mecerreyes, D., *Prog. Polym. Sci.* **2021**, *122*, 101449.

[10] Suga, T.; Ohshiro, H.; Sugita, S.; Oyaizu, K.; Nishide, H., *Adv. Mater.* **2009**, *21* (16), 1627.

[11] Goujon, N.; de Pariza, X.L.; Casado, N., In N. Casado (Editor), *Redox Polymers for Energy and Nanomedicine*, pp. 288–331, (Royal Society of Chemistry **2020**).

[12] Luo, J.; Hu, B.; Hu, M.; Zhao, Y.; Liu, T.L., *ACS Energy Lett.* **2019**, *4* (9), 2220.

[13] Lee, S.; Hong, J.; Kang, K., *Adv. Energy Mater.* **2020**, *10* (30), 2001445.

[14] Lee, M.H.; Kwon, G.; Lim, H.; Kim, J.; Kim, S.J.; Lee, S.; Kim, H.; Eum, D.; Song, J.H.; Park, H.; Seong, W.M.; Jung, Y.; Kang, K., *ACS Energy Lett.* **2022**, *7* (10), 3637.

[15] Wilkinson, D.; Bhosale, M.; Amores, M.; Naresh, G.; Cussen, S.A.; Cooke, G., *ACS Appl. Energy Mater.* **2021**, *4* (11), 12084.

[16] Bhosale, M.E.; Chae, S.; Kim, J.M.; Choi, J.Y., *J. Mater. Chem. A* **2018**, *6* (41), 19885.

[17] Gannett, C.N.; Melecio-Zambrano, L.; Theibault, M.J.; Peterson, B.M.; Fors, B.P.; Abruña, H.D., *Materials Report Energy* **2021**, *1* (1), 100008.

[18] Friebe, C.; Lex-Balducci, A.; Schubert, U.S., *ChemSusChem* **2019**, *12* (18), 4093.

[19] Kye, H.; Kang, Y.; Jang, D.; Kwon, J.E.; Kim, B.G., *Adv. Energy Sustainability Res.* **2022**, *3* (8), 2200030.

[20] Casado, N.; Mantione, D.; Shanmukaraj, D.; Mecerreyes, D., *ChemSusChem* **2020**, *13* (9), 2464.

[21] Hioe, J.; Šakić, D.; Vrček, V.; Zipse, H., *Org. Biomol. Chem.* **2015**, *13* (1), 157.

[22] Yoshida, Z.; Tawara, Y., *J. Am. Chem. Soc.* **1971**, *93* (10), 2573.

[23] Manecke, G.; Gauger, J., *Tetrahedron Lett.* **1967**, *8* (36), 3509.

[24] Cohen, S.; Cohen, S.G., *J. Am. Chem. Soc.* **1966**, *88* (7), 1533.

[25] Sevov, C.S.; Samaroo, S.K.; Sanford, M.S., *Adv. Energy Mater.* **2017**, *7* (5), 1602027.

[26] Robinson, S.G.; Yan, Y.; Hendriks, K.H.; Sanford, M.S.; Sigman, M.S., *J. Am. Chem. Soc.* **2019**, *141* (26), 10171.

[27] Yan, Y.; Vaid, T.P.; Sanford, M.S., *J. Am. Chem. Soc.* **2020**, *142* (41), 17564.

[28] Hünig, S.; Pütter, H., *Chem. Ber.* **1977**, *110* (7), 2524.

[29] Terpetschnig, E., *Dyes Pigm.* **1993**, *21* (3), 227.

[30] Ajayaghosh, A.; Eldo, J., *Org. Lett.* **2001**, *3* (16), 2595.

[31] Broggi, A.; Kim, H.; Jung, J.; Bracciale, M.P.; Santarelli, M.L.; Kim, C.; Marrocchi, A., *Macromol. Chem. Phys.* **2017**, *218* (13), 1600487.

[32] Qiao, W.; Li, Z., *Symmetry* **2022**, *14* (5), 966.

[33] Zu, Y.; Xu, Y.; Ma, L.; Kang, Q.; Wang, J.; Yao, H.; Hou, J.; Zu, Y.; Xu, Y.; Ma, L.; Kang, Q.; Wang, J.; Yao, H.; Hou, J., *Energy Stor. Mater.* **2021**, *41*, 240.

[34] Skujins, S.; Webb, G.A., *Chem. Commun.* **1968**, (11), 598.

[35] Armand, J.; Chekir, K.; Pinson, J., *Can. J. Chem.* **1974**, *52* (23), 3971.

[36] Hünig, S.; Bau, R.; Kemmer, M.; Meixner, H.; Metzenthin, T.; Peters, K.; Sinzger, K.; Gulbis, J., *Justus Liebigs Ann. Chem.* **1998**, *1998* (2), 335.

[37] Vitz, E., *J. Chem. Educ.* **2002**, *79* (3), 397.

[38] Shalev, H.; Evans, D.H., *J. Am. Chem. Soc.* **1989**, *111* (7), 2667.

[39] Bird, M.J.; Pearson, M.A.; Asaoka, S.; Miller, J.R., *J. Phys. Chem.* **2020**, *124* (26), 5487.

[40] Tiesinga, E.; Mohr, P.J.; Newell, D.B.; Taylor, B.N., *J. Phys. Chem. Ref. Data* **2021**, *50* (3), 033105.

[41] Lehmann, H.P.; Fuentes-Arderiu, X.; Bertello, L.F., *Pure Appl. Chem.* **1996**, *68* (4), 957.

[42] Pitzer, K.S.; Mayorga, G., *J. Phys. Chem.* **1973**, *77* (19), 2300.

[43] Johnson, M.P., *Essays Biochem.* **2016**, *60* (3), 255.

[44] Miller, S.L.; Smith-Magowan, D., *J. Phys. Chem. Ref. Data* **1990**, *19* (4), 1049.

[45] Perutz, M.F.; Fermi, G.; Luisi, B.; Shaanan, B.; Liddington, R.C., *Acc. Chem. Res.* **1987**, *20* (9), 309.

[46] Deuchert, K.; Hünig, S., *Angew. Chem. Int. Ed.* **1978**, *17* (12), 875.

[47] Shirakawa, H.; Louis, E.J.; MacDiarmid, A.G.; Chiang, C.K.; Heeger, A.J., *J. Chem. Soc., Chem. Commun.* **1977**, (16), 578.

[48] Das, T.K.; Prusty, S., *Polym.-Plast. Technol. Eng.* **2012**, *51* (14), 1487.

[49] K, N.; Rout, C.S., *RSC Adv.* **2021**, *11* (10), 5659.

[50] Zhang, X.; Xiao, Z.; Liu, X.; Mei, P.; Yang, Y., *Renew. Sust. Energ. Rev.* **2021**, *147*, 111247.

[51] Dodabalapur, A., *Mater. Today* **2006**, *9* (4), 24.

[52] Hess, M.; Jones, R.G.; Kahovec, J.; Kitayama, T.; Kratochvíl, P.; Kubisa, P.; Mormann, W.; Stepto, R.F.T.; Tabak, D.; Vohlídal, J.; Wilks, E.S., *Pure Appl. Chem.* **2006**, *78* (11), 2067.

[53] Ogata, N., *J. macromol. sci., Polym. rev.* **2002**, *42* (3), 399.

[54] Bocharova, V.; Sokolov, A.P., *Macromolecules* **2020**, *53* (11), 4141.

[55] Walton, D.J., *Mater. Des.* **1990**, *11* (3), 142.

[56] Heeger, A.J., *Angew. Chem. Int. Ed.* **2001**, *40* (14), 2591.

[57] Horie, K.; Barón, M.; Fox, R.B.; He, J.; Hess, M.; Kahovec, J.; Kitayama, T.; Kubisa, P.; Maréchal, E.; Mormann, W.; Stepto, R.F.T.; Tabak, D.; Vohlídal, J.; Wilks, E.S.; Work, W.J., *Pure Appl. Chem.* **2004**, *76* (4), 889.

[58] Arimoto, F.S.; Haven, A.C., *J. Am. Chem. Soc.* **1955**, *77* (23), 6295.

[59] Dai, G.; Liu, Y.; Niu, Z.; He, P.; Zhao, Y.; Zhang, X.; Zhou, H., *Matter* **2019**, *1* (4), 945.

[60] Nakahara, K.; Iwasa, S.; Satoh, M.; Morioka, Y.; Iriyama, J.; Suguro, M.; Hasegawa, E., *Chem. Phys. Lett.* **2002**, *359* (5-6), 351.

[61] Nakahara, K.; Oyaizu, K.; Nishide, H., *Chem. Lett.* **2011**, *40* (3), 222.

[62] Song, Z.; Qian, Y.; Zhang, T.; Otani, M.; Zhou, H., *Adv. Sci.* **2015**, *2* (9), 1500124.

[63] Yao, M.; Sano, H.; Ando, H.; Kiyobayashi, T., *Sci. Rep.* **2015**, *5*, 10962.

[64] Deng, S.R.; Kong, L.B.; Hu, G.Q.; Wu, T.; Li, D.; Zhou, Y.H.; Li, Z.Y., *Electrochim. Acta* **2006**, *51* (13), 2589.

[65] Niu, Z.; Wu, H.; Liu, L.; Dai, G.; Xiong, S.; Zhao, Y.; Zhang, X., *J. Mater. Chem. A* **2019**, *7* (17), 10581.

[66] Kolek, M.; Otteny, F.; Schmidt, P.; Mück-Lichtenfeld, C.; Einholz, C.; Becking, J.; Schleicher, E.; Winter, M.; Bieker, P.; Esser, B., *Energy Environ. Sci.* **2017**, *10* (11), 2334.

[67] Feng, J.K.; Cao, Y.L.; Ai, X.P.; Yang, H.X., *J. Power Sources* **2008**, *177* (1), 199.

[68] Suga, T.; Sugita, S.; Ohshiro, H.; Oyaizu, K.; Nishide, H., *Adv. Mater.* **2011**, *23* (6), 751.

[69] Chu, S.; Cui, Y.; Liu, N., *Nat. Mater.* **2016**, *16* (1), 16.

[70] Weber, A.Z.; Mench, M.M.; Meyers, J.P.; Ross, P.N.; Gostick, J.T.; Liu, Q., *J. Appl. Electrochem.* **2011**, *41* (10), 1137.

[71] Skyllas-Kazacos, M.; Rychcik, M.; Robins, R.G.; Fane, A.G.; Green, M.A., *J. Electrochem. Soc.* **1986**, *133* (5), 1057.

[72] Hagedorn, N.H.; Thaller, L.H., Improvement and scale-up of the NASA redox storage system. NASA TM-81632, **1980**.

[73] Jiang, H.R.; Sun, J.; Wei, L.; Wu, M.C.; Shyy, W.; Zhao, T.S., *Energy Stor. Mater.* **2020**, *24*, 529.

[74] Hruska, L.W.; Savinell, R.F., *J. Electrochem. Soc.* **1981**, *128* (1), 18.

[75] Winsberg, J.; Hagemann, T.; Janoschka, T.; Hager, M.D.; Schubert, U.S., *Angew. Chem. Int. Ed. Engl.* **2017**, *56* (3), 686.

[76] Rhodes, Z.; Cabrera-Pardo, J.R.; Li, M.; Minteer, S.D., *Isr. J. Chem.* **2021**, *61* (1-2), 101.

[77] Yan, Y.; Robinson, S.G.; Vaid, T.P.; Sigman, M.S.; Sanford, M.S., *J. Am. Chem. Soc.* **2021**, *143* (33), 13450.

[78] Yan, Y.; Sitaula, P.; Odom, S.A.; Vaid, T.P., *ACS Appl. Mater. Interfaces* **2022**, *14* (44), 49633.

[79] The Nobel Prize in Chemistry 2019. **9th october 2019**, URL `https://www.nobelprize.org/prizes/chemistry/2019/press-release/`.

[80] Mizushima, K.; Jones, P.C.; Wiseman, P.J.; Goodenough, J.B., *Mater. Res. Bull.* **1980**, *15* (6), 783.

[81] Yazami, R.; Touzain, P., *J. Power Sources* **1983**, *9* (3), 365.

[82] Shu, Z.X.; McMillan, R.S.; Murray, J.J., *J. Electrochem. Soc.* **1993**, *140* (4), 922.

[83] Yoshino, A., Secondary battery: United States Patent. **1987**, URL `https://patents.google.com/patent/US4668595A/en`.

[84] Yoshino, A., *Angew. Chem. Int. Ed.* **2012**, *51* (24), 5798.

[85] Manthiram, A., *Nat. Commun.* **2020**, *11* (1), 1550.

[86] Xu, C.; Dai, Q.; Gaines, L.; Hu, M.; Tukker, A.; Steubing, B., *Commun. Mater.* **2020**, *1* (1).

[87] Abraham, D.P.; Roth, E.P.; Kostecki, R.; McCarthy, K.; MacLaren, S.; Doughty, D.H., *J. Power Sources* **2006**, *161* (1), 648.

[88] Zhang, S.; Ding, Y.; Liu, B.; Chang, C.C., *Waste Management* **2017**, *65*, 113.

[89] Heelan, J.; Gratz, E.; Zheng, Z.; Wang, Q.; Chen, M.; Apelian, D.; Wang, Y., *JOM* **2016**, *68* (10), 2632.

[90] Vaalma, C.; Buchholz, D.; Weil, M.; Passerini, S., *Nat. Rev. Mater.* **2018**, *3* (4).

[91] Harper, G.; Sommerville, R.; Kendrick, E.; Driscoll, L.; Slater, P.; Stolkin, R.; Walton, A.; Christensen, P.; Heidrich, O.; Lambert, S.; Abbott, A.; Ryder, K.; Gaines, L.; Anderson, P., *Nature* **2019**, *575* (7781), 75.

[92] Ferreira, D.A.; Prados, L.M.Z.; Majuste, D.; Mansur, M.B., *J. Power Sources* **2009**, *187* (1), 238.

[93] Nishide, H.; Iwasa, S.; Pu, Y.J.; Suga, T.; Nakahara, K.; Satoh, M., *Electrochim. Acta* **2004**, *50* (2-3), 827.

[94] Nishide, H.; Suga, T., *Electrochem. Soc. Interface* **2005**, *14* (4), 32.

[95] Suguro, M.; Iwasa, S.; Kusachi, Y.; Morioka, Y.; Nakahara, K., *Meet. Abstr.* **2007**, *MA2007-01* (8), 424.

[96] Suguro, M.; Iwasa, S.; Kusachi, Y.; Morioka, Y.; Nakahara, K., *Macromol. Rapid Commun.* **2007**, *28* (18–19), 1929.

[97] Yokoji, T.; Kameyama, Y.; Maruyama, N.; Matsubara, H., *J. Mater. Chem. A* **2016**, *4* (15), 5457.

[98] Zhu, L.M.; Lei, A.W.; Cao, Y.L.; Ai, X.P.; Yang, H.X., *Chem. Commun.* **2013**, *49* (6), 567.

[99] Xie, J.; Wang, Z.; Xu, Z.J.; Zhang, Q., *Adv. Energy Mater.* **2018**, *8* (21), 1703509.

[100] Casado, N.; Mecerreyes, D., In N. Casado (Editor), *Redox Polymers for Energy and Nanomedicine*, pp. 1–26, (Royal Society of Chemistry **2020**).

[101] Zhang, S.; Ericsson, N.; Hansson, P.A.; Sjödin, M.; Nordberg, Å., *J. Clean. Prod.* **2022**, *337*, 130454.

[102] Breslow, R., *J. Am. Chem. Soc.* **1957**, *79* (19), 5318.

[103] Roberts, J.D.; Streitwieser, A.; Regan, C.M., *J. Am. Chem. Soc.* **1952**, *74* (18), 4579.

[104] Hückel, E., *Z. Elektrochem. Angew. Phys. Chem.* **1937**, (43), 752.

[105] Breslow, R.; Yuan, C., *J. Am. Chem. Soc.* **1958**, *80* (22), 5991.

[106] Breslow, R.; Groves, J.T., *J. Am. Chem. Soc.* **1970**, *92* (4), 984.

[107] Breslow, R.; Hover, H.; Chang, H.W., *J. Am. Chem. Soc.* **1962**, *84* (16), 3168.

[108] Kerber, R.C.; Hsu, C.M., *J. Am. Chem. Soc.* **1973**, *95* (10), 3239.

[109] Curnow, O.J.; MacFarlane, D.R.; Walst, K.J., *Chem. Commun.* **2011**, *47* (37), 10248.

[110] Bandar, J.; Lambert, T., *Synthesis* **2013**, *45* (18), 2485.

[111] Walst, K.J.; Yunis, R.; Bayley, P.M.; MacFarlane, D.R.; Ward, C.J.; Wang, R.; Curnow, O.J., *RSC Adv.* **2015**, *5* (49), 39565.

[112] Freyer, J.L.; Brucks, S.D.; Gobieski, G.S.; Russell, S.T.; Yozwiak, C.E.; Sun, M.; Chen, Z.; Jiang, Y.; Bandar, J.S.; Stockwell, B.R.; Lambert, T.H.; Campos, L.M., *Angew. Chem. Int. Ed. Engl.* **2016**, *55* (40), 12382.

[113] Abel, B.A.; Lidston, C.A.L.; Coates, G.W., *J. Am. Chem. Soc.* **2019**, *141* (32), 12760.

[114] Gerson, F.; Plattner, G.; Yoshida, Z., *Mol. Phys.* **1971**, *21* (6), 1027.

[115] Weiss, R.; Schloter, K., *Tetrahedron Lett.* **1975**, *16* (40), 3491.

[116] Johnson, R.W., *Tetrahedron Lett.* **1976**, *17* (8), 589.

[117] Yan, Y.; Robinson, S.G.; Sigman, M.S.; Sanford, M.S., *J. Am. Chem. Soc.* **2019**, *141* (38), 15301.

[118] Brucks, S.D.; Freyer, J.L.; Lambert, T.H.; Campos, L.M., *Polymers* **2017**, *9* (3).

[119] Steinman, N.Y.; Starr, R.L.; Brucks, S.D.; Belay, C.; Meir, R.; Golenser, J.; Campos, L.M.; Domb, A.J., *Macromolecules* **2019**, *52* (9), 3543.

[120] Paren, B.A.; Raghunathan, R.; Knudson, I.J.; Freyer, J.L.; Campos, L.M.; Winey, K.I., *Polym. Chem.* **2019**, *10* (22), 2832.

[121] Jiang, Y.; Freyer, J.L.; Cotanda, P.; Brucks, S.D.; Killops, K.L.; Bandar, J.S.; Torsitano, C.; Balsara, N.P.; Lambert, T.H.; Campos, L.M., *Nat. Commun.* **2015**, *6*, 5950.

[122] Montoto, E.C.; Cao, Y.; Hernández-Burgos, K.; Sevov, C.S.; Braten, M.N.; Helms, B.A.; Moore, J.S.; Rodríguez-López, J., *Macromolecules* **2018**, *51* (10), 3539.

[123] Brucks, S.D.; Steinman, N.Y.; Starr, R.L.; Domb, A.J.; Campos, L.M., *J. Polym. Sci. A Polym. Chem.* **2018**, *56* (23), 2641.

[124] Wang, Y.; Ji, H.; Zhang, X.; Shi, J.; Li, X.; Jiang, X.; Qu, X., *ACS Appl. Mater. Interfaces* **2021**, *13* (14), 16469.

[125] Lian, S.; Wang, Y.; Ji, H.; Zhang, X.; Shi, J.; Feng, Y.; Qu, X., *Nanomaterials* **2021**, *11* (10).

[126] Maahs, G., *Justus Liebigs Ann. Chem.* **1965**, *686* (1), 55.

[127] Ehrhardt, H.; Hünig, S.; Pütter, H., *Chem. Ber.* **1977**, *110* (7), 2506.

[128] Yagi, S.; Hyodo, Y.; Matsumoto, S.; Takahashi, N.; Kono, H.; Nakazumi, H., *J. Chem. Soc., Perkin Trans. 1* **2000**, (4), 599.

[129] Connell, A.; Holliman, P.J.; Jones, E.W.; Furnell, L.; Kershaw, C.; Davies, M.L.; Gwenin, C.D.; Pitak, M.B.; Coles, S.J.; Cooke, G., *J. Mater. Chem. A* **2015**, *3* (6), 2883.

[130] Markgraf, J.H.; Homan, W.P.; Katt, R.J.; Scott, W.L., *J. Heterocycl. Chem.* **1969**, *6* (1), 135.

[131] Ried, W.; Kunstmann, W., *Chem. Ber.* **1969**, *102* (4), 1439.

[132] Hünig, S.; Pütter, H., *Chem. Ber.* **1977**, *110* (7), 2532.

[133] Tobey, S.W.; West, R., *J. Am. Chem. Soc.* **1966**, pp. 2478–2481.

[134] Dehmlow, E.V.; Höfle, G., *Chem. Ber.* **1974**, *107* (8), 2760.

[135] Nacsa, E.D.; Lambert, T.H., *J. Am. Chem. Soc.* **2015**, *137* (32), 10246.

[136] Karunakaran, C.; Santharaman, P.; Balamurugan, M., In *Spin Resonance Spectroscopy*, pp. 49–110, (Elsevier **2018**).

[137] Hamann, C.H.; Hamnett, A.; Vielstich, W., *Electrochemistry*, (Wiley-VCH **1998**).

[138] Guo, W.; Yin, Y.X.; Xin, S.; Guo, Y.G.; Wan, L.J., *Energy Environ. Sci.* **2012**, *5* (1), 5221.

[139] Rieger, J., *J. Therm. Anal. Calorim.* **1996**, *46* (3-4), 965.

[140] Sulikowski, G.A.; Sulikowski, M.M.; Haukaas, M.H.; Moon, B., In *Encyclopedia of Reagents for Organic Synthesis*, (John Wiley & Sons, Ltd **2001**).

[141] Catalán, J.; Palomar, J.; Díaz, C.; de Paz, J.L.G., *J. Phys. Chem. A* **1997**, *101* (28), 5183.

[142] White, D.P.; Anthony, J.C.; Oyefeso, A.O., *J. Org. Chem.* **1999**, *64* (21), 7707.

[143] Wunderlich, B., *J. Chem. Phys.* **1958**, *29* (6), 1395.

[144] Safari, A.; Saidur, R.; Sulaiman, F.A.; Xu, Y.; Dong, J., *Renew. Sust. Energ. Rev.* **2017**, *70*, 905.

[145] Mark, J.E. (Editor), *Physical properties of polymers handbook*, (Springer Science + Business Media LLC **2007**), 2nd edn.

[146] Gaur, U.; Lau, S.f.; Wunderlich, B.B.; Wunderlich, B., *J. Phys. Chem. Ref. Data* **1982**, *11* (4), 1065.

[147] Fulmer, G.R.; Miller, A.J.M.; Sherden, N.H.; Gottlieb, H.E.; Nudelman, A.; Stoltz, B.M.; Bercaw, J.E.; Goldberg, K.I., *Organometallics* **2010**, *29* (9), 2176.